

MICROSTRUCTURAL FORMATIONS AND PHASE TRANSFORMATION  
PATHWAYS IN TANTALUM CARBIDES

by

ROBERT ALLEN MORRIS

A DISSERTATION

Submitted in partial fulfillment of the requirements  
for the degree of Doctor of Philosophy in the  
Department of Metallurgical Engineering  
in the Graduate School of  
The University of Alabama

TUSCALOOSA, ALABAMA

2010

Copyright Robert Allen Morris 2010

**ALL RIGHTS RESERVED**

## ABSTRACT

Transition metal carbides have a large assortment of applications because of their high hardness, chemical resistance, and high melting temperatures. Tantalum carbide (TaC) and its sub-stoichiometric Ta<sub>2</sub>C and Ta<sub>4</sub>C<sub>3</sub> phases have emerged as candidate materials for ultra-high temperature structural applications. A consequence of the high melting temperature is the limiting methods to fabricate near-net shape, near full density tantalum carbides. In general, hot-isostatic pressing (HIP) and/or arc melting/vacuum plasma spraying (VPS) of powders are the viable means of manufacturing. In HIP'ing, the phase formation is through solid-state reactions whereas arc melting/VPS involves rapid solidification. Additionally, the precipitation of multiple phases generates various orientation relationships that influence the grain morphology. Depending on carbon content, the grains were equiaxed, equiaxed with a cross-hatch pattern of thin laths of secondary phases, to acicular grains. The microstructures were quantified through a series of different 2D and 3D analytical techniques.

To understand how these microstructures developed, a series of XTa:(1-X)C (0.5<X<1) atomic compositions have been fabricated by VPS and HIP processes that spanned the single phase TaC, multi-phase TaC+Ta<sub>4</sub>C<sub>3</sub>+Ta<sub>2</sub>C and single phase Ta<sub>2</sub>C fields. The results revealed that the grain size was constrained by either the larger as-sprayed grain sizes in the VPS process or the largest powder sizes that sintered in the HIP process. The equiaxed grains formed in the single phase materials because they did not have another phase which would dictate a low energy orientation relationship to change the grain morphology. The cross-hatch pattern in the equiaxed grains formed from the precipitation of the lower melting temperature Ta<sub>4</sub>C<sub>3</sub> and Ta<sub>2</sub>C phases in the TaC matrix on the closed packed planes. Since the B1 TaC structure has multiple variants of

these {111} planes, these precipitates formed on these different planes. The acicular grains revealed fine secondary phase laths that were parallel to the major axis of the grain. These laths formed unidirectional as a result of the TaC phase precipitation from a Ta<sub>2</sub>C matrix, which is a hexagonal closed packed structure and only has one closed packed plane orientation, {0001}. This low energy interface exhibited a preferential growth direction.

The formation of oxide inclusions and porosity within the tantalum carbides were also examined. The oxides phases were identified to be Ta<sub>2</sub>O<sub>5</sub> and TaO through selected area electron diffraction. Serial sectioning and 3D reconstruction was used to quantify the globular oxide structure.

Finally, a thermo-mechanical testing apparatus has been constructed where an electrical current provides resistive heating and, in the presence of a magnetic field, provides a Lorentz force for the application of a load on a test bar specimen. The electromagnetic Helmholtz coil can be used to independently control the magnetic flux, or load, while adjusting the specimen current for resistive heating of the specimen. The coils and specimen were encased in a stainless steel chamber that controlled the testing environment. The apparatus successfully deformed test bars of  $\gamma$ -TaC at 2600 °C and 3100 °C for 30 minutes. The temperature and deflection measurements were simulated using a finite element model. During the thermo-mechanical testing, the equiaxed grains grew isotropic with the intrinsic porosity, observed in pre-tested grain boundaries, providing microstructural markers of the grains initial size, shape and location in the microstructure.

## DEDICATION

This dissertation is dedicated to my loving wife Bethany and my daughter Briella.

## ACKNOWLEDGMENTS

I am pleased to have this opportunity to thank the many colleagues, friends, and faculty members who have helped me with this research project. I am most indebted to my advisor Gregory Thompson, the chairman of this dissertation, for sharing his research expertise and wisdom regarding materials science. I would also like to thank all of my committee members, Viola Acoff, Richard Bradt, Daniel Butts, Robin Foley, Lawrence Matson, and Mark Weaver for their invaluable input, inspiring questions, and support of both the dissertation and my academic progress. I would like to thank Daniel Butts with Plasma Processing, Inc. and Steve DiPietro with Exothermics, Inc for providing a gracious amount of samples used in this research. I also thank Michael Uchic and Paul Shade for providing the scripting computers files used for the serial sectioning of the samples in this dissertation. A majority of this research has been financially supported by the Army Research Office under grant W911NF-08-1-0300, with support for the non-contact testing rig from the Missile Defense Agency under contract HQ0006-08-C-7663.

Finally, this research would not have been possible without the support of my friends and fellow graduate students and of course of my family who never stopped encouraging me to persist, especially my parents, Rob and Donna Morris.

## CONTENTS

ABSTRACT.....	ii
DEDICATION.....	iv
ACKNOWLEDGMENTS .....	v
LIST OF ABBREVIATIONS AND SYMBOLS .....	ix
LIST OF TABLES.....	xi
LIST OF FIGURES .....	xii
CHAPTER 1: INTRODUCTION.....	1
1.1    Motivation.....	1
1.2    Technical Background .....	2
1.3    Processing Dependent Microstructures.....	5
1.4    Thermo-mechanical Testing .....	8
1.5    Dissertation Organization .....	9
CHAPTER 2: MICROSTRUCTURAL FORMATIONS AND PHASE TRANSFORMATION PATHWAYS IN HOT ISOSTATICALLY PRESSED TANTALUM CARBIDES .....	10
1.    Introduction.....	11
2.    Experimental Procedures .....	13
3.    Results.....	15
4.    Discussion.....	32
5.    Conclusions.....	38
6.    Acknowledgement: .....	39

7.	References.....	39
<b>CHAPTER 3: TANTALUM CARBIDE PHASES AND MICROSTRUCTURES PROCESSED BY VACUUM PLASMA SPRAYING .....</b>		<b>42</b>
1.	Introduction.....	43
2.	Experimental Procedure.....	45
3.	Results.....	49
4.	Discussion.....	56
5.	Conclusion .....	60
6.	Acknowledgement .....	61
7.	References.....	61
<b>CHAPTER 4: FORMATION OF OXIDE INCLUSIONS AND POROSITY IN VACUUM PLASMA SPRAYED TANTALUM CARBIDES MICROSTRUCTURES .....</b>		<b>64</b>
1.	Introduction.....	65
2.	Experimental.....	66
3.	Results & Discussion .....	71
4.	Conclusion .....	83
5.	Acknowledgement .....	83
6.	References.....	83
<b>CHAPTER 5: THERMO-MECHANICAL TESTING OF TANTALUM CARBIDES USING A LORENTZ-FORCE, NON-CONTACT TECHNIQUE .....</b>		<b>87</b>
1.	Introduction.....	88
2.	Modifications to the Lorentz-force, non-contact apparatus.....	90

3.	Results and Discussion .....	96
4.	Summary .....	105
5.	Acknowledgements:.....	105
6.	References.....	105
CHAPTER 6: CONCLUSIONS AND FUTURE DIRECTIONS .....		108
6.1	General Summary .....	108
6.2	Linking Microstructure to Processing.....	111
6.3	A Perspective on the Nucleation of Secondary Phases.....	112
6.4	Thermo-mechanical Test Rig Improvements.....	116
REFERENCES .....		118
APPENDIX A: PROPERTY VALUES.....		122
APPENDIX B: SIMULATED ZONE AXIS FOR COMMON TANTALUM CARBIDE PHASES.....		125
APPENDIX C: SERIAL SECTIONING PROCEDURES .....		127

## LIST OF ABBREVIATIONS AND SYMBOLS

3D	Three-dimensional
at%	atomic percent
B	Magnetic flux, in Tesla
$\epsilon$	Emissivity
EBS	Electron backscattered diffraction
EDS	Energy dispersive spectroscopy
eV	electron volts
fcc	face centered cubic
FIB	Focused ion beam
HAADF	High angle annular dark field
hcp	Hexagonal close packed
HIP	Hot isostatic pressing
I	current, in Amperes
°C	Celsius
OR	Orientation relationship
Pa	Pascal

ROI	Region of interest
$\sigma_{\max}$	Maximum applied stress
SAED	Selected area electron diffraction
SEM	Scanning electron microscope
SPS	spark plasma sintering
STEM	Scanning transmission electron microscope
TaC	Tantalum carbide
TEM	Transmissions electron microscope
$T_m$	Melting temperature
UHTC	Ultra high temperature ceramic
VPS	Vacuum plasma spraying
XRD	X-ray diffraction

## LIST OF TABLES

### Chapter 2

**Table 1:** Tabulated data for the specimens prepared..... 13

**Table 2:** Grain size analysis data for the  $Ta_xC_{1-x}$  specimens..... 17

**Table 3:** Grain size data for Figure (8)..... 28

### Chapter 3

**Table 1:** Tabulated phase amounts for the samples used for this investigation determined by integrated intensities of the XRD scans in figure 2(d) and 4(a). ..... 47

**Table 2:** Tabulated carbon content data for the samples used for this investigation determined using both the lever rule and EDS. .... 48

### Chapter 4

**Table 1:** XRD and EDS data for the starting powders and VPS process sample.. ..... 69

### Chapter 5

**Table 1:** Table of the various experimental parameters for the as-cut specimens and the deformed specimens #1 and #2..... 100

## LIST OF FIGURES

### Chapter 1

<b>Figure 1:</b> The tantalum-carbide phase diagram. ....	3
<b>Figure 2:</b> (a) The $\gamma$ -TaC phase is a B1 compound, i.e. the rock-salt structure. (b) The rhombohedral $\zeta$ -Ta <sub>4</sub> C <sub>3</sub> crystal structure. (c) The hexagonal $\beta$ -Ta <sub>2</sub> C crystal structure ...	3
<b>Figure 3:</b> Variation in tantalum carbide microstructures for different carbon compositions. ....	6

### Chapter 2

<b>Figure 1:</b> Ta-C binary phase diagram showing a highlighted region of the Ta/C content obtained for each specimen investigated. ....	12
<b>Figure 2:</b> Grain size data and SEM Images from the initial Ta and TaC powders used in the fabrication of the Ta <sub>x</sub> C <sub>1-x</sub> specimens. ....	16
<b>Figure 3:</b> XRD and FIB micrographs of XRD data of the XTa:(1-X)C specimens .....	19
<b>Figure 4:</b> FIB and STEM-HAADF images of the labeling method used in the diffusion couple. ....	22
<b>Figure 5:</b> EDS and XRD line data from diffusion couple. ....	23
<b>Figure 6:</b> EBSD of diffusion couple. ....	25
<b>Figure 7:</b> EBSD and SEM micrographs of diffusion couple .....	26
<b>Figure 8:</b> EBSD Image quality maps with corresponding phase maps of the Ta <sub>2</sub> C/Ta interface.	28
<b>Figure 9:</b> STEM-HAADF images and SAED of a conventionally prepared TEM foil of the diffusion couple. ....	30

### Chapter 3

<b>Figure 1:</b> Ta-C binary phase diagram showing a highlighted region of the Ta/C content obtained for each specimen investigated, as determined by EDS. Phase diagram from work by Barabash et al. [8]. ....	44
<b>Figure 2 :</b> Images and XRD data from 53Ta:47C. ....	50
<b>Figure 3:</b> SEM and EBSD micrographs of as-sprayed specimen .....	50
<b>Figure 4:</b> XRD and FIB micrographs of the VPS specimens .....	52

<b>Figure 5:</b> TEM data of 55Ta:45C specimen .....	53
<b>Figure 6:</b> Different viewing direction of a 3D reconstruction of a grain in 55Ta:45C.....	54
<b>Figure 7:</b> FIB and TEM micrographs of 63Ta:37C specimen.....	55
<b>Figure 8:</b> Different viewing direction of a 3D reconstruction of a grain in 63Ta:37C.....	56
Chapter 4	
<b>Figure 1:</b> Serial sectioning sample preparation.....	68
<b>Figure 2:</b> (a) Monte-Carlo simulation of the electron beam interaction within the TaC material showing larger volume of interaction for higher accelerating voltages. (b) A plot of the variation of Ta content for different accelerating voltages on a 51Ta:49C sample. ....	70
<b>Figure 3:</b> SEM image and EDS spectral maps of the starting powder. ....	72
<b>Figure 4:</b> XRD and SEM micrographs of 61Ta:39C specimen.....	73
<b>Figure 5:</b> TEM data of 61Ta:39C specimen. ....	75
<b>Figure 6:</b> SEM image and EDS spectral maps of the 61Ta:39C sample with an oxide inclusion. ....	76
<b>Figure 7:</b> SEM and TEM micrographs of oxide inclusion within the 61Ta:39C microstructure.....	78
<b>Figure 8:</b> TEM data and micrographs of oxide inclusion within the 61Ta:39 microstructure ....	79
<b>Figure 9:</b> (a) A slice taken from the serial sectioned microstructure showing an inclusion. (b) 3D perspective of the reconstructed inclusions (light grey) and porosity (dark grey). (c-d) Different perspectives of the 3D reconstruction of the inclusion revealing an interconnected globular structure. ....	81
<b>Figure 10:</b> (a) Histogram of pore volume within the serial sectioned volume. (b-d) Multiple viewing perspectives of the reconstructed porosity within the microstructure. ....	82
Chapter 5	
<b>Figure 1:</b> (a) Image of the thermo-mechanical testing rig with the components labeled (b) Clamp-type mount for holding the test bar between the electromagnets. The specimen shown is post thermo-mechanical loading; the initial specimen was flat. (c) Test bar during heating experiment with the electromagnet and conical iron cores and gas inlet above the specimen. (d) Electronics and related machinery.....	91
<b>Figure 2:</b> (a) Illustration of the Lorenz force applied to a current carrying conductor in the presence of a magnetic field. (b) Plot of real-time displacement and magnetic flux	

for a TaC sample held at 2000°C. (c) Iso-loading contour plot showing temperature-magnetic flux relationships to provide a constant stress. .... 95

**Figure 3:** (a) Oxide scale after heating  $Ta_xC_{1-x}$  in atmosphere. (b) Surface tantalum layer that was transformed from the  $Ta_xC_{1-x}$  bar by de-carburization at elevated temperature in Ar environment. .... 97

**Figure 4:** (a) Plot of the carburization and decarburization of  $Ta_xC_{1-x}$  at 2600 °C after 30 minutes at various methane chamber pressures. (b) Decarburization of  $Ta_xC_{1-x}$  to tantalum at a working pressure of 0.33 Pa of  $CH_4$ . (c) Micrograph showing no visible transformation at 0.66 Pa of  $CH_4$ . (d) Carburization of  $Ta_xC_{1-x}$  to TaC at a working pressure of 0.99 Pa of  $CH_4$ . (e) EBSD phase map of (d) showing the carburized TaC layer that formed. (f) Micrograph of transformed TaC layer in a highly carburizing environment of 4.4 Pa of  $CH_4$ . .... 99

**Figure 5:** (a) Surface plot of the simulated magnetic flux density of the electromagnet with an iron core. (b) Plot of the simulated magnetic flux across the test bar length for two different iron core air gaps of 4 mm and 8 mm. (c) 3D model of the clamp fixture and specimen used for the modeling of the thermo-mechanical testing rig. (d) Plot of the simulated specimen temperature. (e) Images of the as-cut sample and deformed specimens #1 and #2 with the simulated deformed specimen overlaid with the temperature profile. (f) Plot of the experimental and simulated displacements across the length of the deformed specimens. .... 101

**Figure 6:** (a-b) SEM micrographs of the as-cut microstructure showing equiaxed grains with the porosity located at the grain boundaries. (c) Post heating of specimen #1 microstructure. (d) Post heating of specimen of #2 microstructure ..... 104

Conclusions and Summary

**Figure 1:** STEM-HAADF of TaC grain with the initial formations of sub-carbide phases. .... 114

**Figure 2:** Transformation of the TaC structure to the  $Ta_2C$  structure by a diffusion/shear mechanism. .... 116

**Figure 3:** Transformation of the TaC structure to the  $Ta_4C_3$  structure by a diffusion/shear mechanism. .... 117

Appendix B

**Figure 1:** TEM electron diffraction simulation of the TaC structure for the viewing directions of (a) [100], (b) [110], and (c) [111]. .... 125

**Figure 2:** TEM electron diffraction simulation of the Ta<sub>2</sub>C structure for the viewing directions of (a) [1010], (b) [1230], and (c) [0001].....126

**Figure 3:** TEM electron diffraction simulation of the Ta<sub>4</sub>C<sub>3</sub> structure for the viewing directions of (a) [1010], (b) [1230], and (c) [0001].....126

Appendix C

**Figure 1:** Sample positions in relation to the ion source during the different steps of the serial sectioning script..... 127

**Figure 2:** Runscript user interface..... 129

**Figure 3:** Milled sections of cutting image ..... 130

**Figure 4:** Cropped Cutalign.bmp image for image matching routine..... 131

**Figure 5:** Imaging area of ROI showing the milled trenches and image alignment mark. .... 132

**Figure 6:** Initial autolog.99 file..... 134

**Figure 7:** Location of the "#" sign to be replaced and added in the AutoSV.psc file..... 134

**Figure 8:** Location of the parameter to be edited in the setup.ini file..... 135

**Figure 9:** Location of milling box showing the extended size..... 137

## CHAPTER 1

### INTRODUCTION

#### 1.1 Motivation

In materials engineering, understanding the interrelationship of processing-properties-structure is a pre-requisite for developing superior materials. For several years, there has been a significant interest in developing optimal ceramic microstructures for use in severe elevated temperature structural applications. Thermo-mechanical properties are a direct function of grain size, composition and crystal structure. In transition metal carbides, Santoro [1] and others [2,3,4,5,6] have found a strong dependency in microhardness, electrical resistivity, and intrinsic crystal properties, like melting point and lattice parameter, as a function of carbon content. In particular to the Ta-C binary system, the basic relationships between phase content, microstructure, and macro-properties, such as elevated temperature strength and creep behavior, is not well understood which can limit their use in extreme temperature applications. Anecdotal evidence gathered of Ta-C phases has shown critical links between microstructure morphology, processing and properties. Thus, there is a need to conduct a study on the fundamental relationships between processing, properties and microstructures in this class of high temperature materials. The first step in such a study is to understand the relationship of how processing controls microstructure. From this understanding, developing testing means to determine how properties relate to microstructures is required. This is extremely relevant when one considers that tantalum carbide phases have melting temperatures beyond 3000 °C. With a testing apparatus developed, the properties can be measured. The successful completion of which will bring tailored microstructures that meet the thermo-mechanical requirements for high

temperature applications. Such research will provide a broader impact in establishing the fundamental insights into how micro-chemistry and processing develops microstructures.

## 1.2 Technical Background

The tantalum carbide, Ta-C, binary system shown in the phase diagram, figure 1, has a wide range of carbon compositions. The  $\gamma$ -TaC phase exhibits a maximum in the solidus near 4000 °C which is one of the highest melting temperature material known [7]. The TaC phase is a B1 compound, i.e. the rock-salt structure, and is shown in figure 2(a) [7,8]. For the carbon deficient species, a Ta<sub>2</sub>C phase can precipitate at temperatures below 3300 °C [2]. This phase consists of hexagonal metal layers separated between either an  $\alpha$ -ordered or  $\beta$ -disordered carbon sublattices. The Ta<sub>2</sub>C allotropic phase transformation between  $\alpha$  (CdI antitype structure) to  $\beta$  (L'3 structure) is near 2000 °C [7,8] and a representative  $\beta$ -Ta<sub>2</sub>C crystal is shown in figure 2(c). In addition, a metastable  $\zeta$ -Ta<sub>4</sub>C<sub>3</sub> phase, which is rhombohedral space group R<sub>3</sub>m [9], can form and will be discussed in detail below. The ultra-high melting temperature of TaC and its ability to form Ta-rich sub-stoichiometric phases with similar high melting temperature offers the microstructure engineering opportunities to tailor this system for ultra-high temperature thermo-mechanical applications [10].

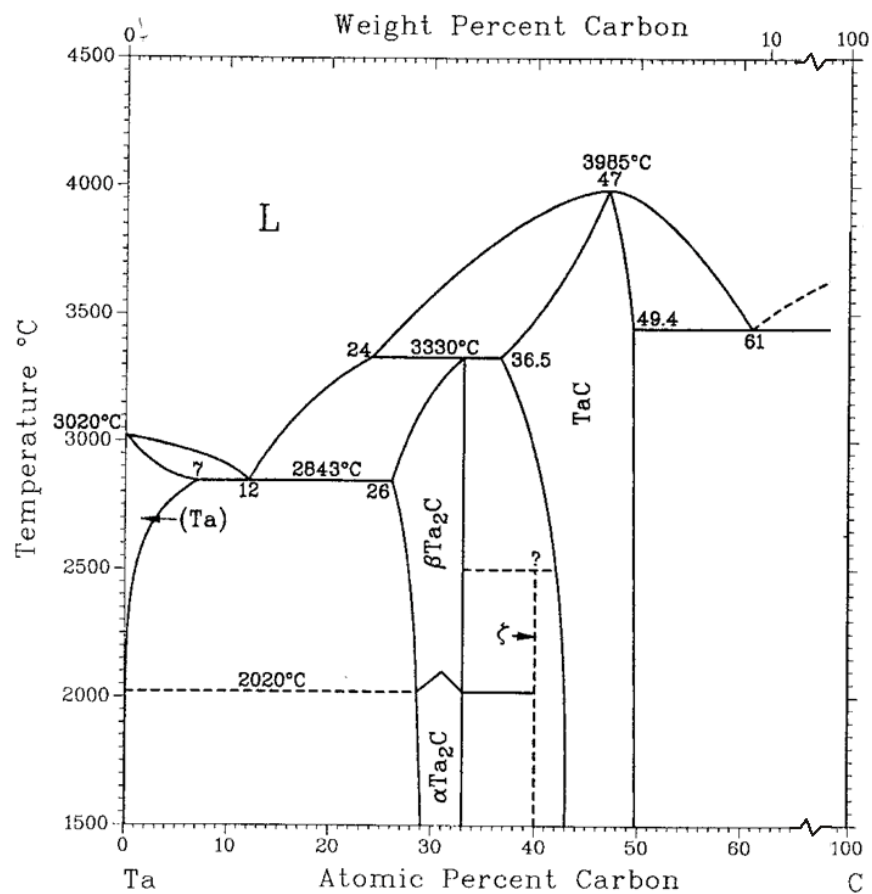


**Figure 1:** The tantalum-carbide phase diagram [11].

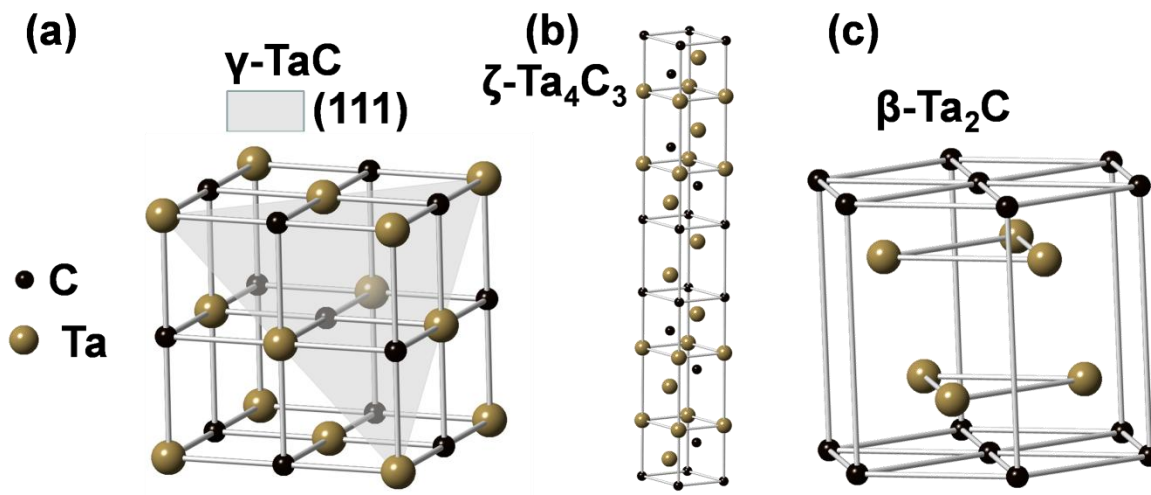


**Figure 2:** (a) The  $\gamma\text{-TaC}$  phase is a B1 compound, i.e. the rock-salt structure. (b) The rhombohedral  $\zeta\text{-Ta}_4\text{C}_3$  crystal structure. (c) The hexagonal  $\beta\text{-Ta}_2\text{C}$  crystal structure.

The formation of Ta<sub>2</sub>C out of a TaC phase field occurs below ~3400 °C. This transformation is extremely difficult, if not impossible, to suppress with rapid quenching [7]. There is speculation on the exact mechanism for the phase transformation. A suggested phase transformation mechanism is the Ta<sub>2</sub>C phase forms from the hexagonal stacking faults that can develop between two partial Shockley dislocations in the fcc-like TaC phase [12]. The nucleation of this new phase would be perpendicular to the stacking plane requiring the movement of metal atoms to the interstitial sites. The kinetics of this shear transformation would be controlled by the rate of carbon diffusion and would likely require a ‘ledge growth mechanism’ for thickening the lamella [13].

The orientation relationship (OR) between TaC and Ta<sub>2</sub>C is {111}TaC//{0002} Ta<sub>2</sub>C and <110>TaC//<1010>Ta<sub>2</sub>C and is a low energy interface [14]. Consequently in the formation of these phases, the structure of the microstructure will be highly dependent on maintaining this or similar low energy ORs.

The ζ-phase Ta<sub>4</sub>C<sub>3</sub> is formed from a diffusionless transformation in carbon deficient TaC [15]. Brizes [13] suggests that ζ-phase Ta<sub>4</sub>C<sub>3</sub> forms on cooling as a result of decreasing solubility of carbon in stoichiometric monocarbide. The zeta phase epitaxially grows off of the TaC phase when the temperature is too low to transform directly into Ta<sub>2</sub>C. Rudy and Harmon [16] noted it took 400 hours at 1700 °C to decompose the ζ-phase. While there are many reports of the zeta-phase [8,9,13,15,17], information on the formation and high resolution microscopy studies are limited.

### 1.3 Processing Dependent Microstructures

Both processing and the composition play an important role in the types of microstructures that can form. Small changes in the carbon content generate significant changes in the grain morphology of both the HIP and VPS tantalum carbides, as seen in figure 3. The figure shows a tantalum carbide microstructure whose carbon content is varied from 44 at % to 32 at %. Grain shape is shown to transition from equiaxed to acicular then back to equiaxed with decreasing carbon content. The morphology of the grain structure, which can control the mechanical properties, is dependent not only on the carbon content, but also the way the methods used for the fabrication of the tantalum carbides. Understanding the roles that the composition and processing play in the formation of tantalum carbides will allow for the ability to tailor the microstructure to the desired characteristics.

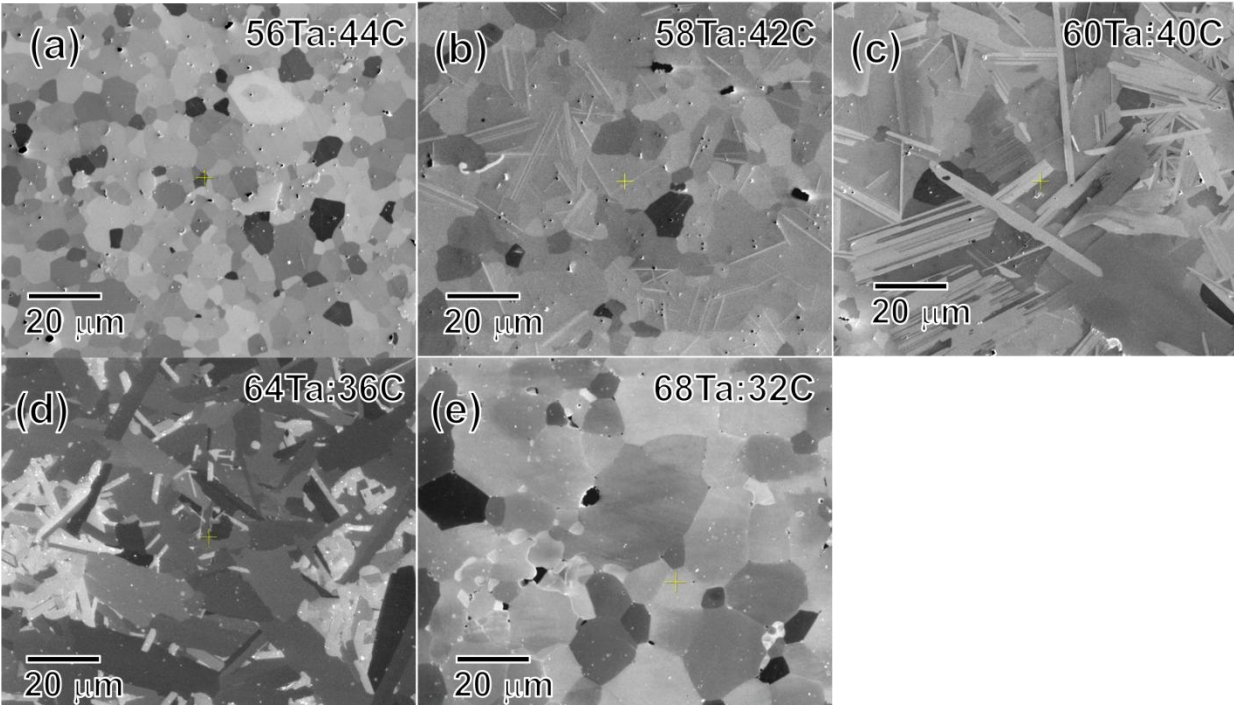


**Figure 3:** Variation in HIP tantalum carbide microstructures for different carbon compositions. (a) 56Ta:44C. (b) 58Ta:42C. (c) 60Ta:40C. (d) 64Ta:36C. (e) 68Ta:32C.

The high melting temperatures of the tantalum carbides requires fabrication by either hot-isostatic pressing (HIP) and/or vacuum plasma spraying (VPS). The fundamental differences in these manufacturing routes, described below, create variations in microstructures. HIP'ing involves solid-state diffusion of constituent powder mixtures with relatively slow heating and cooling rates as compared to VPS. Unlike nominal hot pressing and sintering, the use of simultaneous high pressures allows significant plastic flow in the billet which can yield near theoretical densities [18,19]. By reducing the porosity defects, the reliability of the mechanical-microstructure deformation data is increased. For these studies, a variety of HIP samples have

been supplied to the research program by Stephen DiPietro, Exothermic, Inc. (Amherst, NH). The HIP processing parameters are proprietary to Exothermics, Inc.

In the VPS method, the tantalum carbide powders are fed into a plasma torch where the powder is melted. Unlike the HIP process, the tantalum carbide goes through a liquid to solid transformation which can change the microstructure. Balani *et al.* [20] investigated the microstructural and mechanical properties of a VPS TaC material. In their findings, the VPS method produced near-isotropic mechanical behavior. The plasma arc provides a high temperature environment to enable the Ta-C powders to liquefy. The liquid metal is then deposited onto a graphite mandrel and rapidly solidified. The VPS process can result in a loss of carbon via vaporization as well as lower density in the as-sprayed condition. In order to increase the density, the VPS samples are sintered and then HIP'ed. The VPS samples were supplied to the research program through collaboration with Dr. Daniel Butts, Plasma Processes Inc. (Huntsville, AL). The VPS processing parameters are proprietary to PPI.

In addition to the characterization of tantalum carbide microstructure, the understanding of the formation of oxide inclusions and porosity in tantalum carbide is important as these can alter the mechanical responses of the material [21]. Previous works [22,23,24] have studied the oxidation of different carbide materials, but these have been processed in highly oxidizing environments. There are limited studies of the formation of oxides in this system [25,26]. The formation and subsequent morphology of the oxide requires characterization. Additionally, studies of the inherent formation of porosity in tantalum carbides are limited [20]. The porosity has been found to affect the mechanical properties in tantalum carbides as show by Kim *et al.* [27].

The dramatic differences in heating and cooling rates between the two processes could have an impact on the phase forming steps which will facilitate differences in the microstructures. HIP and VPS processing of tantalum carbides with varying compositions affects the precipitation of the different  $Ta_xC_{1-x}$  phases and their effect on the final microstructure. The lack of a detailed microscopy-based study of these microstructures inhibits conclusively understanding of how these microstructures and phases are formed and thereby engineered. The microstructure morphologies are explained by the phase content and sequence of precipitation. This dissertation studies the transformation, nucleation and growth of the tantalum carbide phases by exploring different micro-chemistry changes as a function of manufacturing.

#### 1.4 Thermo-mechanical Testing

For ultrahigh temperature ceramics (UHTC), quantifying the thermo-mechanical properties can be challenging because of the inability to access temperature regimes where intrinsic deformation modes are initiated [28,29,30,27,28]. Since bulk lattice diffusion, which can have a dramatic effect on mechanical responses, initiates at approximately one-half or higher the melting temperature, the ability to probe temperatures  $> 2000$  °C for UHTC is crucial. These testing limitations are usually because of inadequate heating capability, compliance in the testing rig at these temperatures, and/or chemical reactions between the testing specimens and testing fixtures or the environment [31]. In particular,  $\gamma$ -TaC has a melting temperature near 4000 °C and has one of the highest melting temperatures known [7]. Additionally,  $\gamma$ -TaC exhibits a brittle-to-ductile behavior at temperatures  $> 1500$  °C [7]. In general most testing rigs, such as four point bending units encased in a graphite filament furnace, are only able to provide temperatures a few hundred degrees higher than this transition temperature. These temperatures are below temperatures where creep based deformations could become significantly active and

changes the mechanisms and modes of deformation. To fully exploit tantalum carbides for thermo-structural loading application in extreme temperatures, the ability to quantitatively probe higher temperatures is required.

### 1.5 Dissertation Organization

The remainder of this work describes key findings of tantalum carbide microstructure evolution through two processing routes. The dissertation is organized in a journal paper format, per the guidelines of The University of Alabama's Graduate School. Chapter 2 is a discussion on the role that carbon content in controlling the microstructure in HIP processed tantalum carbide alloys. A variety of samples with specifically varied carbon content along with a diffusion couple are examined. Chapter 3 is a similar discussion, but analyzes the microstructures that form through VPS processing. Chapter 4 is a discussion on the formation of oxide inclusions and pores within the VPS processed tantalum carbide system. Finally, Chapter 5 introduces an improvement to an existing design to thermo-mechanically test UHTC, specifically applied to tantalum carbides. Chapter 6 is a summary of the results from the research and suggestions for future work. An appendix is included that provides a standard operating procedure for serial sectioning specimens on a focus ion beam microscope.

## CHAPTER 2

### MICROSTRUCTURAL FORMATIONS AND PHASE TRANSFORMATION PATHWAYS IN HOT ISOSTATICALLY PRESSED TANTALUM CARBIDES<sup>1</sup>

#### Abstract

A series of  $\text{XTa:(1-X)C}$  ( $0.5 < X < 1$ ) atomic compositions have been fabricated by hot isostatic pressing (HIP) of TaC-Ta powder blends. Depending upon the targeted stoichiometry, a single or dual phase microstructure can be formed. The single phase microstructure consisted of equiaxed grains. The dual phase microstructure was found to have grain morphology of either equiaxed grains with refined secondary phase laths encased in the grains in multiple orientations or acicular shaped grains with secondary phase laths parallel to the major axis of the grains. The effect of the phase transformations on the resultant microstructure is discussed and compared to a diffusion couple of TaC-Ta powder processed under the same HIP conditions. The diffusion couple revealed the depletion of carbon from TaC and its reaction with tantalum with its subsequent phase transformation-microstructure morphologies for each  $\text{Ta}_x\text{C}_{1-x}$  phase. The specimens have been characterized using Focused Ion Beam and Scanning Electron Microscopy, X-ray Diffraction, and Transmission Electron Microscopy techniques.

---

<sup>1</sup> A manuscript has been prepared for the work in this chapter for the publication in Acta Materialia as : R.A. Morris, B. Wang, and G.B. Thompson, "Microstructural Formations and Phase Transformation Pathways in HIP Tantalum Carbides."

## 1. Introduction

One of the significant challenges of developing tantalum carbides ( $Ta_xC_{1-x}$ ) and other similar refractory compounds is their high melting points. Though advantageous for ultrahigh temperature applications, the production of fully dense, near net shape structures limits the ability for easy manufacturing. Additionally, for this system, decarburization during annealing provides challenges in controlling stoichiometry. Hot-isostatic pressing (HIP) involves solid-state diffusion of constituent powder mixtures with relatively slow heating and cooling rates as opposed to other fabrications methods such as vacuum plasma spraying and arc melting of powders [1]. While the constituent powders themselves can off-gas, volatilization can be minimized within a confined can which houses the powders providing processing control of the Ta/C molar ratios. Additionally, a well blended mixture of powders can reduce or eliminate significant compositional gradients in the final product. Finally, the significant plastic flow in the billet, because of the high temperatures and pressures, can yield near theoretical densities [2].

The TaC phase has a melting temperature near 4000 °C, which is one of the highest melting temperature materials known [3]. Consequently, tantalum carbide has been proposed for thermal heat protection, automotive wear resistant liners, and other types of thermo-mechanical loading applications [4,5,6]. The TaC phase is a B1 compound with carbon atoms occupying the octahedral interstitial sites in a tantalum face-centered-cubic lattice. [3,7] For carbon deficient phases, a  $Ta_2C$  phase can precipitate at temperatures below 3500 °C [8,9], as seen in the phase diagram by Barabash *et al.* [10] in figure 1. This phase consists of hexagonal metal layers separated between either an  $\alpha$ -ordered or  $\beta$ -disordered carbon sublattice. The allotropic phase transformation between  $\alpha$ - $Ta_2C$  (CdI antitype structure) to  $\beta$  ( $L'3$  structure) is near 2000 °C

[3,7]. In addition, a  $\zeta$ -Ta<sub>4</sub>C<sub>3</sub> phase, which is rhombohedral with the space group R<sub>3m</sub>, can form at 2500 °C [11,12]. The thermodynamic stability of the  $\zeta$ -Ta<sub>4</sub>C<sub>3</sub> phase is still under discussion [11]. The ultra-high melting temperature of TaC and the ability to precipitate similar high melting temperature phases offers several microstructure engineering opportunities to tailor this system for high temperature thermo-mechanical applications [13]. In the present paper, we report how HIP processing of tantalum carbides with varying compositions affects the precipitation of the different Ta<sub>x</sub>C<sub>1-x</sub> phases and their effect on the final microstructure.

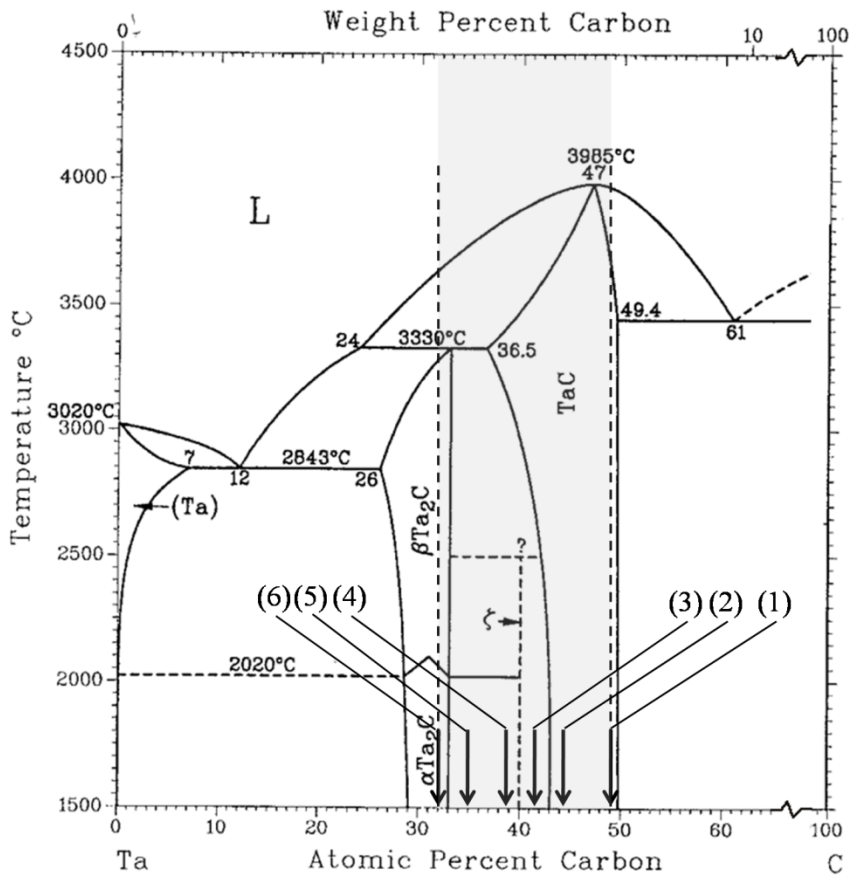


**Figure 1:** Ta-C binary phase diagram showing a highlighted region of the Ta/C content obtained for each specimen investigated. Phase diagram from reference [8].

## 2. Experimental Procedures

Six specimens of various Ta/C ratios were prepared with compositions, tabulated in Table 1, which placed them in either the single or two phase region, figure 1. The compositions are listed in atomic percent. In addition, a diffusion couple was formed from the stack of TaC powder on top of Ta powder. The powders were purchased from Cerac, Inc. and their starting size distribution was measured from scanning electron microscopy images using the Nikon Elements® imaging analysis software package. The powders were placed into tantalum can containers prior to HIP processing in an environmentally controlled glove box to eliminate any extraneous contamination. The tantalum containers were then evacuated and welded closed and subsequently HIP'ed at 200 MPa in an argon atmosphere at 1600°C.

**Table 1:** Tabulated data for the specimens prepared. The far left column contains the targeted or weighed amount compositions, the XRD is the estimated volume fraction of the phases determined by the integrated intensity ratio of the peaks from figure 3(f), and the lever rule is the compositions based on the XRD volume fraction estimations.

Samples/Phase	XRD			Lever rule	
	TaC	Ta <sub>4</sub> C <sub>3</sub>	Ta <sub>2</sub> C	Ta	C
(1) 51Ta:49C	100	0	0	51	49
(2) 56Ta:44C	100	0	0	56	44
(3) 58Ta:42C	96	4	0	58	42
(4) 60Ta:40C	49	33	17	61	39
(5) 64Ta:36C	7	36	57	65	35
(6) 68Ta:32C	0	0	100	68	32

Post-HIP, the XTa:(1-X)C specimens were removed from the tantalum can and were mechanically cut into two pieces. The ‘interior’ portions of the XTa:(1-X)C specimens were examined for the subsequent analysis. The specimens were mounted in cross-section,

mechanically ground and polished to 3 micron diamond abrasive paste and then Vibromet® polished for 24 hours in aqueous 0.05 micron silica slurry.

The microstructures were imaged using either secondary electrons or ion contrast imaging in a FEI Quanta 3D dual beam focus ion beam (FIB) - scanning electron microscope (SEM) operated at 30 keV. Electron backscatter diffraction (EBDS) patterns, used for phase identification, were collected using the EDAX-TSL platform with the Hikari camera attached to the FEI Quanta 3D microscope. The specimens were tilted 70° towards the detector and scanned at 100 frames per second at an electron beam of 30 keV and 5.0 nA.

X-ray diffraction for phase identification and estimated volume fraction determination was done using a Bruker Discovery D8 General Area Diffraction Detector System with Cu-K $\alpha$  radiation at 45 keV and 40 mA as the source. The TaC, Ta<sub>2</sub>C, and  $\zeta$ -Ta<sub>4</sub>C<sub>3</sub> phases were identified using data from Wyckoff, Lissner [8], and Gusev *et al.* [11] sources, respectively. The phase content is tabulated in Table 1 and was estimated by the integrated intensity of the theoretically most intense peak for each phase divided by the sum of all maximum peak intensities [15]. These peaks were the following: {111}<sub>TaC</sub>, {107}<sub>Ta<sub>4</sub>C<sub>3</sub></sub>, and {1011}<sub>Ta<sub>2</sub>C</sub> reflections [14,11,8]. The lever rule compositions used the XRD determined volume fractions of each phase and had good agreement to the initial powder Ta-C ratios.

For the diffusion couple specimen, SEM-Energy dispersive spectroscopy (EDS), collected on an EDAX Apollo XV silicon drift detector, at an electron beam setting of 10 keV and 3.3 nA, was used to determine the approximate Ta and C composition across the reaction interface. A standard 51Ta:49C specimen was used for calibrating the EDS instrument. The large difference in atomic number of Ta to C can result in the preferential absorption of carbon x-rays

by tantalum but, surprisingly, there was good agreement of the EDS data to the standard to provide confidence in the diffusion couple Ta/C measurements. As will be shown later, the compositions matched the required phases determined by the various crystallographic scattering techniques.

(Scanning) transmission electron microscopy ((S)TEM) was performed using an FEI F20 Tecnai operated at 200keV. Correlated bright field and dark field imaging with electron diffraction was used for phase and microstructure identification. Complimentary atomic, or Z-, contrast imaging, using a High Angle Annular Dark Field (HAADF) detector was done in a STEM mode. The HAADF collects scattered electrons that are relatively insensitive to crystallographic dependent (Bragg) scattering; therefore, the contrast observed is chemically dependent with higher atomic number elements being brighter [16]. TEM samples were prepared using both traditional and FIB milled techniques. [17,18] Traditional TEM foil preparation involves sectioning and thinning a 3mm disc of a desired region of the specimen after which a dimple is milled in the middle of the disc. An ion mill is then used to cause perforation resulting in an electron transparent region near the perforated areas of the specimen. FIB milling allowed for site specific extraction and thinning TEM sample preparation using the FEI Quant 3D dual beam FIB.

### 3. Results

#### i. *Initial Powders*

The average size of the Ta powder was found to be  $48 \mu\text{m} \pm 25 \mu\text{m}$ . The Ta powders exhibited a large variation in size, as shown in the distribution histogram in figure 2(a), with a greater number of powders in the range of  $\sim 20$  to  $\sim 40 \mu\text{m}$ . In addition, these powders were composed of small conglomerated Ta particulates, shown in figure 2(b). Figure 2(c) shows the

nodal structure of these Ta powders. The TaC powder size was considerably smaller,  $2.7 \mu\text{m} \pm 0.7 \mu\text{m}$ , and more uniform in size, figure 2(d). Though the nodal morphology of the TaC and Ta powders were similar, the TaC powders were qualitatively less conglomerated than the Ta powders, comparing each in figures 2 (b-c) to (e-f). As will be discussed in detail in the proceeding sections, there is a trend of the grain size of the resultant HIP microstructures as related to the starting powder sizes.

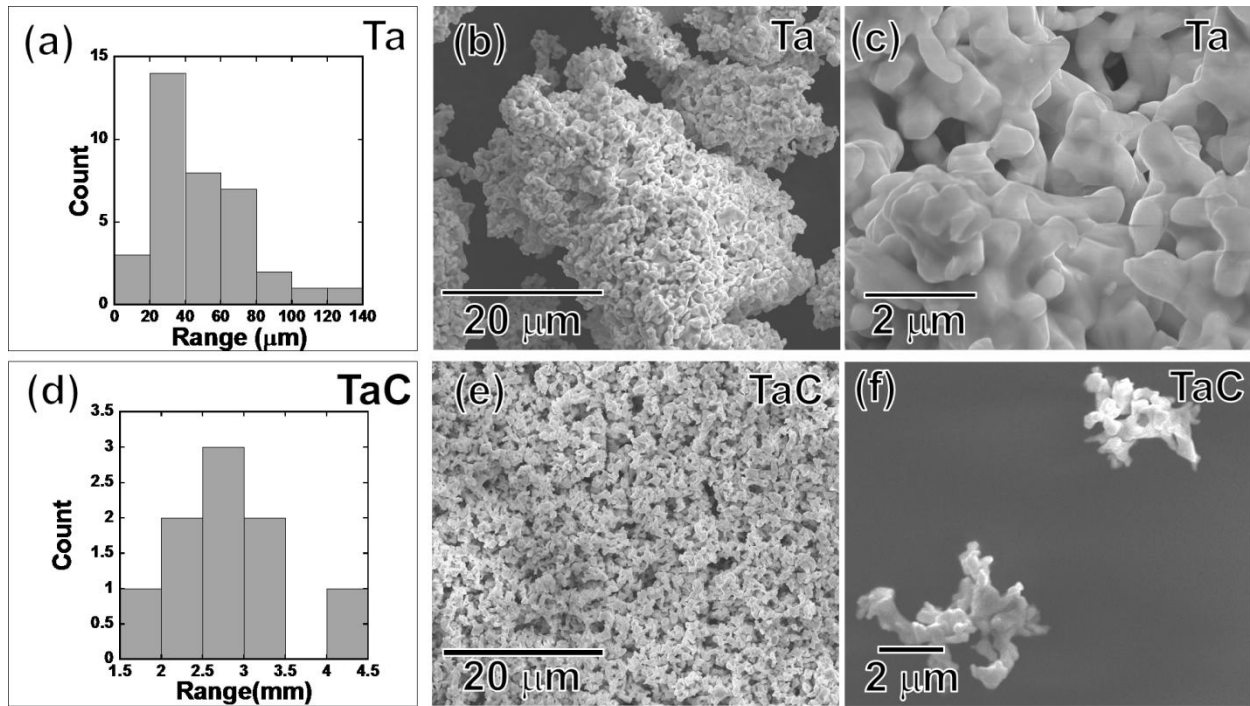


**Figure 2:** Grain size data and SEM Images from the initial Ta and TaC powders used in the fabrication of the  $\text{XTa}:(1-X)\text{C}$  specimens. **(a)** Distribution histogram of the grain sizes of the Ta powder. **(b-c)** SEM image of the Ta powder showing the conglomerated nature of the Ta powders. **(d)** Distribution histogram of the grain sizes of the TaC powder. **(e)** SEM image of the TaC powder. **(f)** SEM image of two separated TaC powders showing the nodal nature of the powder.

ii. XTa:(1-X)C Compositions

The XTa:(1-X)C specimens, where X = 51, 56, 58, 62, 65, and 68 at. %, were processed to span the range from single phase TaC to single phase Ta<sub>2</sub>C, with their multiphase microstructures in between. As noted in the experimental section, the desired compositions, determined by the starting TaC/Ta ratios, were in close agreement to the post-processed HIP compositions determined by either the XRD volume fraction lever rule or EDS. This confirms that minimal carbon changes occurred during the processing preserving the desired phase hence microstructure to be studied. Grain size analysis was performed on the single composition specimens, whose results are shown in Table 2. Along with mean grain size, average maximum Feret, also known as long axis measurements, were made. The maximum Feret diameter represents the longest dimension of the particle [19]. This measurement is useful for quantifying the non-equiaxed nature of the acicular grain morphologies.

**Table 2:** Grain size analysis data for the XTa:(1-X)C specimens.

Samples/grain size	Mean Diameter, $\mu\text{m}$		Mean Long axis, $\mu\text{m}$	
(1) 51Ta:49C	2.2	$\pm 0.7$	2.8	$\pm 0.9$
(2) 56Ta:44C	5.2	$\pm 2.0$	7.0	$\pm 4.0$
(3) 58Ta:42C	8.9	$\pm 3.6$	11.9	$\pm 5.2$
(4) 60Ta:40C	9.6	$\pm 5.0$	18.0	$\pm 11.1$
(5) 64Ta:36C	6.1	$\pm 4.0$	11.0	$\pm 7.7$
(6) 68Ta:32C	23.0	$\pm 8.8$	29.0	$\pm 10.8$

The 51Ta:49C (not shown) and 56Ta:44C specimens were both found to be single phase TaC with an equiaxed grain microstructure, with the XRD phase identification shown in figure

3(a) and representative micrograph in figure 3(b). The TaC phase has a range of carbon solubility while still retaining the B1 structure, as evident in the phase diagram in figure 1 and confirmed for the two compositions prepared. The TaC lattice parameter is sensitive to carbon content. While the XRD for both 51Ta:49C and 56Ta:44C specimens indicate single phase TaC, a clear XRD shift between the specimens does exist in figure 3(a). This XRD shift is in the direction of a smaller d-spacing, which would correspond to a sub-stoichiometric TaC carbon content. The Ta<sub>51</sub>C<sub>49</sub> specimen was found to have a similar grain size,  $2.2 \pm 0.7 \mu\text{m}$ , to that of the starting TaC powder,  $2.7 \pm 0.7 \mu\text{m}$ , showing that there was not a significant amount of grain coarsening during the HIP process for this specimen. The 56Ta:44C specimen, which had a small amount of elemental Ta powder in the blend, had an increase in grain size,  $5.2 \pm 2.0 \mu\text{m}$ , as compared to the 51Ta:49C specimen. Recall that the Ta starting powder is larger than the TaC starting powder. As expected with the equiaxed grain shape, the maximum Feret length was similar to the mean grain size for both the 51Ta:49C and 56Ta:44C specimens.

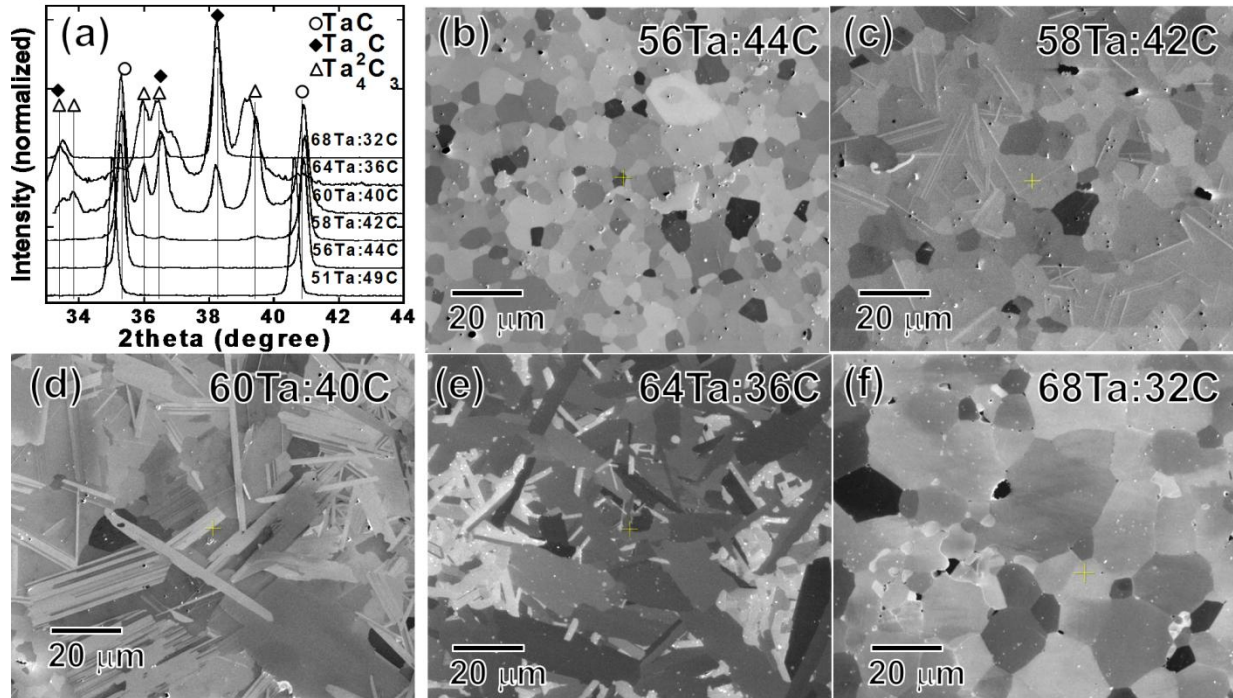


**Figure 3:** XRD and FIB micrographs of XRD data of the XTa:(1-X)C specimens (a) XRD data of the XTa:(1-X)C specimens showing the different phases present depending on composition. Note the variation in TaC peak angle between the 51Ta:49C and 56Ta:44C specimen, indicating a change in carbon content. (b) FIB image of the 56Ta:44C specimen showing an equiaxed single phase TaC microstructure. (c) 58Ta:42C specimen showing precipitated secondary phase laths encased within an equiaxed TaC grain microstructure. (d) 60Ta:40C specimen showing an acicular microstructure with large amounts of secondary phase laths. (e) 64Ta:36C specimen showing an acicular microstructure with a majority of the Ta<sub>2</sub>C and Ta<sub>4</sub>C<sub>3</sub> phases. (f) 68Ta:32C specimen showing an equiaxed single phase Ta<sub>2</sub>C grain microstructure.

The 58Ta:42C specimen had a composition within the two phase field of TaC and Ta<sub>4</sub>C<sub>3</sub>, as shown in the phase diagram in figure 1. XRD of the 58Ta:42C specimen showed a majority of the TaC phase with minor intensity reflections for the Ta<sub>4</sub>C<sub>3</sub> phase. The phase content for this specimen was found to be ~ 96 vol % TaC and 4 vol. % Ta<sub>4</sub>C<sub>3</sub>. The equiaxed grain shape was similar to that of the 51Ta:49C and 56Ta:44C specimens, but the SEM micrographs in figure 3(c) clearly indicates multi-directional Ta<sub>4</sub>C<sub>3</sub> phase laths, which we [20] as well as others [21] have reported to be the precipitation of Ta<sub>4</sub>C<sub>3</sub> on the TaC's {111} planes within the TaC grains.

Also, there was found to be a slight increase in grain size, to  $8.9 \pm 3.6 \mu\text{m}$ , continuing the trend of increasing grain size with increasing Ta powder amounts in the blend.

The 60Ta:40C specimen was found to form a greater amount of these secondary phases, as shown in the SEM micrograph in figure 3(d) by the elongated bands or laths. The XRD spectra, figure 3(a), confirmed the increase in  $\text{Ta}_4\text{C}_3$  and  $\text{Ta}_2\text{C}$  phase content as evident by their higher intensity peaks. The resultant volume fraction of these phases for this specimen was 49 vol.% TaC, 34 vol. %  $\text{Ta}_4\text{C}_3$  and 17 vol. %  $\text{Ta}_2\text{C}$ . The grain structure of this specimen is no longer equiaxed but changed to an acicular grain morphology. Unlike the 58Ta:42C specimen, where the laths were multi-directional, in the 60Ta:40C specimen the laths were found to form along preferential directions in each of the grains, which would suggest orientation dependent controlled growth. While the 60Ta:40C specimen is composed of nearly half TaC phase, the increase content of secondary phases has a marked influence on microstructure grain morphology. This influence was characterized in the grain size analysis. The mean grain size diameter was found to be  $9.6 \pm 5.0 \mu\text{m}$ , and notably, the maximum Feret length was found to be over twice the grain size, with a mean value of  $18.0 \pm 11.1 \mu\text{m}$ , confirming that the grain shape are non-equiaxed.

With further depletion in the carbon content, the XRD spectra for the 64Ta:36C specimen, as expected, showed a continual decrease in the TaC phase content and an ever increasing amount of  $\text{Ta}_4\text{C}_3$  and  $\text{Ta}_2\text{C}$ , figure 3(a). Similar to 60Ta:40C, 64Ta:36C exhibited an acicular grain structure, figure 3(e). The phase amounts were determined to be 7 vol. % TaC, 36 vol. %  $\text{Ta}_4\text{C}_3$ , and 57 vol. %  $\text{Ta}_2\text{C}$ . As with the 60Ta:40C specimen, the 64Ta:36C specimen had a grain size analysis that showed the maximum Feret length to be  $11.0 \pm 7.7 \mu\text{m}$ . The grain

morphology had a wide range of grain sizes, with figure 3(e) showing interconnecting large and small grains.

The 68Ta:32C composition places it into the single Ta<sub>2</sub>C phase field. The XRD spectra, figure 3(a), confirmed that this was the only phase present. Similar to the single phase TaC, this specimen exhibited an equiaxed grain microstructure, figure 3(f). A comparison of the single phase TaC and Ta<sub>2</sub>C grains, figure 3(b and f), and their mean grain diameters, Table 2, shows a large difference in the grain sizes. As noted previously, the grain sizes for each of the specimens, listed in Table 2, shows a general increasing trend of grain size with increasing Ta content.

### iii. TaC-Ta Diffusion Couple

A diffusion couple was fabricated using TaC powder placed adjacent to Ta powder and then processed using the same HIP procedure of 1600 °C at 200MPa. The diffusion couple allows for the creation of different regions with a varying compositional gradient used to elucidate the method of the phase transformation and subsequent microstructure formations. Starting on the TaC side of the diffusion couple and progressing towards the Ta side, the microstructure was found to have seven specific and different regions with each region corresponding to different carbon compositions, shown in figure 4(a-c). These regions are the following:

- [A] Equiaxed single phase TaC
- [B] Equiaxed TaC grain structure with laths of  $Ta_4C_3/Ta_2C$  encased within the matrix.
- [C] Small equiaxed TaC or  $Ta_2C$  grains
- [D] Acicular  $Ta_2C$  grains
- [E] Equiaxed single phase  $Ta_2C$
- [F] Mixture of equiaxed  $Ta_2C$  and Ta grains
- [G] Equiaxed Ta grains

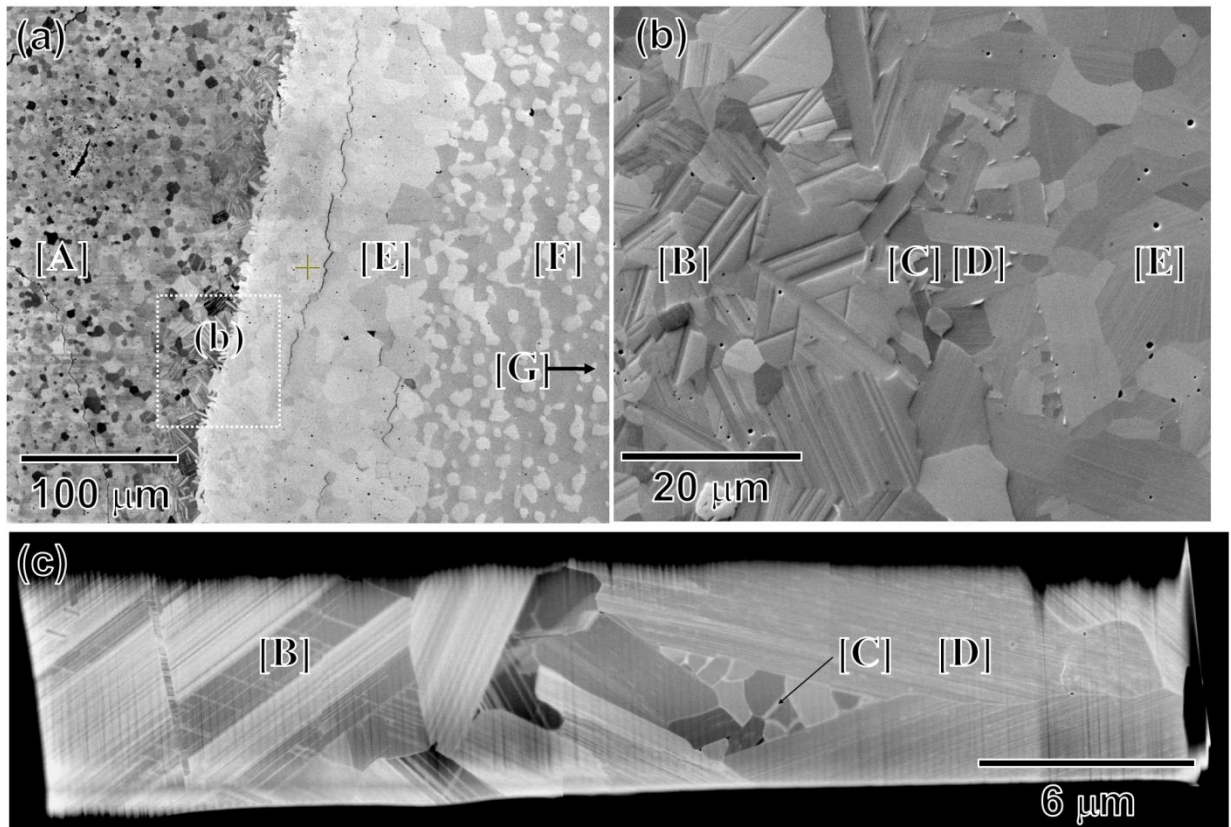


**Figure 4:** FIB and STEM-HAADF images of the labeling method used in the diffusion couple (a) SEM image of the diffusion couple showing the single phase TaC labeled as [A] through the mixture of  $Ta_2C$  and Ta grains labeled as [F] with the equiaxed Ta grain region [G] (not shown). (b) Enlarged region of (a) showing the different microstructures along the TaC/ $Ta_2C$  interface. (c) STEM image of the TaC/ $Ta_2C$  interface showing the secondary phase laths that form within the grains. Foil prepared by FIB-based milling extraction [17].

Both EDS and XRD line scans were performed on the diffusion couple to characterize the different regions that formed. The EDS line scan, dark arrow in figure 5(a), shows the relative microstructural location with respect to how carbon content fluctuated across the couple, figure 5 (b). The EDS line profile shows a steady decrease in the carbon content starting from approximately 50Ta:50C (TaC) and decreasing to 56Ta:44C. At the 56Ta:44C composition, a significant slope change occurs to a steady state composition of the 66Ta:33C (Ta<sub>2</sub>C). Further profiling resulted in an oscillatory carbon signal that varied between 66Ta:33C and 90Ta:10C, which corresponded to grains of either Ta<sub>2</sub>C or Ta and will be further discussed below. Though Ta has little to no solubility for carbon according to the phase diagram at 1000 °C, the interaction volume generated a carbon signal and thus the read should not assume that a solid solution of C in Ta has formed in these grains.

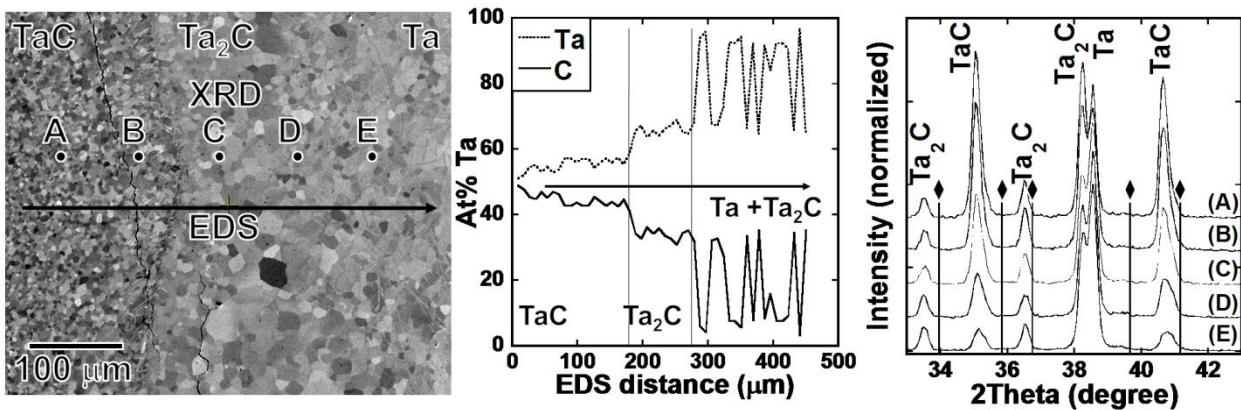


**Figure 5:** EDS and XRD line data from diffusion couple (a) SEM of diffusion couple showing the EDS and XRD line scan spot locations. (b) EDS line profile showing the different composition through the different phase of the diffusion couple. (c) XRD data for the line scan showing the variation in the amount of each phase in the diffusion couple. Note that there were no reflections corresponding to the Ta<sub>4</sub>C<sub>3</sub> phase, as indicated by the diamond shaped markers (♦).

The XRD line scan, figure 5(c), was performed over ~400 μm per ~80 μm spacing of the TaC/Ta interface to determine the phase content across the diffusion couple. The approximate

XRD positions are alphabetically marked in figure 5(a). The XRD spectra confirmed TaC, Ta<sub>2</sub>C and Ta phases. The smallest available XRD spot probe was 0.3 mm so the XRD collection volume was larger than the grains at the interface. Hence this method was not able to clearly separate specific phases and identify them to their specific spatial locations, but clear trends in the relative rise and fall in phase peak intensities is evident in figure 5(c). Regardless, the XRD and EDS line profile positions showed relatively good agreement between composition and phase content. To remedy the issue of phase position to specific grain location, EBSD phase mapping was conducted.

The EBSD phase maps are plotted in figures 6 thru 8. It is important to note that the EBSD has difficulty in distinguishing between Ta<sub>2</sub>C and Ta<sub>4</sub>C<sub>3</sub> due to their similar structure and symmetry. It can however distinguish between the TaC and Ta<sub>2</sub>C or Ta<sub>4</sub>C<sub>3</sub>. The microstructure in region [B] in figure 4(b) revealed a mixture of equiaxed and acicular grains with a lath structure encased within the grains. Figure 6(d) has identified these laths as either the Ta<sub>2</sub>C or Ta<sub>4</sub>C<sub>3</sub> phase. A closer inspection of figure 6(c-d) reveals thin dark bands that are not indexed as TaC or Ta<sub>2</sub>C. Though these phases as well as Ta<sub>4</sub>C<sub>3</sub> were placed in the search routine, the lack of identification is a result of either poor diffraction contrast and/or the size of the feature is beyond the resolution limit of our instrumentation. This reaction zone was typically 35 μm in width.

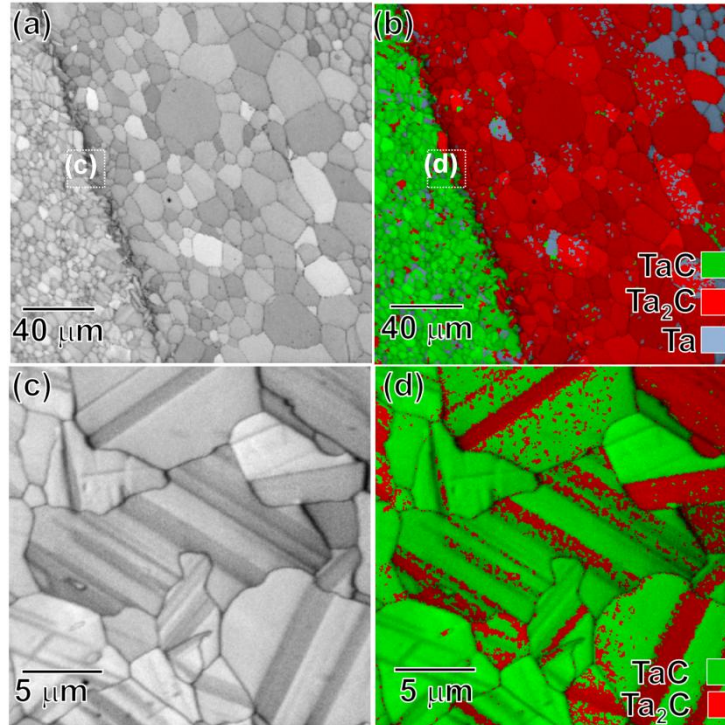


**Figure 6:** EBSD of diffusion couple. **(a)** EBSD Image quality map of the overall diffusion couple. **(b)** EBSD phase map of region in (a) showing the three phases, TaC, Ta<sub>2</sub>C and Ta. **(c)** Image quality map of the TaC grains near the TaC/Ta<sub>2</sub>C interface with the Ta<sub>2</sub>C phase showing up as dark multidirectional bands. **(d)** EBSD phase map of region in (c) showing the Ta<sub>2</sub>C phase forming within the TaC grains.

Region [C] of figure 4(b-c) contained small grains of both TaC and a sub-carbide (probably Ta<sub>2</sub>C). The EBSD phase map, figure 7(a-b), illustrated this observation. The STEM image, figure 4(c), shows that these grains were equiaxed and whose sizes were much smaller than those in the surrounding region.

The Ta<sub>2</sub>C phase next to this small grain region was found to yield acicular grains. A closer look at region [D] shows that the acicular Ta<sub>2</sub>C grains also contain very thin laths, figure 7(a-b). Region [D], as with region [C], was found to only be a few grains thick before the grain morphology changed. The SEM micrograph of the tilted surface, figure 7(c-d), reveals a topographical difference between the matrix grain and these laths within the grains. This surface

modulations results from the difference in hardness between the TaC, Ta<sub>2</sub>C and Ta phases during polishing [20].

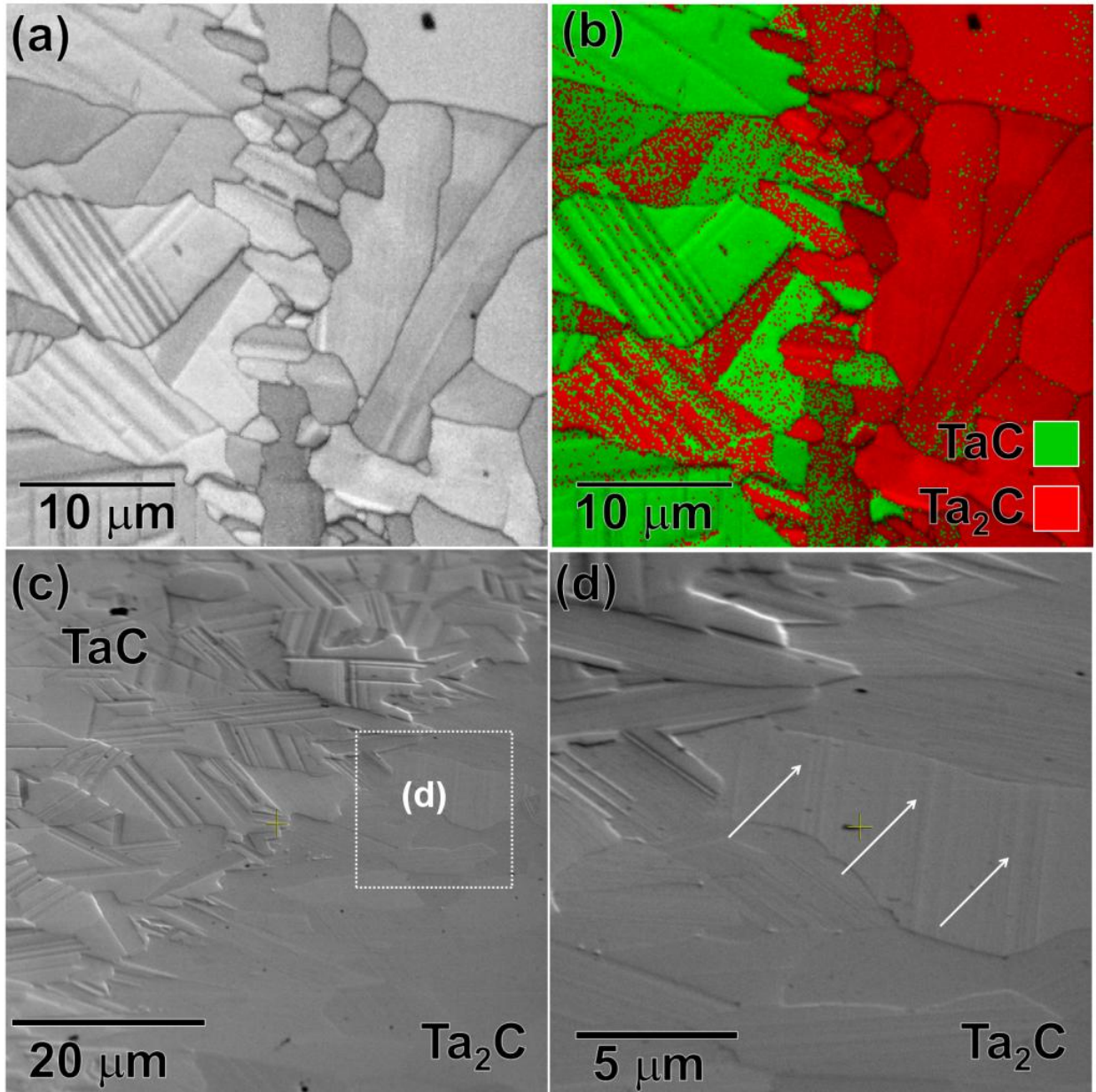


**Figure 7:** EBSD and SEM micrographs of diffusion couple (a) EBSD Image quality map of the diffusion couple of regions [B], [C] and [D]. Note the difference in the band directionality in either phase. (b) EBSD phase map of same region in (a) showing the both the TaC and Ta<sub>2</sub>C phases, with the middle smaller grains composed mostly of Ta<sub>2</sub>C. (c) SEM image of the sample

tilted to show the topography differences between the phases. **(d)** SEM image of the Ta<sub>2</sub>C phase tilted to show the unidirectional bands that formed within.

Upon approaching the Ta side of the diffusion couple, region [E] in figure 4(b), the acicular shape of the Ta<sub>2</sub>C grains changes into an equiaxed shape. The grain size becomes larger than those grains seen in the previous regions and was found to approximately 120 μm wide. As shown in figure 6(a-b), the grain size of the Ta<sub>2</sub>C phase increases moving away from the TaC/Ta<sub>2</sub>C interface until reaching region [F].

Moving further toward the Ta side of the diffusion couple, denoted as region [F], the equiaxed Ta<sub>2</sub>C grains become intermixed with the Ta phases, figure 8, with the following three distinct regions based on size:

[F] - (a): A majority of larger Ta<sub>2</sub>C grains with smaller Ta grains

[F] - (b): A mixture of equivalent sized Ta<sub>2</sub>C and Ta grains

[F] - (c): A majority of smaller Ta<sub>2</sub>C grains nucleating at the grain boundaries of the larger Ta grains.

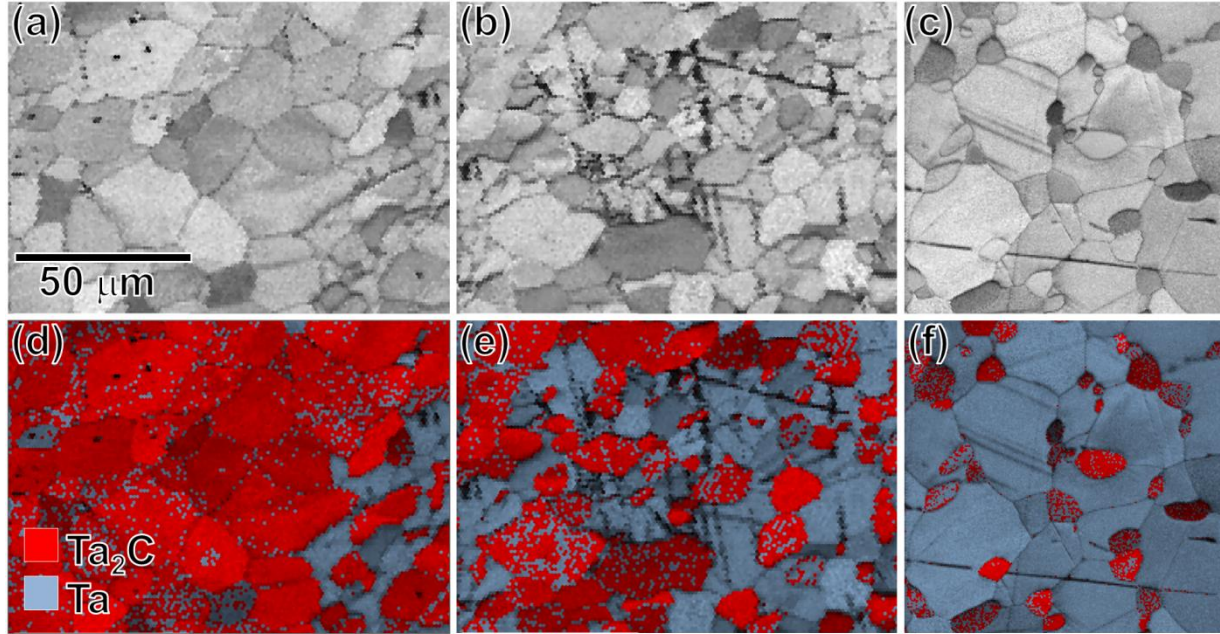


**Figure 8:** EBSD Image quality maps with corresponding phase maps of the Ta<sub>2</sub>C/Ta interface. (a and d) Ta<sub>2</sub>C side showing mostly Ta<sub>2</sub>C grains with small Ta grains. (b and e) Mixture of equi-sized Ta<sub>2</sub>C and Ta grains. (c and f) Ta side showing mostly Ta grain with Ta<sub>2</sub>C grain forming at the grain boundaries.

The average equivalent grain diameters for the different phases in the three regions are tabulated in Table 3. The change in grain size for each of the Ta<sub>2</sub>C and Ta phases is similar to one another, *i.e.* the major phase size is  $\sim 16 \mu\text{m}$  while the minor phase size is  $\sim 7 \mu\text{m}$ . At the end of diffusion couple, region [G] figure 4(a), was equiaxed Ta grains.

**Table 3:** Grain size data for figure (8). Data shows the similar grain sizes of each of the major phase, *i.e.* Ta<sub>2</sub>C grain sizes in Ta<sub>2</sub>C side and Ta grain sizes in Ta side, along with similar grain sizes for the Ta and Ta<sub>2</sub>C grains within the middle area in figure 8 (b and e).

Diameter ( $\mu\text{m}$ )	(1) Ta <sub>2</sub> C side	(2) Middle	(3) Ta Side
Ta	$9 \pm 4.1$	$11 \pm 3.5$	$17 \pm 6.9$
Ta <sub>2</sub> C	$15 \pm 5.5$	$10 \pm 4.7$	$6 \pm 2.0$

As shown in figure 4, TEM foils were prepared at the TaC/Ta interface of the diffusion couple. Figure 9(a-i) is TEM micrographs, from a different foil, of the same region. Similar to 51Ta:49C and 56Ta:44C, the foil region in figure 9(a), contained an equiaxed grain structure that was single phase TaC. The bright contrast in the STEM-HAADF image of these grain boundaries suggests that these grains are slightly enriched in tantalum. As the system began to lose carbon, or alternatively as you move towards the Ta powder direction, secondary phase Ta<sub>2</sub>C precipitated, as concluded from the selected area electron diffraction (SAED) patterns in figure 9(i) and phase map of figure 6(b). These Ta<sub>2</sub>C phases are shown as the higher intensity bands in figure 9(b-c) and correspond to region [B] in figure 4(b).

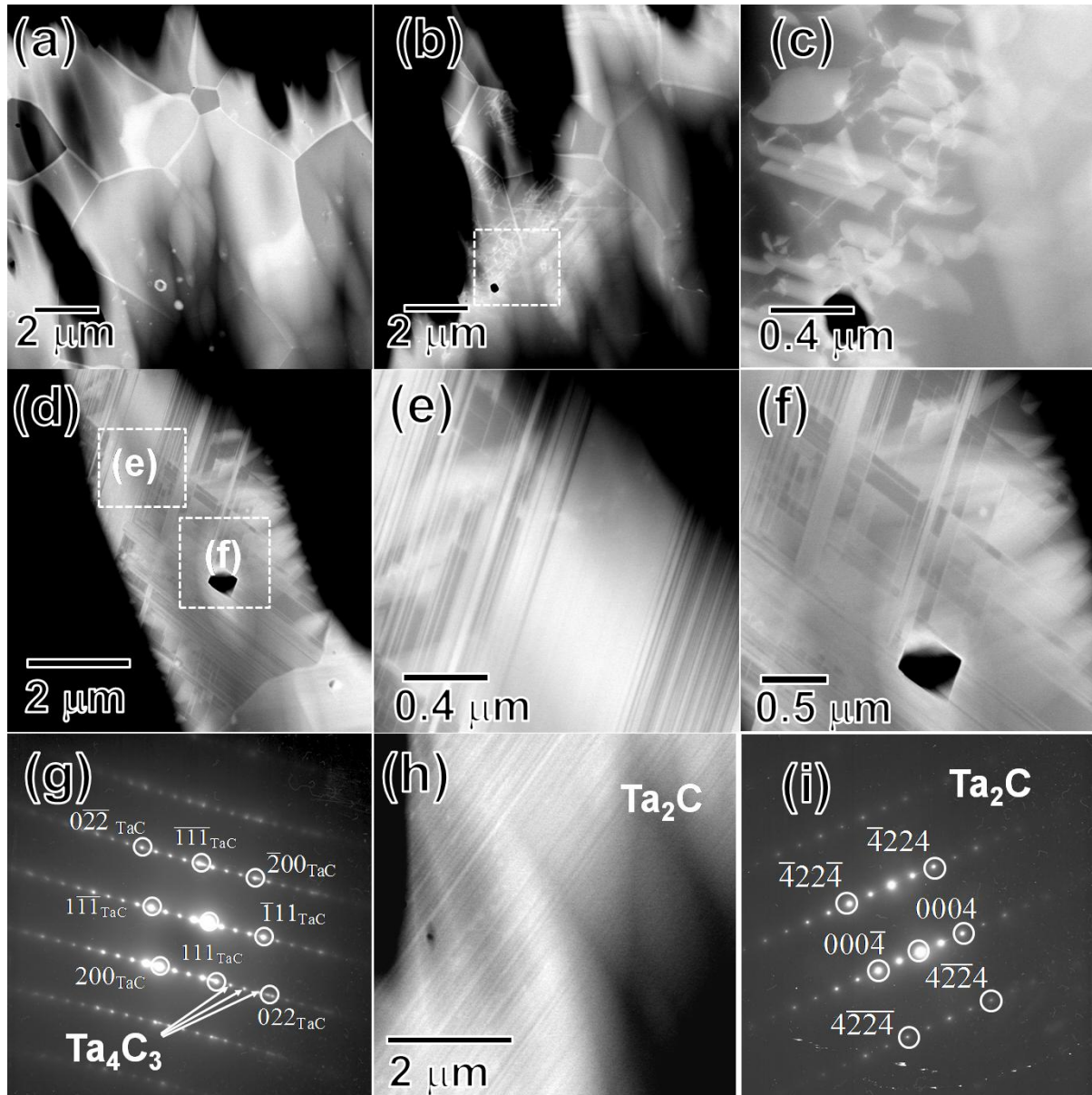


**Figure 9:** STEM-HAADF images and SAED of a conventionally prepared TEM foil of the diffusion couple. **(a)** Equiaxed TaC grains with no appreciable carbon loss. **(b)** TaC grain with the formation of Ta<sub>2</sub>C/Ta<sub>4</sub>C<sub>3</sub> phase forming as small incongruent laths. **(c)** Enlarged image of **(b)** showing the plate-like bands forming on multiple TaC {111} planes. **(d)** TaC grain with large amount of precipitated Ta<sub>4</sub>C<sub>3</sub> phase, congruently forming on a specific {111} plane, as shown in the enlarged image in **(e)**, or forming in multiple directions, as shown in **(f)**. **(g)** SAED of the high concentration Ta<sub>4</sub>C<sub>3</sub> lath area in **(e)** showing multiple spots corresponding to the Ta<sub>4</sub>C<sub>3</sub> phase along with the TaC phase. **(h)** A Ta<sub>2</sub>C grain with intense unidirectional bands that form within the grain. These bands are not uniformly spaced, but do form along the same {0001} close packed plane of the Ta<sub>2</sub>C. **(i)** SAED of grain in **(h)** showing that the spots were only identified as single phase Ta<sub>2</sub>C.

As carbon content is further lost, the density of these secondary laths increases, figure 9(d-f) and figure 4(c). These micrographs show that these bands were found to run parallel to each other, figure 9(e) and intersect each other, figure 9(f). This is very similar to the features observed in the 58Ta:42C specimen in figure 3(c). Previous work [20,21] found that these secondary phase laths intersect each other on the  $\{111\}$  planes of the TaC, which shares an orientation relationship with Ta<sub>2</sub>C of  $\{111\}_{\text{TaC}} // \{0001\}_{\text{Ta}_4\text{C}_3} // \{0001\}_{\text{Ta}_2\text{C}}$ ;  $\langle 110 \rangle_{\text{TaC}} // \langle 10\bar{1}0 \rangle_{\text{Ta}_4\text{C}_3} // \langle 10\bar{1}0 \rangle_{\text{Ta}_2\text{C}}$ . SAED of the parallel and intersecting laths, figure 9(h), identify a mixture of TaC and Ta<sub>4</sub>C<sub>3</sub> diffraction spots.

As the carbon content drives the system towards the predominate Ta<sub>2</sub>C region, region [D] in figure 4(b), the grains became acicular with the laths running parallel to the major axis of the grain (not the hatch-work patterns seen in region [B]). This is also seen in as seen in figure 4(c) and figure 9(h) and has the same closed packed orientation relationship given above. The SAED of this region, shown in figure 9(i), shows that only the Ta<sub>2</sub>C phase is present, indicating that the brighter laths seen in figure 9(h) are not a secondary phase but a possible chemical modulation because of stacking faults. More high resolution TEM is needed to clarify this situation.

#### 4. Discussion

From the results presented above, small changes in carbon content in tantalum carbides can result in the precipitation of multiple phases and significant changes in microstructures. The presence of the same phases does not necessarily result in the same microstructures. For example, consider either 58Ta:42C versus 60Ta:40C or region [B] versus [D] in the diffusion couple. In one case, 58Ta:42C and region [B] have equiaxed grains with secondary phases precipitated in multiple directions as compared to 60Ta:40C and region [D]'s acicular grains with the secondary phases precipitated parallel to each other and all along the major-axis of the grain. Complicating these issues is that these phases form through a reaction of constituent powders. Elucidating how the reaction process facilitates the nucleation and growth of secondary phases and their influence on microstructure morphologies is paramount to develop and engineer tantalum carbides microstructures.

To initiate the discussion of microstructure formation, the various grain sizes observed in the single composition specimens are reviewed. In general, the predominantly equiaxed TaC-phase materials (51Ta:49C, 56Ta:44C, and 58Ta:42C) had smaller grain sizes, between 2-9  $\mu\text{m}$ , as compared to either the major axis length of the acicular grains (60Ta:40C and 64Ta:36C), 11-18  $\mu\text{m}$ , or the equiaxed Ta<sub>2</sub>C materials (68Ta:32C), 23  $\mu\text{m}$ .

For the single phase TaC, this can be easily understood by considering the starting powder diameters. Since these powders will only sinter, and not react to form other phases, the grain size will, in general, be governed by the size distribution of the starting powder sizes [1]. The TaC powder had a mean size of  $2.7 \pm 0.7 \mu\text{m}$  and the mean grain size of the 51Ta:49C sample was 2.2

$\pm 0.7 \mu\text{m}$ , suggesting that the powders only sintered together, without any grain growth. The other two single phase TaC samples, 56Ta:44C and 58Ta:42C had an increase in the grain size, 5.2 and 8.9  $\mu\text{m}$ , respectively. The slight increase between the starting powder and final grain sizes is attributed to both thermodynamic curvature growth [1] and the fact that the TaC powder was mixed with Ta powder. The Ta powder, while in small additions, had a larger powder size, and caused the final grain size to be larger.

In contrast, Ta<sub>2</sub>C grain sizes were 23  $\mu\text{m}$  which is in the range of initial Ta powder sizes that were binned to show the highest frequency of occurrence in the histogram of figure 2(a). From the diffusion couple, the carbon is depleted from the TaC phase which then reacts with the Ta metal precipitating the Ta<sub>2</sub>C phase. Thus, the Ta<sub>2</sub>C grain size would be controlled by the size of the sintered Ta and TaC powders. The larger standard deviation for Ta<sub>2</sub>C grains, as compared to TaC grains, may be because of the extreme differences between the TaC and Ta starting powder sizes. Based on the composition of 68Ta:32C, both TaC and Ta powders would convert to single phase Ta<sub>2</sub>C, whose grain size would be controlled by the initial powder size. The difference in starting powder sizes is believed to have contributed to the larger grain size distribution. Finally, the major axis length of the acicular grains is very similar to that of the Ta starting powder sizes. As mentioned previously, the rapid carbon depletion in TaC, as observed from the diffusion couple region [B], resulted in carbon's reaction and precipitation of Ta<sub>2</sub>C in the Ta metal, and as Ta being the largest constituent powder size, would govern the longest length of the acicular grains.

The next issue would be the formation of the phases. For each composition, the phases presented on the binary phase diagram, figure 1, formed upon the HIP process. Though this may seem obvious, the  $\zeta$ -Ta<sub>4</sub>C<sub>3</sub> phase has generated discussion if it is a metastable or a

thermodynamic equilibrium phase [11]. It has been speculated that when the temperature is too low to phase transform directly into  $Ta_2C$ , the  $\zeta$  phase can form under the compressive stresses as it epitaxially grows off of a  $Ta_xC_{1-x}$  phase [22,23]. Rudy and Harmon [24] noted that it took 400 hours at 1700 °C to decompose the  $\zeta$  phase. In this study, the 64Ta:36C specimen, which is in the dual phase region of figure 1, contained 7 vol. % TaC, 36 vol. %  $Ta_4C_3$ , and 57 vol. %  $Ta_2C$  according to XRD analysis. Nearly all of the initial starting TaC powder was consumed and converted into  $Ta_4C_3$  or  $Ta_2C$ . If one considers the  $\zeta$ - $Ta_4C_3$  phase stable, the TaC would ultimately be transformed since the overall composition lies between the  $Ta_2C$  and  $Ta_4C_3$  two phase region in figure 1. In the single composition specimens and the diffusion couple, the  $Ta_4C_3$  phase was a fine lath, figure 3 and 4, encased in the matrix phase.

Rowcliffe [21] reported that the  $Ta_2C$  and  $Ta_4C_3$  phase precipitates out of the TaC matrix through a stacking fault mechanism. Each of these phases has a parallel closed packed plane and closed packed direction orientation relationship with TaC. B1 TaC is a rock-salt structure which has face-centered-cubic (fcc) symmetry. It is commonly known that a Shockley partial dislocation of  $1/6\langle 211 \rangle$  passed on every other  $\{111\}$  fcc plane converts the structure to hcp. Since the B1 structure has two interpenetrating fcc lattices of Ta and C, the Shockley needs to be twice as long to give the correct symmetry displacement. This would result in a large energy penalty since dislocation energy scales with the burgers vector squared,  $b^2$  [25]. Consequently, Rowcliffe [21] suggested that a  $1/6\langle 211 \rangle$  Shockley is passed in opposite directions on parallel planes to generate the necessary displacement with the least energy penalty. Though this shift can give the correct fcc to hcp symmetry, Rowcliffe [21] did not discuss the compositional change necessary between TaC and  $Ta_2C$  or  $Ta_4C_3$ . To maintain the correct symmetry and composition, carbon atoms must be depleted on specific closed packed planes.

For transforming to  $Ta_2C$ , this depletion is on every other initial TaC plane, and for transforming to  $Ta_4C_3$ , this depletion is on every fourth initial TaC carbon plane. This would explain the fine lath structure of these phases, on these closed packed planes with the reported orientation relationships, when carbon is depleted from the TaC matrix. The closed packed plane lattice misfit of  $\sim 1.27\%$  for TaC and  $Ta_2C$  would place the lattice under compression which would enhance the diffusion of the carbon atoms away from these regions. The SEM images of these  $Ta_4C_3$  or  $Ta_2C$  bands, figure 4(b), suggests that they are thick; but complementary TEM, figure 9, reveals that these band are composed of densely packed plates of  $Ta_4C_3$  because of carbon loss on the  $\{111\}$  TaC planes.

Finally, how does the microstructure observed form from the constituent powder reactions and phase transformation pathways? The single phase TaC (51Ta:49C and 56Ta:44C) and  $Ta_2C$  (68Ta:32C) microstructures were equiaxed. This would be expected since no other phases are present; hence no interfacial energy contributions to driving a particular morphology. Rather the system forms grains that maximize volume while minimizing surface area. For the multiple phase microstructures, two distinct morphologies are present: (i) equiaxed grains that encase secondary phases in multiple directions or (ii) acicular grains which have secondary phases parallel to the major axis of the grain.

Consider case (i), equiaxed grains that encase multi-directional secondary phases. This microstructure is observed in 58Ta:42C and in region [B] of the diffusion couple. The matrix phase is TaC and the secondary phases are  $Ta_4C_3$  (and  $Ta_2C$ ). Based on the discussion above, it is apparent that only slight differences in shearing and carbon depletion distinguish the formation of these sub-stoichiometric phases in TaC and both phases could readily form in an 'ideal' two phase region between TaC and  $Ta_2C$ , figure 1. Their lath like structure is attributed to the

shearing mechanism, proposed by Rowcliffe [21], on the  $\{111\}$  planes. Since TaC has four variants in the  $\{111\}$  family, this would explain  $Ta_4C_3$  (or  $Ta_2C$ ) precipitation in multiple directions, i.e. precipitating on the different  $\{111\}$  planes. This was confirmed by our diffusion couple experiment. In region [B] in figure 4(b), the formation of  $Ta_2C$  and  $Ta_4C_3$  formed as carbon was depleted from TaC and diffused towards the Ta-rich side of the couple. The TEM micrographs of figure 9 confirmed the fine nature of these secondary phase laths on these different  $\{111\}$  planes [20].

Case (ii), an acicular grain with all the secondary phase parallel and along the major axis of the acicular grain, seen in 60Ta:40C, 64Ta:36C and region [D], is more complex. As carbon depletes TaC, it diffuses towards the Ta metal powder. Figure 1's phase diagram reveals little to no carbon solubility in tantalum. Consequently, the carbon and tantalum must react and nucleate the first available phase,  $Ta_2C$ . This was confirmed by figure 8(c), which shows small  $Ta_2C$  grains, e.g. initial nucleation sites, on the grain boundaries of the larger Ta grains. In addition, these  $Ta_2C$  grains were only found to form at the grain boundaries of the Ta grains and grain boundaries would be fast-track pathways for carbon diffusion and ideal heterogeneous nucleation sites. As these  $Ta_2C$  grains grew, they consumed the Ta grains around them which resulted in a reduction of the Ta grain size, figure 8(a). Rodriguez [26] reported that the diffusion rate of carbon in tantalum metal is three orders of magnitude higher than that in the TaC and  $Ta_2C$ . This difference in diffusion rates allowed the carbon to quickly deplete out of the TaC material and react with the constituent tantalum powder. The diffusion couple effectively shows the process of transformation of Ta into  $Ta_2C$  because of the carbon gradient.

Now that the Ta metal has been converted to  $Ta_2C$ , it reacts with the TaC (encasing  $Ta_2C$  or  $Ta_4C_3$  laths) grains, figure 6. Since the TaC grains still have a higher concentration of carbon

than  $Ta_2C$ , a carbon gradient exists. As the  $Ta_2C$  grains continue to consume more carbon, the precipitation of TaC results as the two phases, TaC and  $Ta_2C$ , grains compositionally equilibrate. Unlike fcc symmetry, which has multiple closed packed  $\{111\}$  planes, the  $Ta_2C$ , because of its hcp symmetry, has only one variant of closed packed planes,  $\{0001\}$ , within each grain. Since the closed packed planes in the closed packed direction has the lowest interfacial energy (low misfit strain), the TaC phase only precipitates in that one direction within that one  $Ta_2C$  grain. Thus, for these grains, one series of lath orientations exists. The high aspect ratio of these acicular grains also indicated an orientation dependent growth rate, with the fastest growth parallel to the close packed planes. This leads to the grain conversion into an acicular structure whose major axis of the grain is parallel to the closed packed planes, region [D] in figure 4(c). These elongated grains are clearly apparent at the interface, where carbon content would be the highest to continue the conversion and precipitation process. This acicular morphology was not observed in any other region of the diffusion couple. For the single phase  $Ta_2C$  (68Ta:32C), the conversion was complete because no elemental Ta was observed in the XRD spectra of figure 3(a). Since no secondary phases were precipitated, the grain morphology was not altered and remained equiaxed.

Lastly, at the interface, a series of small equiaxed grains, region [C] in figure 4(c), were indexed as primarily the  $Ta_2C$  phase, figure 7. Though carbon would be the fastest diffusing species in the system and would explain the precipitation and conversion of phases far from the reaction interface, the tantalum metal would also diffuse, but over a much shorter distance, and react with TaC. These small  $Ta_2C$  grains, directly at the interface, are suspected to have formed as the tantalum reacted with the TaC powders to yield  $Ta_2C$ . This would be similar to the previous discussion of initial nucleation and grain formation observed with the smaller Ta grains

on the boundaries of the larger Ta<sub>2</sub>C grains or smaller Ta<sub>2</sub>C grains at the boundaries of the larger Ta grains, figure 8.

## 5. Conclusions

A series of XTa:(1-X)C specimens, where X = 51, 56, 58, 62, 65, and 68 at. %, were HIP processed from TaC and Ta powder mixtures to span the range from phase ranges of TaC, TaC + Ta<sub>2</sub>C (Ta<sub>4</sub>C<sub>3</sub>), and Ta<sub>2</sub>C. For the single phase compositions, the microstructure was equiaxed with the TaC grains being smaller than Ta<sub>2</sub>C. The grain size difference was speculated to be due to the initial powder sizes. For composition between ~ 40 at.% C to ~ 44 at.% C (two-phase region between Ta<sub>4</sub>C<sub>3</sub> and TaC in figure 1), the microstructure consisted of equiaxed TaC grains encasing fine laths of Ta<sub>4</sub>C<sub>3</sub> precipitated on multiple TaC {111} planes within each grain. This resulted in hatch-work pattern morphology. For compositions between ~ 34 at.% C to ~ 40 at.% C, the two phase mixture consisted of acicular grains with the TaC, Ta<sub>4</sub>C<sub>3</sub> and Ta<sub>2</sub>C phases having their closed packed planes and closed packed directions all aligned and parallel to the major axis of the grain. This grain morphology is formed because of the low interfacial energy between the phases, preferential growth rate parallel to the closed packed planes and the sequence of precipitation. Using a TaC/Ta diffusion couple, it was observed that carbon is depleted from the TaC phase and reacts with the Ta to form Ta<sub>2</sub>C. Since *hcp* Ta<sub>2</sub>C has only one closed packed plane orientation, {0001}, per grain, the subsequent precipitation of TaC within these grains results in all the phases being parallel laths which drives the change in grain shape. These results clearly indicate that small variations in carbon content can have a dramatic effect on microstructure morphology and phase content. The sequence of precipitation of the initial matrix phase, either TaC or Ta<sub>2</sub>C, controls the overall grain morphology because of the preferred orientation relationship of these phases with each other.

## 6. Acknowledgement:

This research has been supported by the Army Research Office under grant W911NF-08-1-0300, Dr. David Stepp program manager.

## 7. References

- [1] R. M. German, *Powder Metallurgy and Particulate Processing*. Princeton, New Jersey: Metal Powder Industries Federation, 2005.
- [2] M. Desmaison-Brut, N. Alexandre, and J. Desmaison, "Comparison of the Oxidation Behavior of Two Dense Hot Isostatically Pressed Tantalum carbide (TaC and Ta<sub>2</sub>C) Materials," *Journal of the European Ceramic Society*, **17**(1997) 1326-1334
- [3] E K Storms, "The Tantalum-Tantalum Carbide System," in *The Refractory Carbides.*: Academic Press, 1967.
- [4] C. R. Wang, J. M. Yang, and W. Hoffman, "Thermal stability of refractory carbide/boride composites," *Mater. Chem. Phys.*, **74**(3)(2002) 272-281
- [5] K. Upadhyay, J. M. Yang, and W. P. Hoffman, "Materials for Ultrahigh Temperature Structural Applications," *Am. Ceram. Soc. Bull.*, **76**(12)(1997) 51-56
- [6] K. Balani, G. Gonzalez, A. Agarwal, R. Hickman, and J. S. O'Dell, "Synthesis, Microstructural Characterization, and Mechanical Property Evaluation of Vacuum Plasma Sprayed Tantalum Carbide," *J. Am. Ceram. Soc.*, **89**(4)(2006) 1419-1425
- [7] G. Santoro and H. B. Probst, "An Explanation of Microstructures in the Tantalum-Carbon System," in *Adv. X-Ray Anal.*, **7**, 1963, pp. 126-135.
- [8] F. Lissner and T. Schleid, "Redetermination of the Crystal Structure of di-Tantalum monocarbide, Ta<sub>2</sub>C," *Z. Kristallogr. NCS*, **216**(6)(2001) 329
- [9] A. L. Bowman, "The Variation of Lattice Parameter with Carbon Content of Tantalum Carbide," *J. Phys. Chem. A* , **65**(9)(1961) 1596-1598
- [10] O. M. Barabash and Y. N. Koval, *A Handbook on the Structure and Properties of Metals and Alloys*. Kiev: Naukova Dumka, 1986.
- [11] A. I. Gusev, A. S. Kurlov, and V. N. Lipatnikov, "Atomic and Vacancy ordering in carbide z-Ta<sub>4</sub>C<sub>3-x</sub> and Phase equilibria in the Ta-C system," *J. Solid State Chem.*, **180**(2007) 3234-

- [12] K. Yvon and E. Parthe, "On the Crystal Chemistry of the Close Packed Transition Metal Carbides. I. The Crystal Structure of the z-V, Nb, and Ta Carbides," *Acta Crystallogra.*, **26**(1970) 149-153
- [13] D. J. Rowcliffe and G. E. Hollox, "Plastic Flow and Fracture of Tantalum Carbide and Hafnium Carbide at Low Temperatures," *J. Mater. Sci.*, **6**(1971) 1261-1269
- [14] R. W. G. Wyckoff, *Crystal Structures*, 2nd ed. New York: Interscience Publishers, 1963.
- [15] J. M. Cowley, *Diffraction Physics*, 3rd ed. Amsterdam, The Netherlands: Elsevier Science B. V., 1995.
- [16] D. B. Williams and C. B. Carter, *Transmission electron microscopy: a textbook for materials science*. New York, N.Y.: Springer Science, 1996.
- [17] L. A. Giannuzzi, "Reducing FIB Damage Using Low Energy Ions," *Journal of Microscopy and Microanalysis*, **12**(2)(2006) 1260-1261
- [18] L. A. Giannuzzi, R. Geurts, and J. Ringnalda, "2 keV Ga<sup>+</sup> FIB Milling for Reducing Amorphous Damage in Silicon," *Journal of Microscopy and Microanalysis*, **11**(2)(2005) 828-829
- [19] C.Y. Kuo, J.D. Frost, J.S. Lai, and L.B. Wang, "Three-Dimensional Image Analysis of Aggregate Particles from Orthogonal Projections," *Transp. Res. Rec.*, **1526**(1997) 98-103
- [20] R. A. Morris, D. Butts, and G. Thompson, "TaXC<sub>1-X</sub> Phases and Microstructures Processed by Vacuum Plasma Spraying," *J. Am. Ceram. Soc.*, **In press**(2010)
- [21] D. J. Rowcliffe, "Structure of Non-Stoichiometric TaC," *Mater. Sci. Eng.*, **18**(1975) 231-238
- [22] W. F. Brizes and J. M. Tobin, "Isolation of the Zeta Phase in the System Tantalum Carbide," *Journal of the American Ceramic Society*, **50**(2)(1967) 115-116
- [23] I. Zaplatynsky, "Observations of the zeta phase in the system Ta-C," *J. Am. Ceram. Soc.*, **49**(2)(1966) 109-110
- [24] E. Rudy and D P Harmon, Air force Materials Laboratory Research and Technology Division, Air Force Command, Wright-patterson A.F.B., Ohio, AFML-TR-65-2, Part I, Volume V, 1965.

[25] D. Hull and D.J. Bacon, *Introduction to Dislocations*, 4th ed. Woburn, Ma: Butterworth-Heinemann, 2001.

[26] P. J. Rodriguez, "Characterization and Refinement of Carbide Coating Formation Rates and Dissolution Kinetics in the Ta-C System," The University of New Mexico, Albuquerque, New Mexico, Thesis 1996.

## CHAPTER 3

### TANTALUM CARBIDE PHASES AND MICROSTRUCTURES PROCESSED BY VACUUM PLASMA SPRAYING <sup>2</sup>

#### Abstract

A series of tantalum carbide compounds have been fabricated by vacuum plasma spraying from constituent TaC powders. By manipulating the process parameters, the carbon content was altered and either equiaxed or acicular grains in the microstructure could be produced. The equiaxed grains contained a TaC matrix that encased fine laths of Ta<sub>4</sub>C<sub>3</sub>; in contrast, the acicular grains contained layered TaC, Ta<sub>4</sub>C<sub>3</sub>, and Ta<sub>2</sub>C along the major-axis of the grains. The phases of the compounds have been determined by complimentary X-ray diffraction and electron diffraction techniques. Focus ion beam serial sectioning and transmission electron microscopy tilt series tomography were performed to generate three dimensional reconstructions of the microstructure morphologies.

---

<sup>2</sup> A manuscript has been prepared for the work in this chapter for the publication in the Journal of American Ceramics Society as : R.A. Morris, D. Butts, L. Matson, G.B. Thompson, "Ta<sub>x</sub>C<sub>1-x</sub> Phases and Microstructures Processed by Vacuum Plasma Spraying."

## 1. Introduction

The TaC phase has a melting temperature near 4000 °C, which is one of the highest melting temperature materials known [1]. Consequently, tantalum carbide has been proposed for thermal heat protection, automotive wear resistant liners, and other types of thermo-mechanical loading applications [2-4]. The TaC phase is a B1 compound with carbon atoms occupying the octahedral interstitial sites in a tantalum face-centered-cubic lattice [1,5]. For carbon deficient phases, a Ta<sub>2</sub>C phase can precipitate at temperatures below 3500 °C [6,7], as seen in the phase diagram by Barabash *et al.* [8] in figure 1. This phase consists of hexagonal metal layers separated between either an  $\alpha$ -ordered or  $\beta$ -disordered carbon sublattice. The Ta<sub>2</sub>C allotropic phase transformation between  $\alpha$  (CdI antitype structure) to  $\beta$  (*L'*3 structure) is near 2000 °C [1,5]. In addition, a  $\zeta$ -Ta<sub>4</sub>C<sub>3</sub> phase, which is rhombohedral with the space group R3m, can form at 2500 °C [9,10] The thermodynamic stability of the  $\zeta$ -Ta<sub>4</sub>C<sub>3</sub> phase is still under discussion [9]. The ultra-high melting temperature of TaC and the ability to precipitate similar high melting temperature species offers several microstructure engineering opportunities to tailor this system for extreme-high temperature thermo-mechanical applications [11].

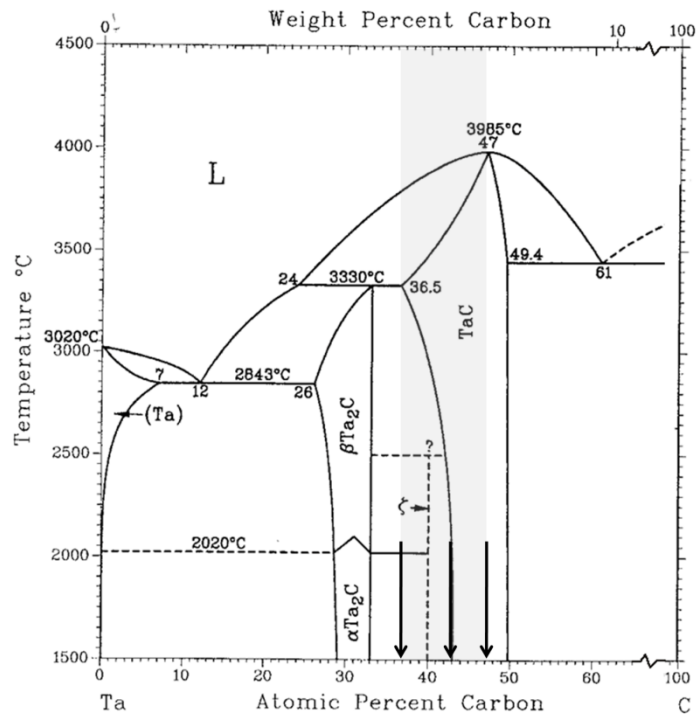


**Figure 1:** Ta-C binary phase diagram showing a highlighted region of the Ta/C content obtained for each specimen investigated, as determined by EDS. Phase diagram from work by Barabash et al. [8]

One of the consequences of TaC's high melting temperature is the limited number of processing methods capable of fabricating near full density tantalum carbides. In general, hot-isostatic pressing (HIP) of powders, spark-sintered processing, arc melting, or vacuum plasma spraying (VPS) are the viable means to fabricate tantalum carbides [12]. In the VPS method, the tantalum carbide powders are fed into a plasma gun where they are melted and exit the gun at high velocities (e.g. Mach 1). The molten particles are deposited onto a substrate where upon it solidifies and a tantalum carbide product is built up through continuous deposition. As with any manufacturing process, changing the processing parameters for VPS can result in a variation in the final microstructure of the tantalum carbide. In particular, the time the powder stays in the plasma plume can affect the final microstructure and chemistry [13] and offer means to engineer

the final sprayed product. In particular to TaC, the large difference in vapor pressure between tantalum and carbon [14] can result in a preferential loss of carbon during processing which changes the final product chemistry and phase content. In the present research, a series of tantalum carbide specimens have been vacuum plasma sprayed and post-processed by sintering and hot isostatic pressing (HIP) to reveal different microstructures dependent upon the retained carbon content. The microstructure morphologies are explained by the phase content and sequence of precipitation.

## 2. Experimental Procedure

Three XTa:(1-X)C specimens, where X= 53, 55, and 63 at. %, were fabricated by the VPS process. These compositions, hence listed in atomic percent, are shown on the binary Ta-C phase diagram in figure 1 and represent the final composition post-processing. The spraying chamber was evacuated to 13 Pa using mechanical pumps and backfilled with argon to a pressure of 27 kPa. An argon-hydrogen mixture having a ratio of 70:1 served as the carrier gas for the TaC feedstock powder that was injected into the tungsten cathode plasma gun. The plasma gun employed argon as the primary plasma gas and hydrogen as the secondary. The molten  $Ta_xC_{1-x}$  was deposited onto a rotating graphite mandrel. The carbon loss was controlled by the resonance time the powder spent in the plasma plume. Post-VPS fabrication, the graphite mandrel was mechanically ground away whereupon the XTa:(1-X)C specimens were sintered in a graphite furnace under a vacuum environment near  $0.5 T_m$ , where  $T_m$  is the melting temperature, to reduce the porosity inherent in the VPS fabrication method [4]. Post-sintering, the XTa:(1-X)C specimens were approximately 95+% dense. To further reduce porosity and homogenize the microstructures, the specimens were HIP'ed at 200 MPa in an argon atmosphere near  $0.5 T_m$ . The post-HIP densities were >98 % dense. The density measurements were done by a water

immersion displacement technique [15] and compared to the theoretical density of 14.5 g/cc for TaC and 14.8 g/cc for Ta<sub>2</sub>C [16]. Since the volume fraction of each phase was estimated, the densities given are approximate.

Post-manufacturing, the XTa:(1-X)C specimens were sectioned via a diamond saw. The ‘interior’ portions (not free surfaces or edges) of the XTa:(1-X)C specimens were examined for the subsequent analysis. The specimens were mounted in cross-section, mechanically ground and polished to 3 micron diamond abrasive paste and then Vibromet® polished for 24 hours in aqueous 0.05 micron silica slurry. The microstructures were imaged using either secondary electron or ion contrast imaging in a FEI Quanta 3D dual beam focus ion beam (FIB) - scanning electron microscope (SEM) operated at 30 keV. Electron backscatter diffraction (EBDS) patterns, used for phase identification, were collected on the EDAX-TSL platform attached to the FEI Quanta 3D microscope. Finally, the FEI Quanta 3D microscope’s ion beam was used to perform a series of serial sectioning and imaging steps to reveal the depth dependent change in microstructure.

For serial sectioning, the surfaces of the specimens were polished to a grit of 0.5 μm silica after which they were adhered onto a SEM aluminum stub. A 10 μm x 10 μm isolated pillar was cut out of the edge of each specimen using a diamond saw. This pillar provided the volume from which successive mill cuts would be taken. By isolating the pillar from the bulk of the sample, the ‘gaps’ between the pillars allowed easy removal of material without re-deposition back onto the pillar surface. A protective platinum cap, ~5 μm thick, was *in situ* deposited onto the surface and long axis direction of the pillar using an organometallic precursor gas injection system attached to the Quanta 3D. This capping layer reduced the amount of ‘streaking or curtaining’ across the specimen surface during each cut caused by the ion beam. The pillars were

FIB-milled at 1 nA and 30 keV at steps sizes of 100 nm using an automated scripting program. After each mill, the revealed surface was rotated, ion contrast imaged and subsequently rotated back such that the ion beam could continue the serial slicing. Ion contrast imaging was found to easily distinguish the microstructure's grains and phases over more traditional SEM imaging techniques. Ion surface damage to the specimen was not noted during the time required to collect the ion contrast image. The VSG Avizo® Fire software platform was used to compile and reconstruct the sequential serial images to generate the three-dimensional (3D) rendering.

X-ray diffraction for phase identification and estimated volume fraction determination was done using a Bruker Discovery D8 General Area Diffraction Detector System with Cu-K $\alpha$  radiation at 45 keV and 40 mA as the source. The TaC, Ta<sub>2</sub>C, and  $\zeta$ -Ta<sub>4</sub>C<sub>3</sub> phases were identified using data from Wyckoff [17], Lissner [6], and Gusev *et al.* [9] sources, respectively. The phase content is tabulated in Table 1 and was estimated by the integrated intensity of the theoretically most intense peak for each phase, which are the {111}<sub>TaC</sub>, {107}<sub>Ta<sub>4</sub>C<sub>3</sub></sub>, and {1011}<sub>Ta<sub>2</sub>C</sub> reflections. [17,9,6] reflections, divided by the sum of all maximum peak intensities [18].

**Table 1:** Tabulated phase amounts for the samples used for this investigation determined by integrated intensities of the XRD scans in figure 2(d) and 4(a).

Samples/Phase (Volume %)	TaC	Ta <sub>4</sub> C <sub>3</sub>	Ta <sub>2</sub> C
53Ta:47C -As sprayed	67.7	~0	32.3
53Ta:47C-Sintered	89.4	7.8	2.7
53Ta:47C-HIP'ed	100	~0	~0
55Ta:45C-HIP'ed	95.9	4.1	~0
63Ta:37C-HIP'ed	69.2	25.8	5.0

SEM-energy dispersive spectroscopy (EDS), collected on an EDAX Apollo XV silicon drift detector, was used to determine the approximate Ta and C composition of each specimen using an electron beam setting of 10 keV and 3.3 nA. A standard 51Ta:49C was used for calibrating the EDS instrument. The large difference in atomic number between Ta and C can result in the preferential absorption of carbon x-rays by tantalum. To provide a complimentary comparison to the EDS composition measurements, a lever rule approximation using the determined volume fractions of each phase was performed and had good agreement to the EDS results. These results are tabulated in Table 2.

**Table 2:** Tabulated carbon content data for the samples used for this investigation determined using both the lever rule and EDS.

Samples/Phase (at. %)	Lever rule		EDS		
	Ta	C	Ta	C	Std. Dev. (%)
53Ta:47CAs sprayed	60	40	54	46	0.98
53Ta:47C Sintered	58	42	54	46	0.30
53Ta:47CHIP'ed	50	50	53	47	0.41
55Ta:45C HIP'ed	57	43	55	45	0.86
63Ta:37C HIP'ed	61	39	63	37	1.10

Transmission electron microscopy (TEM) was performed using an FEI F20 Tecnai TEM operated at 200 keV. Correlated bright field and dark field imaging with electron diffraction was used for phase and microstructure identification. Complimentary atomic, or Z-, contrast imaging using a High Angle Annular Dark Field (HAADF) detector was done in a scanning TEM (STEM) mode. The HAADF collects scattered electrons that are relatively insensitive to crystallographic dependent (Bragg) scattering; therefore, the contrast observed is chemically dependent with higher atomic number elements being brighter [19]. By tilting the TEM foil and

collecting a series of STEM-HAADF images, a reconstructed tomography image of the phases has been done [20]. An advantage of these three-dimensional reconstructions as compared to the serial sectioning described above is its ability to recover the tens of nanometer fine scale size precipitate features.

### 3. Results

All three specimens underwent the same three stages of processing: VPS, sinter and HIP. The phase and microstructure evolution at each stage of processing is shown for the 53Ta:47C specimen in figure 2. The micrographs in figure 2(a)-(c) clearly reveal an evolution of grain size and shape with each processing step and the XRD spectra, figure 2(d), reveals a changing phase content which is quantified in the histogram of figure 2(e). The as-sprayed VPS microstructure, figure 2(a), shows a bimodal distribution of grain sizes with one group being micron-plus in size and the other being sub-micron in size. Using EBSD, it was determined that the larger grains were composed of the TaC phase while the smaller grains were Ta<sub>2</sub>C, figure 3. These phases are consistent with the phases identified in the XRD spectra. The topography of this specimen, figure 3(a), also revealed a ‘step ledge’ between the larger grains and the smaller grains. This is because of the hardness difference between the two phases. During polishing, the Ta<sub>2</sub>C was more readily removed while the harder TaC phase remained. This topography modulation can be a readily easy way to identify the phases.

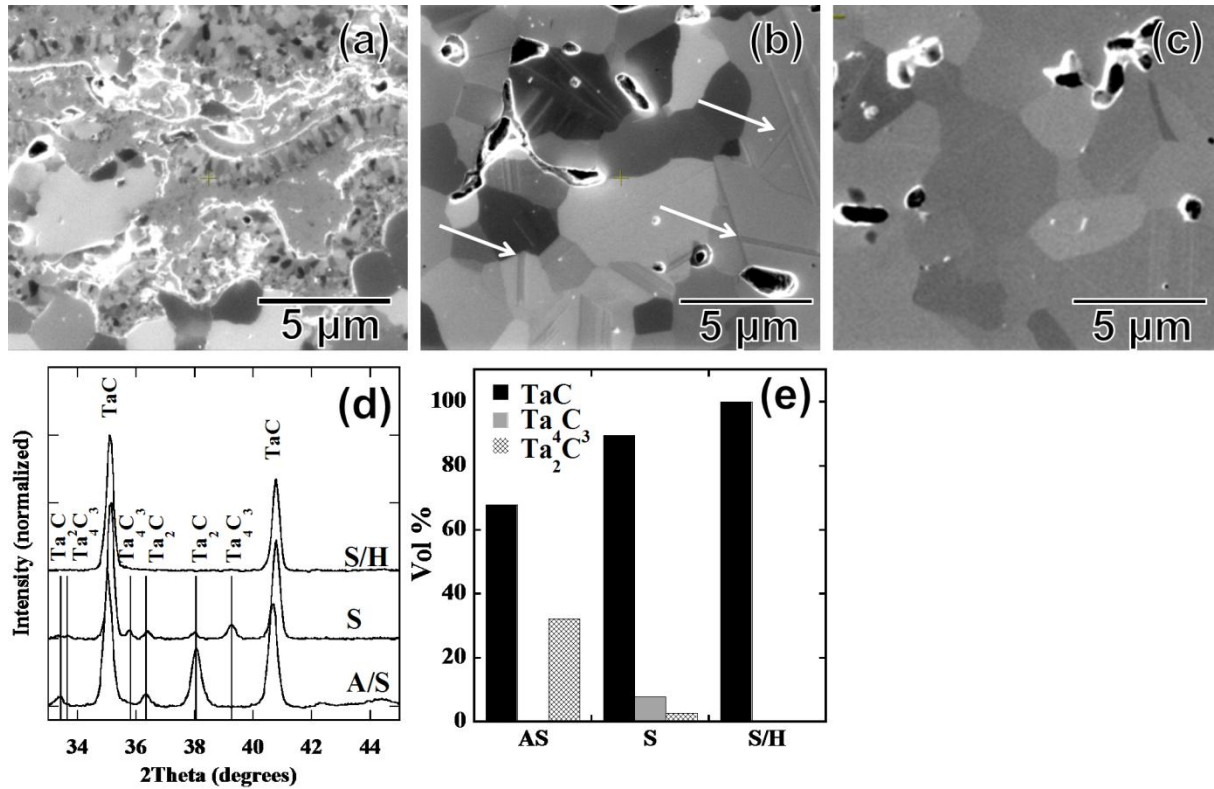


**Figure 2 :** Images and XRD data from Ta<sub>53</sub>C<sub>47</sub>. (a) FIB image of the as-sprayed Ta<sub>53</sub>C<sub>47</sub> showing a heterogeneous variation in grain size. (b) FIB image of the sintered condition showing the secondary phases within the TaC grains, indicated by white arrows. (c) FIB image of HIP'ed condition showing equiaxed TaC grains. (d) XRD of Ta<sub>53</sub>C<sub>47</sub> at as-sprayed (AS), sintered (S), and HIP'ed (S/H) conditions. (e) A bar plot of phase content determined from XRD showing a decreasing secondary phase with sintering and HIP'ing.

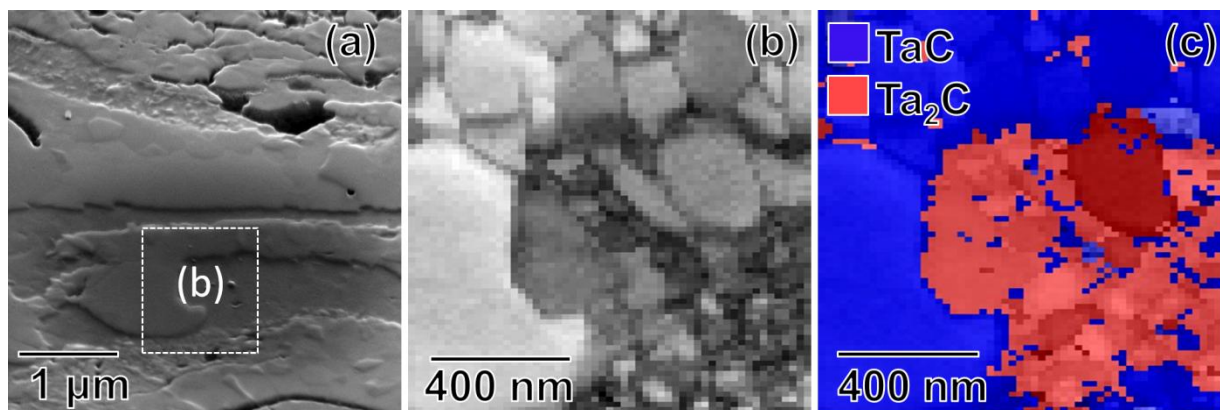


**Figure 3:** SEM and EBSD micrographs of as-sprayed specimen. (a) SEM image of the as-sprayed version of Ta<sub>53</sub>C<sub>47</sub> tilted to show the variation in topography in the surface. (b) EBSD Image quality map of region highlighted in (a). (c) EBSD phase map of region highlighted in (a) showing separated regions of TaC and Ta<sub>2</sub>C.

The sintered Ta<sub>53</sub>C<sub>47</sub> specimen, figure 2(b), showed a significant increase and equalization of grain sizes compared to the as-sprayed specimen, figure 2(a). The sintering allowed the larger grains to coarsen. The XRD spectra of the sintered specimen revealed the presence of both the Ta<sub>2</sub>C and Ta<sub>4</sub>C<sub>3</sub> phases along with TaC. As will be discussed later, the lath structures encased within the grains in the micrograph of figure 2(b) are these tantalum-rich phases.

The HIP'ed version of 53Ta:47C showed similar grain sizes and morphology to that of the sintered version. XRD spectrum, figure 2(d), was indexed to TaC. The SEM micrograph of figure 2(c) did show some very faint lath structures, but the volume fraction of this phase was insufficient to diffract adequate XRD intensities for either of the previous Ta<sub>2</sub>C and Ta<sub>4</sub>C<sub>3</sub> phases to be clearly identified.

The XRD spectra for all three post-processed specimens are shown in figure 4(a). As the specimens become carbon depleted, the precipitate phases of Ta<sub>2</sub>C and Ta<sub>4</sub>C<sub>3</sub> become more apparent with the TaC phase. The microstructures of the tantalum carbides, figure 4(b)-(d), also changed with phase content. The volume fraction of the phases in each specimen is tabulated in Table 2. For the 53Ta:47C specimen, the grains are equiaxed and, based on the XRD spectra, is TaC. The 55Ta:45C specimen retains the equiaxed grains but clearly has a multi-directional lath structure encased within the grains. From the XRD spectra, figure 4(a), and the selected area electron diffraction (SAED) pattern in figure 5, the bands have been identified to be the Ta<sub>4</sub>C<sub>3</sub> phase. The Ta<sub>4</sub>C<sub>3</sub> phase within the TaC grain has been found to have the following orientation relationship:  $\{111\}_{\text{TaC}} // \{0001\}_{\text{Ta}_4\text{C}_3}$  and  $\langle 110 \rangle_{\text{TaC}} // \langle 1010 \rangle_{\text{Ta}_4\text{C}_3}$ . The STEM-HAADF tomography tilt series reconstruction, figure 5(d), shows the cross-hatched pattern in the grain with each parallel Ta<sub>4</sub>C<sub>3</sub> phase having the same color distinction.

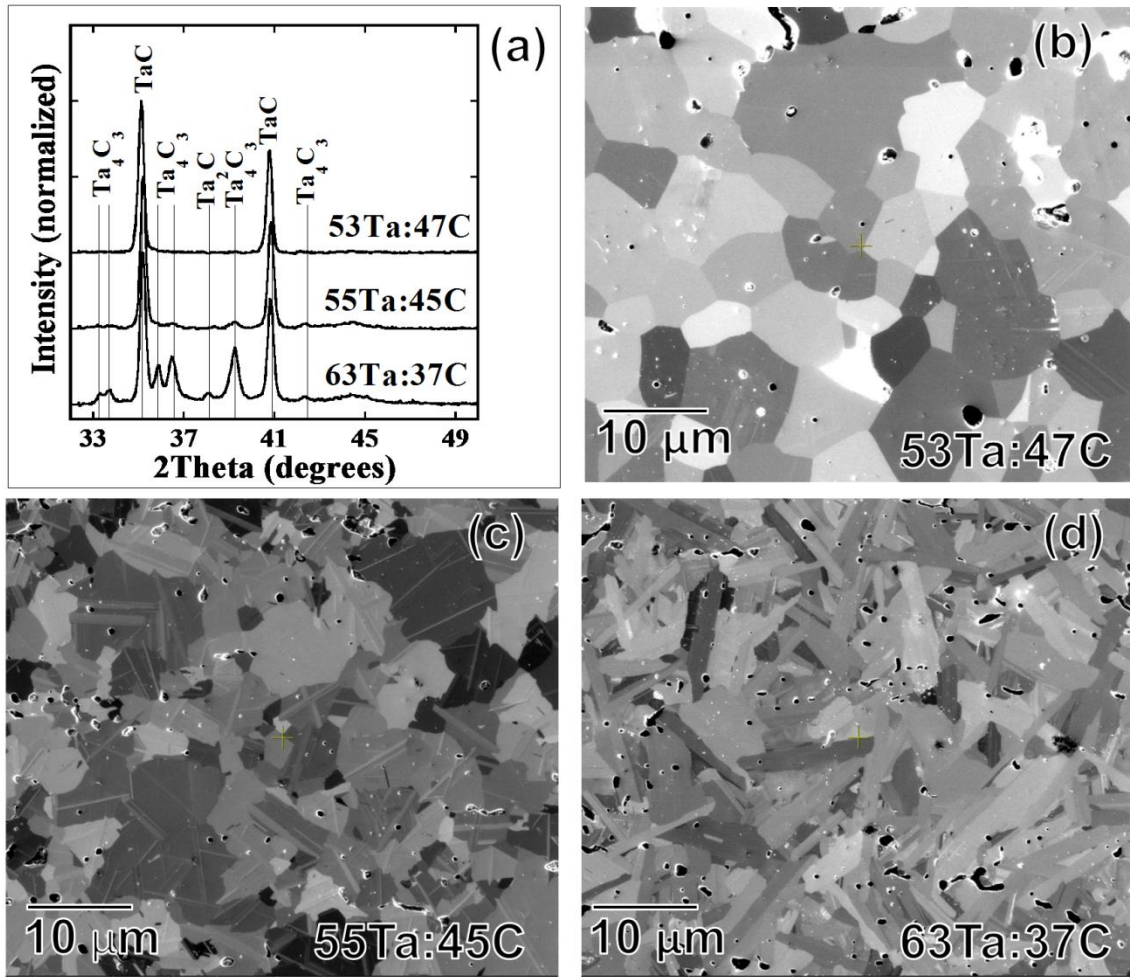


**Figure 4:** XRD and FIB micrographs of the VPS specimens. **(a)** XRD of 53Ta:47C, 55Ta:45C, and 63Ta:37C. Note the change in relative peak heights of the Ta<sub>2</sub>C and Ta<sub>4</sub>C<sub>3</sub> phases. **(b)** FIB image of 53Ta:47C showing single phase equiaxed TaC grains. **(c)** FIB image of 55Ta:45C showing secondary laths encased within TaC equiaxed TaC grains. **(d)** FIB image of 63Ta:37C showing an acicular grain structure of TaC, Ta<sub>2</sub>C, and Ta<sub>4</sub>C<sub>3</sub> phases.

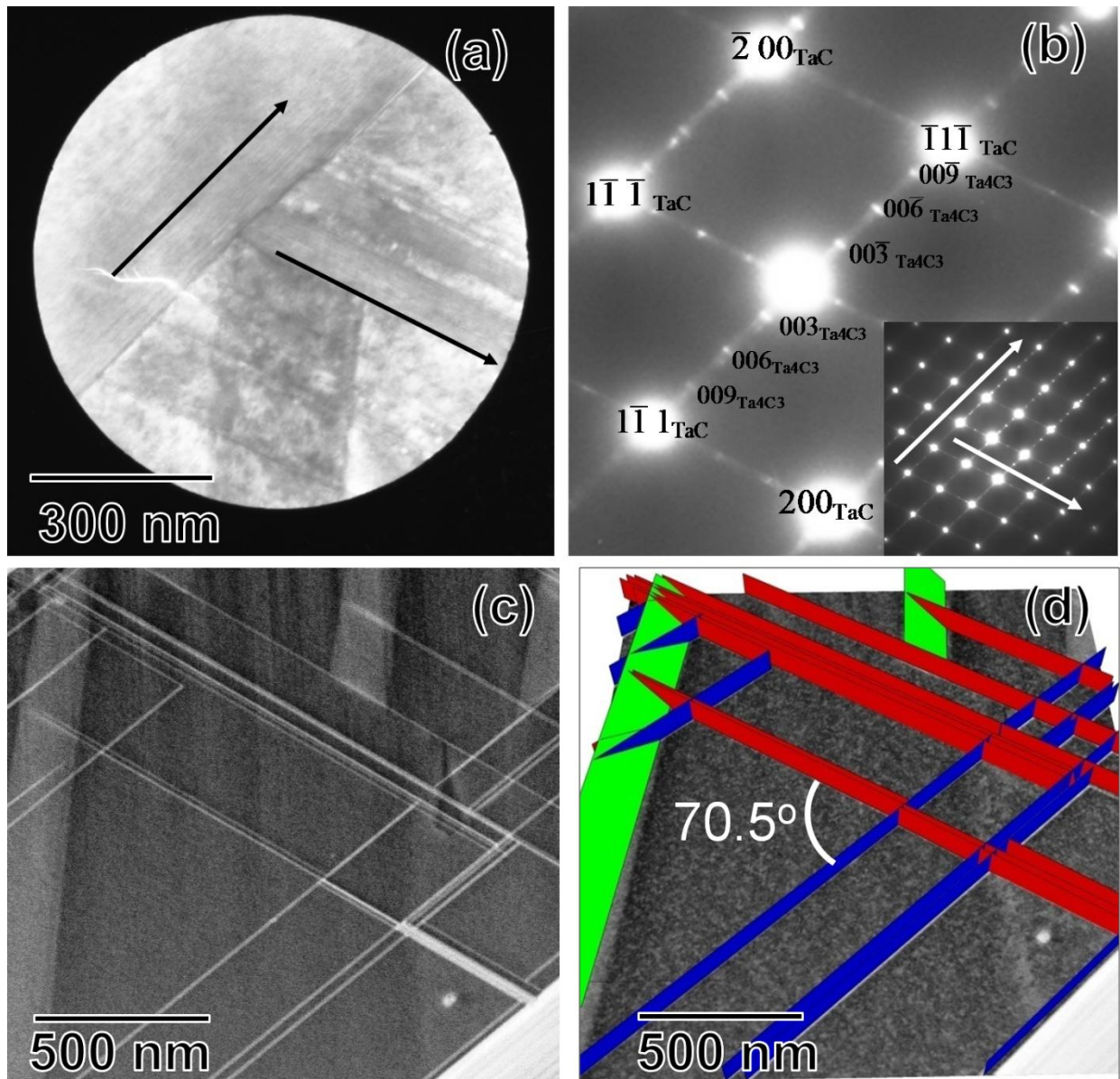


**Figure 5:** TEM data of 55Ta:45C specimen (a) Selected area BF-TEM of TaC grain with Ta<sub>4</sub>C<sub>3</sub> laths tilted to look down  $\langle 110 \rangle_{\text{TaC}}$  (b) Selected area electron diffraction of (a). (c) STEM-HAADF image of intersecting Ta<sub>4</sub>C<sub>3</sub> laths. (d) 3D reconstruction of HAADF tomography series showing Ta<sub>4</sub>C<sub>3</sub> laths forming on different  $\{111\}$  planes, indicated by different colored bands.

Since the TEM foils can only capture a very finite material volume, serial sectioning using the FIB-SEM provided a 3D global characterization of an entire lath structure within a single grain of 55Ta:45C. Two gray scale colors are provided to identify two separate laths in the

single grain shown in figure 6. In one case, the lath spans the entire grain where as in the second case, the lath arrest in the middle of the grain. A closer observation of the micrograph in figure 4(c) reveals that not all the laths span the grains.

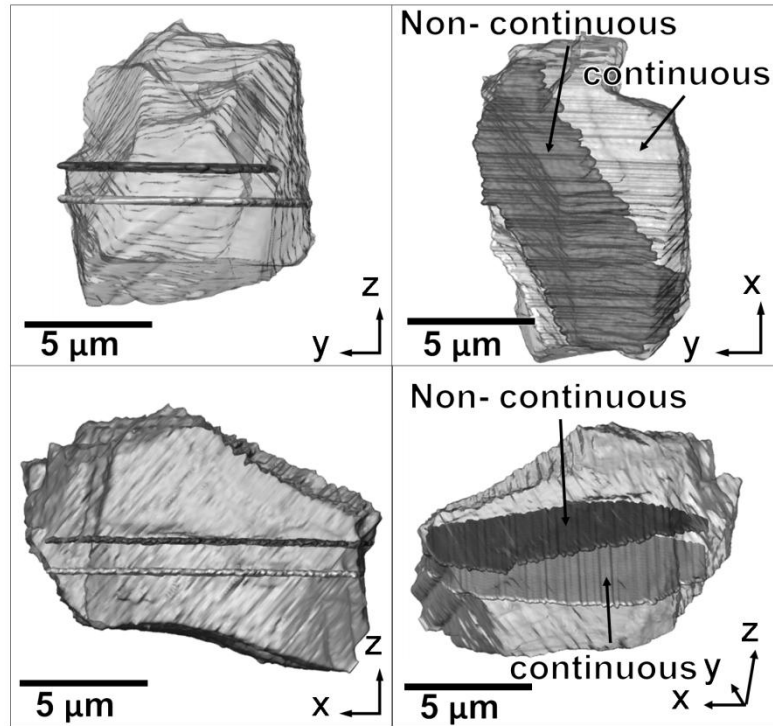


**Figure 6:** Different viewing direction of a 3D reconstruction of a grain in 55Ta:45C. The grain contained two types of laths, one continuous though the entire grain, and one that terminated in the middle of the grain, labeled non-continuous.

The 63Ta:C37 specimen had the highest volume fraction of secondary phases, tabulated in Table 1. Higher magnification SEM and TEM imaging revealed that the acicular grains were comprised of a fine lath structure of multiple phases along the major-axis of the grain, figure 7. This layered lath stacking is clearly evident in the magnified STEM-HAADF image of figure 7(c) taken from the region shown in figure 7(b). SAED, figure 7(d), revealed the phases TaC, Ta<sub>2</sub>C, and Ta<sub>4</sub>C<sub>3</sub> have the following orientation relationship:  $\{111\}_{\text{TaC}} // \{0001\}_{\text{Ta}_4\text{C}_3} // \{0001\}_{\text{Ta}_2\text{C}}$  and  $\langle 110 \rangle_{\text{TaC}} // \langle 10\bar{1}0 \rangle_{\text{Ta}_4\text{C}_3} // \langle 10\bar{1}0 \rangle_{\text{Ta}_2\text{C}}$ . [21]

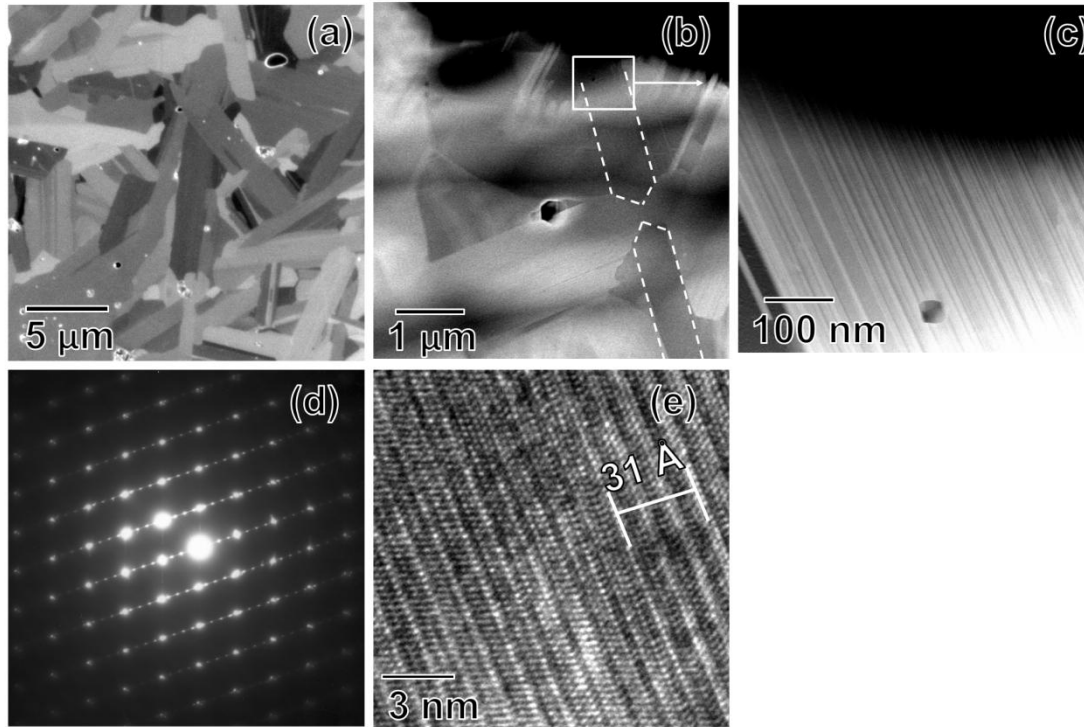


**Figure 7:** FIB and TEM micrographs of 63Ta:37C specimen. (a) FIB image of  $Ta_{63}C_{37}$  with acicular shaped grains containing secondary phases running the long axis of the grains. (b) STEM-HAADF image of  $Ta_{63}C_{37}$ ; the highlighted grain shows acicular nature of grains and how grains may intersect and divide each other. (c) STEM-HAADF of highlighted region in (b) showing multiple closely spaced secondary phase laths. (d) SAED of grain in (b) tilted down  $\langle 110 \rangle_{TaC}$ . (e) Lattice fringes of highlighted grain in (b) with length bar indicating lattice spacing of  $Ta_4C_3$  c-axis.

Based on the contrast mechanism of HAADF, the brighter bands in figure 7(c)'s micrograph are the tantalum rich phases. A TEM image viewed from the  $\langle 110 \rangle_{TaC}$  direction shows the lattice fringes of these laths, figure 7(e), whose banded structure spacing matched the length of a unit cell of  $Ta_4C_3$ . The serial sectioned reconstruction, figure 8, revealed that the laths, the dark gray feature, spanned the entire interior of the grain. A careful review of the micrographs shown in figure 7 also confirms that these secondary phases appear to span entire major-axis direction of the TaC acicular grains.

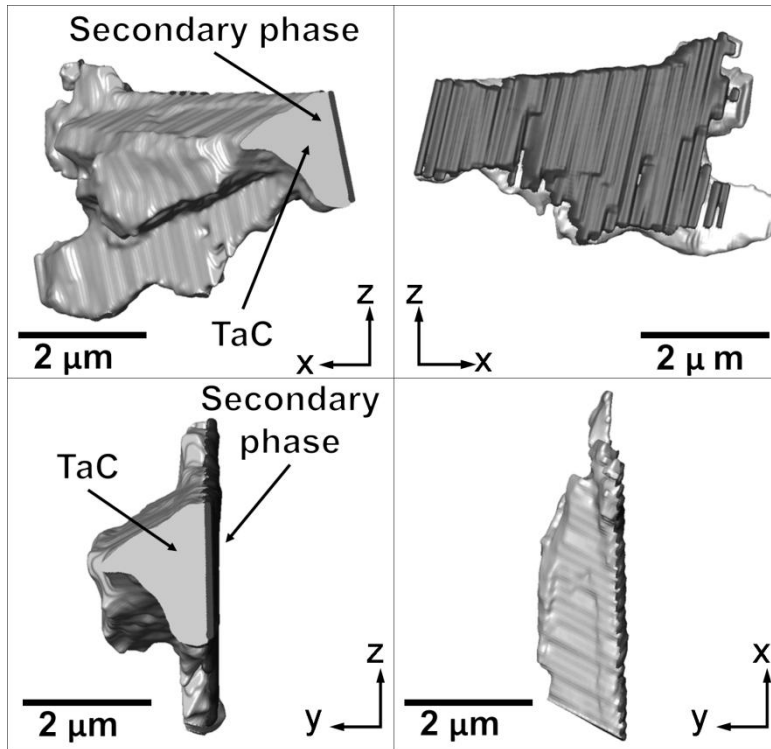


**Figure 8:** Different viewing direction of a 3D reconstruction of a grain in  $Ta_{63}C_{37}$ . The grain contained a thickened secondary phase that spanned the entire grain. The ribbed surface of the grain is an artifact of the 3D reconstruction.

#### 4. Discussion

The as-sprayed 53Ta:47C specimen contained both TaC and  $Ta_2C$  phases, with the  $Ta_2C$  grains being significantly smaller. The presence of  $Ta_2C$  could be a result of the rapid solidification that occurs during the VPS process. Since the  $Ta_2C$  phase content diminished with the subsequent sintering and HIP processing, this phase may have formed by some local loss of carbon during the rapid solidification and was homogenized in the subsequent steps. Interestingly, no  $Ta_4C_3$  phase was indexed in the as-sprayed condition, which is the suspected metastable phase in this system [9].

As a consequence of the lower melting temperature of  $Ta_2C$  ( $\approx 3330$  °C) as compared to TaC ( $\approx 3985$  °C), a grain size distribution developed in the as-sprayed condition. The  $Ta_2C$  will

precipitate out at lower temperatures; consequently, these grains will have relatively lower mobility (growth) because of the reduced temperature as compared to initial TaC phases. In addition, these composition will be further under-cooled, and at a lower temperature, where the thermodynamic nucleation driving force will be high. This will result in numerous nucleation events that resulted in a finer grain size. We recently have provided a generic interface tracking microstructural model for Hf additions to TaC [22]. The increasing Hf content drove the system into a larger liquid phase field or, alternatively, a lower melting temperature. The results revealed that a decrease in the melting temperature resulted in a greater concentration of grains, which were on average smaller. The lack of the Ta<sub>4</sub>C<sub>3</sub>, along with the Ta<sub>2</sub>C, in the as-sprayed specimen could be a result of the non-equilibrium processing of the vacuum plasma spraying or a low volume fraction that is below the detection limit of the XRD analysis.

The layered morphology of the as-sprayed condition is typical of the VPS process [4] and results from the continual build up of material with each successive plasma torch pass. As would be expected, the greatest amount of porosity, which was elongated and continuous, was observed between each build-up layer, figure 2(a).

Upon sintering, a small presence of Ta<sub>4</sub>C<sub>3</sub> formed in the 53Ta:47C specimen. It is noted that the specimens were sintered in a graphite filament furnace which could have provided a low carbon content environment. The loss of the Ta<sub>2</sub>C and Ta<sub>4</sub>C<sub>3</sub>, figure 4(a), continued with the HIP. The HIP specimens also were processed in an environment which used carbon heating elements. The continual loss of the Ta<sub>2</sub>C and Ta<sub>4</sub>C<sub>3</sub> phases in the subsequent VPS processing steps suggests the transformation may not be solely driven by the subsequent post processing, but rather the consumption of the smaller Ta<sub>2</sub>C grains by the larger TaC grains because of the Gibbs-Thomson effect [23]. The TaC phase has a range of carbon solubility while still retaining

the B1 structure, as seen in the phase diagram in figure 1. The consumption of the more tantalum-rich phase would result in a sub-stoichiometric shift in TaC's carbon content while still retaining the TaC symmetry. The TaC lattice parameter is sensitive to carbon content. A clear XRD shift between the as-sprayed and sintered specimen does exist in figure 2(d). This as-sprayed to sintered XRD shift is in the direction of a smaller d-spacing, which would correspond to a sub-stoichiometric TaC carbon content. The sintered equiaxed TaC grains also show laths within the grains, which are likely the Ta<sub>4</sub>C<sub>3</sub> phase, as seen in the 55Ta:45C microstructures, and represent the intermediate conversion phase between the consumed Ta<sub>2</sub>C to the substoichiometric TaC phases. Brizes [24] has reported that the growth of the carbide layers is because of carbon and not tantalum atoms diffusing. The sintering also changed the porosity, in general, to be between the grains and likely developed during the coarsening of the curvature-driven grain growth. Regardless, the sintering and HIP steps helped to homogenize the phase content and microstructure. There was negligible lattice shift in the TaC XRD peak between these two steps in figure 2(d).

A comparison of 55Ta:45C and 63Ta:37C revealed two distinct microstructures both of which contained secondary phases with TaC. The former consisted of equiaxed grains which encased laths in multiple directions within each grain where as the latter formed as acicular grains with the laths running parallel to each other along the major-axis of the acicular grain. For the 55Ta:45C specimen, SAED revealed that the laths were the Ta<sub>4</sub>C<sub>3</sub> phase with precipitation on the closed packed TaC {111} planes. Based on the orientation relationship, the Ta<sub>4</sub>C<sub>3</sub> and TaC phases have a lattice misfit of 0.64% which would be a low energy interface. Since a single TaC crystal or grain has multiple variants of {111}, the Ta<sub>4</sub>C<sub>3</sub> phase precipitated on several different {111} habit planes which yielded the multi-directional or cross-hatch pattern observed, figure 5.

The STEM-HAADF tomography tilt series reconstruction, figure 5(d), has parallel phases registered as the same color. The angle between these different color laths was  $70.5^\circ$  which is consistent with the orientation angle between such  $\{111\}$  planes with respect to each other.

Though the SEM micrograph in figure 4(c) would suggest the bands have a variety of thicknesses, TEM analysis, figure 5, revealed that these laths are actually tens of nanometers thick but have large surface areas within the grain. Thus, the ‘thick’ laths in figure 4(c)’s SEM micrograph are in such an orientation showing the planar surface orientation of the lath within the grain rather than the thickness of the lath. These secondary phases can terminate by impinging into other laths or continue through the lath upon the same plane or a parallel plane with a step at the interface of two laths, figure 5(c) and (d). The serial sectioned 3D volume, figure 6, revealed that these laths do and do not span the TaC grain. This would suggest that they precipitated after the TaC grain formed. The multiple directions and, in some cases, not spanning the entire grain suggest that this composition’s secondary phase content and/or formation sequence has little effect on controlling the microstructure’s grain morphology.

The  $\text{Ta}_{63}\text{C}_{37}$  specimen had a distinct grain morphology as compared to the former two compositions. The secondary phases were thin in thickness, similar to 55Ta:55C, but these phases were parallel with each other (no multiple directions) and spanned the entire interior of the acicular grain. This would suggest that the orientation relationships between TaC and  $\text{Ta}_2\text{C}/\text{Ta}_4\text{C}_3$  for this composition and/or volume fraction of secondary phases contributes significantly to the grain morphology. Similar to the low misfit interface relationship between TaC and  $\text{Ta}_4\text{C}_3$ , TaC has a closed packed plane and closed packed direction orientation relationship with  $\text{Ta}_2\text{C}$ , with a lattice misfit of 1.27 %. These low energy interfaces provide anisotropic growth directions so that the phases increase in length rather than thickness. While

exact atomic positions cannot be taken directly from the on-axis lattice fringes [18] in figure 7(e), the approximate structure of the  $Ta_4C_3$  phase, having a unit cell 3.10 nm c-axis length [9] is evident. The contrast of intensities of the fringes in this image is attributed to the non-uniform spacing of the  $Ta_4C_3$  laths within the TaC matrix. The numerous close stacking of the laths controlled the minor-axis thickness of the acicular grain where as the continuous expansion of the low misfit interface controlled the extent or length of the major-axis of the acicular grain. Using the understanding of anisotropic growth directions which are driven by the low misfit orientation relationships, the resultant grain morphology is dependent upon amount of the secondary phase. As the secondary phase content increases, it can dominate the TaC microstructure by transforming it from an equiaxed to an acicular in grain morphology.

## 5. Conclusion

A series of 53Ta:47C, 55Ta:45C, and 63Ta:37C specimens have been VPS, sintered and HIP'ed processed. In the 53Ta:47C VPS as-sprayed condition, a distribution of grain sizes and phases existed. Upon the subsequent sintering, the grain size became uniform and equiaxed. The post-VPS processing also homogenized the phase content to be single phase TaC. Upon fabricating specimens with less carbon content, the precipitation and stabilization of  $Ta_4C_3$  and  $Ta_2C$  was secured. For the 55Ta:45C specimen, an equiaxed grain structure with secondary phases of  $Ta_4C_3$  precipitated on multiple variants of  $\{111\}$ . These phases spanned and did not span the entire interior of the grain and formed a cross-hatch structure within the grains. The 63Ta:37C specimen exhibited an acicular grain morphology. The precipitation of  $Ta_4C_3$  and  $Ta_2C$  was found to all be parallel to the major-axis of the acicular grain with each grain consisting of a multiple stacking of these secondary phases. These phases also spanned the entire length of the major axis direction of the acicular grain. Based upon the low lattice misfit for the

orientation relationship between these phases and TaC, these low interfacial energy planes dominate. Consequently this yields an anisotropic growth direction that changes the grain morphology from equiaxed to acicular with increasing volume fraction of the secondary phase content with TaC.

## 6. Acknowledgement

The R.A. Morris and G.B. Thompson gratefully acknowledge funding support from the Army Research Office under grant W911NF-08-1-0300, Dr. David Stepp program manager.

## 7. References

- [1] E K Storms, "The Tantalum-Tantalum Carbide System," in *The Refractory Carbides.*: Academic Press, 1967.
- [2] C. R. Wang, J. M. Yang, and W. Hoffman, "Thermal stability of refractory carbide/boride composites," *Mater. Chem. Phys.*, **74**(3)(2002) 272-281
- [3] K. Upadhyay, J. M. Yang, and W. P. Hoffman, "Materials for Ultrahigh Temperature Structural Applications," *Am. Ceram. Soc. Bull.*, **76**(12)(1997) 51-56
- [4] K. Balani, G. Gonzalez, A. Agarwal, R. Hickman, and J. S. O'Dell, "Synthesis, Microstructural Characterization, and Mechanical Property Evaluation of Vacuum Plasma Sprayed Tantalum Carbide," *J. Am. Ceram. Soc.*, **89**(4)(2006) 1419-1425
- [5] G. Santoro and H. B. Probst, "An Explanation of Microstructures in the Tantalum-Carbon System," in *Adv. X-Ray Anal.*, **7**, 1963, pp. 126-135.
- [6] F. Lissner and T. Schleid, "Redetermination of the Crystal Structure of di-Tantalum mono-Carbide, Ta<sub>2</sub>C," *Z. Kristallogr. NCS*, **216**(6)(2001) 329
- [7] A. L. Bowman, "The Variation of Lattice Parameter with Carbon Content of Tantalum Carbide," *J. Phys. Chem. A* , **65**(9)(1961) 1596-1598
- [8] O. M. Barabash and Y. N. Koval, *A Handbook on the Structure and Properties of Metals*

*and Alloys*. Kiev: Naukova Dumka, 1986.

- [9] A. I. Gusev, A. S. Kurlov, and V. N. Lipatnikov, "Atomic and Vacancy ordering in carbide  $z\text{-Ta}_4\text{C}_{3-x}$  and Phase equilibria in the Ta-C system," *J. Solid State Chem.*, **180**(2007) 3234-3246
- [10] K. Yvon and E. Parthe, "On the Crystal Chemistry of the Close Packed Transition Metal Carbides. I. The Crystal Structure of the  $z\text{-V}$ , Nb, and Ta Carbides," *Acta Crystallogra.*, **26**(1970) 149-153
- [11] D. J. Rowcliffe and G. E. Hollox, "Plastic Flow and Fracture of Tantalum Carbide and Hafnium Carbide at Low Temperatures," *J. Mater. Sci.*, **6**(1971) 1261-1269
- [12] R. Morris, D. Butts, S. DiPietro, A. Craven, L. Matson, and G. Thompson, "Comparison between HIP and VPS tantalum carbides microstructure morphologies," in *SAMPE 2009 Technical Conference Proceedings*, Baltimore, MD, May 18-21, 2009, pp. 1-10.
- [13] R. R. Kieschke, K. A. Roberts, and T. Clyne, "Instabilities in the vacuum plasma spraying process," *Surf. Coat. Technol.*, **46**(1)(1991) 25-38
- [14] A. Nesmeianov, *Vapor pressure of the chemical elements*.: Elsevier Pub. Co., 1963.
- [15] R. M. German and S. J. Park, *Mathematical relations in particulate materials processing: ceramics, powder metals, cermets, carbides, hard materials and minerals*.: John Wiley & Sons. Inc., 2008.
- [16] H. O. Pierson, *Handbook of Refractory Carbides and Nitrides*. Westwood, New Jersey: Noyes Publications, 1996.
- [17] R. W. G. Wyckoff, *Crystal Structures*, 2nd ed. New York: Interscience Publishers, 1963.
- [18] J. M. Cowley, *Diffraction Physics*, 3rd ed. Amsterdam, The Netherlands: Elsevier Science B. V., 1995.
- [19] D. B. Williams and C. B. Carter, *Transmission electron microscopy: a textbook for materials science*. New York, N.Y.: Springer Science, 1996.
- [20] P. A. Midgley and M. Weyland, "3D electron microscopy in the physical sciences: the development of Z-contrast and EFTEM tomography," *Ultramicroscopy*, **96**(2003) 413-431
- [21] D. J. Rowcliffe, "Structure of Non-Stoichiometric TaC," *Mater. Sci. Eng.*, **18**(1975) 231-238

- [22] B. Schulz, B. Wang, D. Butts, and G. Thompson, "TaC with HfC,"
- [23] G. Gottstein, *Physical foundations of materials science.*: Springer-Verlag Berlin Heidelberg, 2004.
- [24] W. F. Brizes, "Diffusion of Carbon in the Carbides of Tantalum," *J. Nucl. Mater.*, **26**(1968) 227-237

## CHAPTER 4

### FORMATION OF OXIDE INCLUSIONS AND POROSITY IN VACUUM PLASMA SPRAYED TANTALUM CARBIDES MICROSTRUCTURES<sup>3</sup>

#### Abstract

A vacuum plasma sprayed (VPS) tantalum carbide specimen was fabricated from TaC powder. During its fabrication, oxide-based inclusions from intrinsic impurities in the powder and/or low level oxygen in the processing chamber formed an interconnected globular structure within the matrix phase and in the grain boundaries. The oxygen source was intrinsic impurities in the powder and/or low background pressure in the processing chamber. The oxides phases were identified to be Ta<sub>2</sub>O<sub>5</sub> and TaO through selected area electron diffraction. Serial sectioning and 3D reconstruction was used to quantify the globular oxide structure. The porosity inherent in the VPS process is also investigated using this 3D technique.

---

<sup>3</sup> A manuscript has been prepared for the work in this chapter for the publication in the Journal of American Ceramics Society as : R.A. Morris, G.B. Thompson, "Formation of Oxide Inclusions in Vacuum Plasma Sprayed Tantalum Carbides Microstructures."

## 1. Introduction

Transition metal carbides have a large assortment of applications because of their high hardness, chemical resistance, and high melting temperatures [1,2,3]. Tantalum carbide (TaC) and its sub-stoichiometric Ta<sub>2</sub>C and Ta<sub>4</sub>C<sub>3</sub> phases have emerged as candidate materials for ultra-high temperature structural applications because of their extremely high melting temperatures and their ability to jointly tailor the microstructure through their phase precipitation within the matrix material [4]. One of the consequences of TaC's high melting temperature is the limited number of processing methods capable of fabricating near full density tantalum carbides. In general, hot-isostatic pressing (HIP), spark-sintered processing, arc melting, or vacuum plasma spraying (VPS) of powders are the viable means to fabricate tantalum carbides [5]. In the VPS method, the tantalum carbide powders are fed into a plasma gun where they are melted and exit the gun at high velocities. The molten particles are deposited onto a substrate where upon it solidifies and a tantalum carbide phase is built up through continuous deposition.

The formation of oxides and pores within these structures can adversely affect the mechanical properties [6]. These oxides can form from intrinsic oxygen impurities in the starting powders, from background oxygen levels not purged from the fabrication chamber or environmental oxidation during operation. There have been studies of the oxide formation in various carbide materials [7,8,9,10], but, to date, there is very limited work about the formation of oxide inclusions within tantalum carbides [11,12]. In spite of the numerous studies on the chemistry of tantalum, reliable evidence for the existence of independent forms of tantalum monoxide (TaO) is still absent [13,14,15]. Additionally, studies of the inherent formation of porosity, its sizes and distributions in tantalum carbides, are limited [1,16].

In the present research, a tantalum carbide specimen has been vacuum plasma sprayed from TaC powders and post-processed by sintering and hot isostatic pressing (HIP) to reveal microstructures containing oxide inclusions [4]. This paper investigates the formations of these oxides and pores form within the tantalum carbide matrix and how this influences the microstructure morphology.

## 2. Experimental

A tantalum carbide specimen was fabricated by the VPS process from TaC powders produce using a carbo-thermal reduction of  $Ta_2O_5$ , with the processed specimen having an approximate atomic composition of 61Ta:39C. The reduction reaction is as follows:  $Ta_2O_5 + 7C \rightarrow 2TaC + 5CO$ . The spraying chamber was evacuated to 13 Pa using mechanical pumps and backfilled with argon to a pressure of 27 kPa. A 70 argon: 1 hydrogen gas mixture served as the carrier gas for the TaC feedstock powder in the tungsten cathode plasma gun. The VPS process inherently loses some carbon because of either reactions forming hydrocarbons with the carrier gas and/or vapor pressure differences between carbon and tantalum under the processing temperatures and pressures [4,17]. Post-VPS fabrication, the graphite mandrel was mechanically ground away whereupon the 61Ta:39C specimen was sintered under a vacuum environment in a graphite furnace near  $0.5 T_m$ , where  $T_m$  is the melting temperature, to help reduce the porosity inherent in the VPS fabrication method [1]. Post-sintering, the 61Ta:39C specimens were approximately 95+ % dense. To further reduce porosity and homogenize the microstructure, the specimens were HIP'ed at 200 MPa in an argon atmosphere near  $0.5 T_m$ . The post-HIP densities were >98 % dense. The density measurements were done by a water immersion displacement technique [18] and compared to the theoretical density of 14.5 g/cc for TaC and 14.8 g/cc for

Ta<sub>2</sub>C [19]. Since the volume fraction of each phase was estimated, the densities given are approximate.

Post-manufacturing, the 61Ta:39C specimen was sectioned via a diamond saw. The ‘interior’ portion (not free surfaces or edges) of the 61Ta:39C specimen was examined for the subsequent analysis. The specimen was mounted in cross-section, mechanically ground and polished to 3 micron diamond abrasive paste and then Vibromet® polished for 24 hours in aqueous 0.05 micron silica slurry. The microstructure was imaged using either secondary electron or ion contrast imaging in a FEI Quanta 3D dual beam focus ion beam (FIB) - scanning electron microscope (SEM) operated at 30 keV. The FEI Quanta 3D microscope’s ion beam was used to perform a series of serial sectioning [20] and imaging steps to reveal the depth dependent change in microstructure.

For the FIB-based serial sectioning analysis, the top and side surface of the specimens were polished to a final grit of 0.05 µm colloidal silica suspension after which they were adhered onto an SEM aluminum stub and a 10 µm x 10 µm isolated pillar surrounding the region of interest (ROI) was FIB milled out of the edge of the specimen. This is shown in the schematic diagram of figure 1. A protective platinum cap, ~2 µm, was deposited onto the surface of the pillar to reduce the amount of ion damage and implantation into the analysis volume of the ROI. A circular fiducial marker was placed on the top and side surface which was imaged for each cut and used in the subsequent alignment procedures for each 2D image that reconstructed the 3D volume [20]. The pillar was FIB-milled at 1 nA at steps sizes of 100 nm using an automated runscript. The revealed milled surface was imaged after each consecutive cut using ion contrast imaging. Though ions are implanted in this condition, the short exposure and crystallographic (channeling) orientation dependence resulted in superior contrast of the grains and phases as

compared to traditional SEM imaging. The collected images were compiled and reconstructed into the 3D rendering of the microstructure using VSG Avizo® Fire edition software platform.

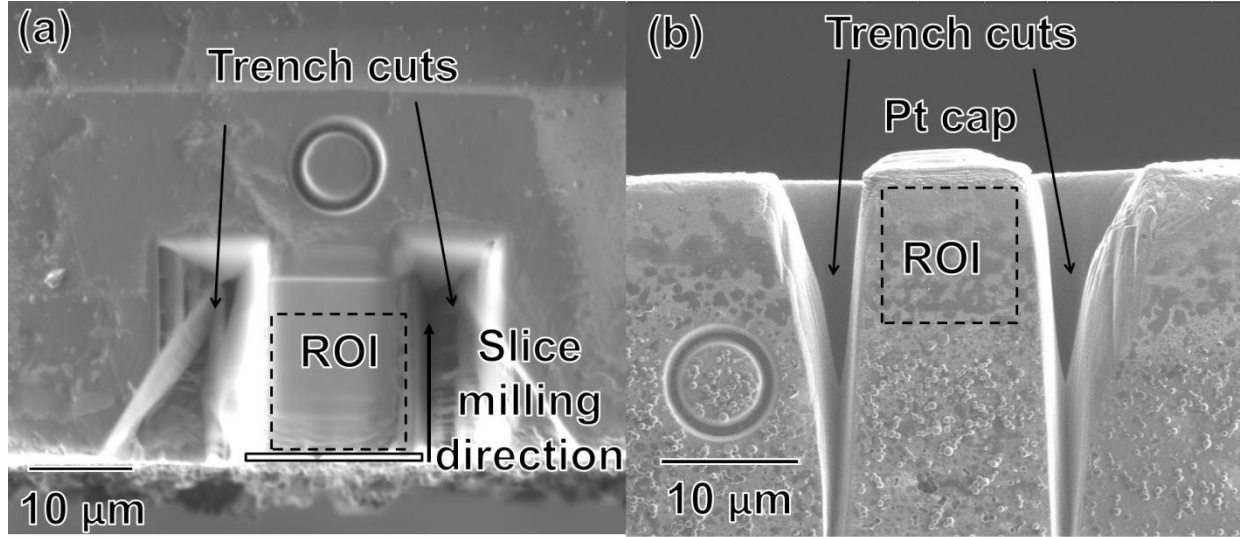


**Figure 1:** Serial sectioning sample preparation. (a) Top view of milling area showing trench cuts on either side of ROI along with a box drawn to represent a milling slice. (b) Side view of initial imaging area showing the fiducial marks for image alignment.

X-ray diffraction for phase identification and estimated volume fraction determination was done using a Bruker Discovery D8 General Area Diffraction Detector System with Cu-K $\alpha$  radiation at 45 keV and 40 mA as the source. The TaC, Ta<sub>2</sub>C, and Ta<sub>4</sub>C<sub>3</sub> phases were identified using data from Wyckoff [21], Lissner [22], and Gusev *et al.* [23] sources, respectively. The phase content is tabulated in Table 1 and was estimated by the integrated intensity of the theoretically most intense peak for each phase, which are the {111}<sub>TaC</sub>, {107}<sub>Ta<sub>4</sub>C<sub>3</sub></sub>, and {1011}<sub>Ta<sub>2</sub>C</sub> reflections [21,23,22], divided by the sum of all maximum peak intensities [24]. The oxide phases, TaO and Ta<sub>2</sub>O<sub>5</sub>, which were not observed in the XRD diffractogram because of their extremely small volume fraction but determined by electron scattering, given below, and compared to data reported by Schonberg [15] and Zibrov *et al.* [25], respectively.

**Table 1:** XRD data for the starting powders and VPS process sample. The XRD values represent the volume estimates of each phase.

	XRD		
	TaC	Ta <sub>4</sub> C <sub>3</sub>	Ta <sub>2</sub> C
Powder	100	0	0
Bulk	28	70	2

SEM-energy dispersive spectroscopy (EDS), collected on an EDAX Apollo XV silicon drift detector, was used to determine the approximate tantalum and carbon composition of the specimen using an electron beam setting of 10 keV and 3.3 nA. A standard 51Ta:49C was used for calibrating the EDS instrument. To provide a complimentary comparison to the EDS composition measurements, a lever rule approximation using the determined volume fractions of each phase from XRD was performed and had good agreement to the EDS results. Since tantalum is a much higher atomic number than carbon, the authors were concerned about carbon X-ray absorption by tantalum [26]. A series of Monte-Carlo simulation [27] of electron scattering in tantalum carbide at 10, 20 and 30 keV is plotted in figure 2(a). The electron density volume from a 30 keV source is approximately 5 times that of a 10 KeV source. The reduction in excitation volume reduces the effect of carbon absorption. Figure 2(b) is a plot of the standard 51Ta:49C composition at the three different acceleration voltages. Clearly, a reduction in voltage improved the fidelity of the EDS analysis.

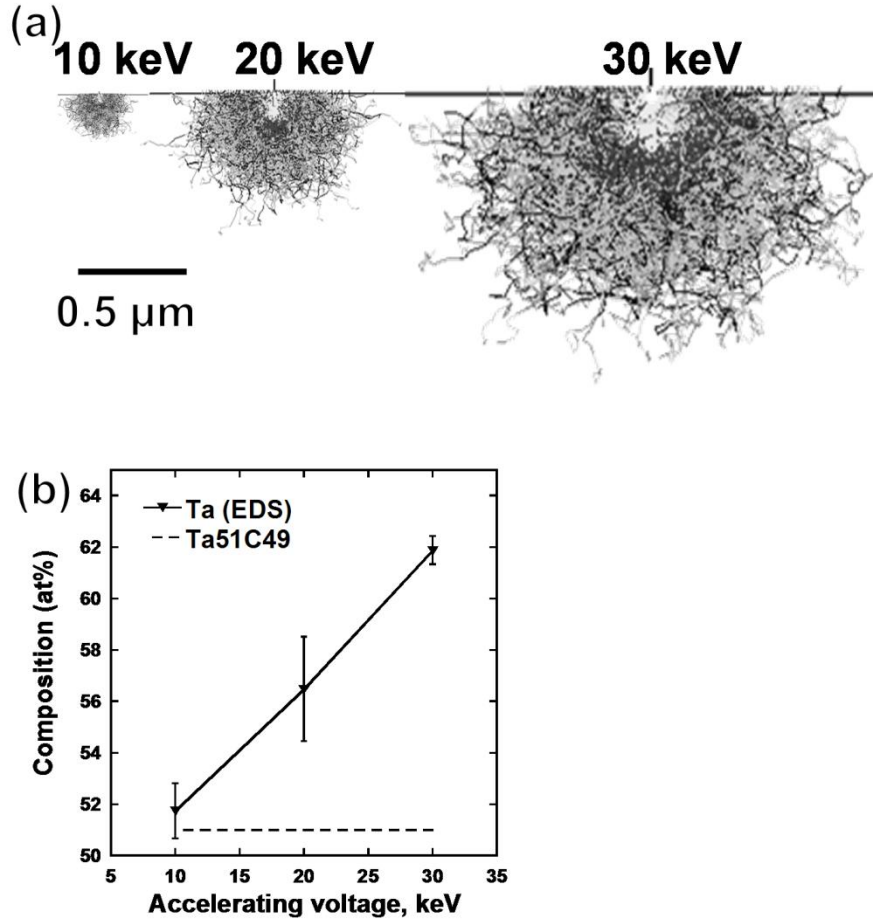


**Figure 2:** (a) Monte-Carlo simulation of the electron beam interaction within the TaC material showing larger volume of interaction for higher accelerating voltages. (b) A plot of the variation of Ta content for different accelerating voltages on a 51Ta:49C sample.

Transmission electron microscopy (TEM) imaging and selected area electron diffraction (SAED) was performed using an FEI F20 Tecnai TEM at 200keV for phase identification. In addition to bright-field (BF) TEM imaging, complimentary Scanning TEM (STEM)- high angle annular dark field (HAADF) or Z-contrast imaging was used. Z (atomic number)-contrast imaging is the collection of incoherent scattered electrons that are sensitive to nucleus mass [28]. The elements with a higher mass, such as tantalum are scattered more; therefore, tantalum-rich phases are brighter in the STEM-HAADF micrographs.

### 3. Results & Discussion

#### *i. Initial powders*

The initial TaC powders were produced using a carbo-thermal reduction of Ta<sub>2</sub>O<sub>5</sub>. Manufacturing of this powder using this method could result in incomplete transformation of the Ta<sub>2</sub>O<sub>5</sub> oxide, and leave a residual oxide within the powder. Analysis of the composition of the starting powders used to fabricate the specimen was performed. Data collected using an Inert Gas Fusion instrument from LECO found there to be 1300 ppm of oxygen in the powder. The oxygen was found to be distributed uniformly throughout the powders, shown by the EDS spectral map in figure 3(d). The carbon and tantalum compositions were found to be 54 at % and 42 at %, respectively. The powder was stoichiometric TaC with excess carbon in the blend to help reduce off-set from carbon loss in the VPS process. XRD was also performed on the powders, shown in figure 4(a), and only the TaC phase was evident. In the previous and subsequent reporting of the tantalum carbide composition, the oxygen level is not given to avoid potential confusion of an initially fabricated oxy-tantalum-carbide powder.

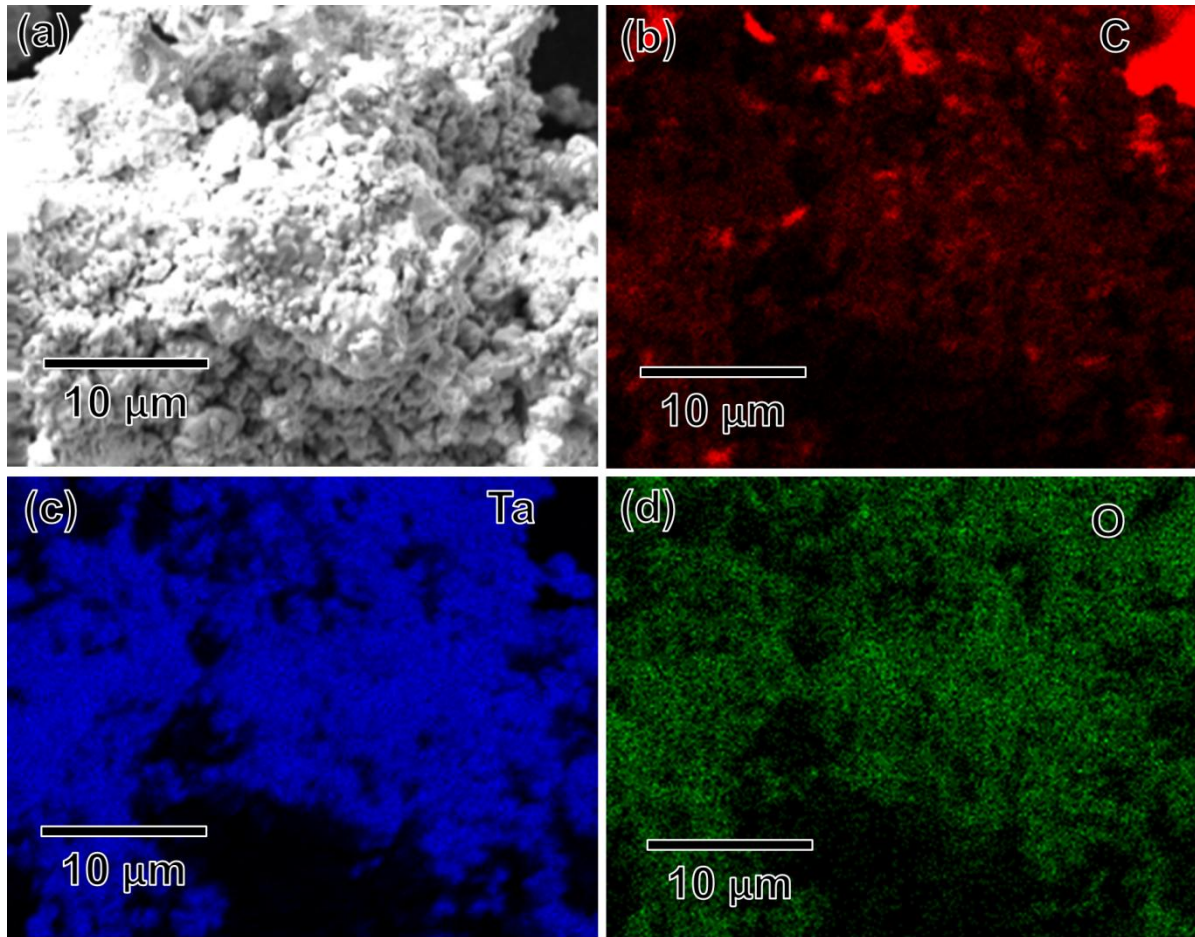


**Figure 3:** SEM image and EDS spectral maps of the starting powder. (a) SEM image of powder showing the region where the EDS spectral maps were taken. EDS spectral map of (b) carbon, (c) oxygen, and (d) tantalum.

ii. *Tantalum carbide microstructure*

After the VPS processing, XRD was performed on the specimen to determine the resultant phase content, plotted in figure 4(b) and (c). The specimen was found to consist of the TaC, Ta<sub>4</sub>C<sub>3</sub>, and Ta<sub>2</sub>C phases. The phase content was determined to be 28 vol. % TaC, 70 vol. % Ta<sub>4</sub>C<sub>3</sub>, and 2 vol. % Ta<sub>2</sub>C, tabulated in Table 1, using the methodology described earlier. EDS revealed the overall bulk composition to be 61Ta:39C. While there were regions of oxide inclusions within the microstructure, the oxygen content did not contribute to the bulk EDS

composition as the amount was less than 1% for the atomic composition of the post-processed specimen. Micrographs of the specimen, figure 4(d), showed an acicular microstructure. Within the microstructure, as will be discussed in a later section, there were oxide inclusions and pores.

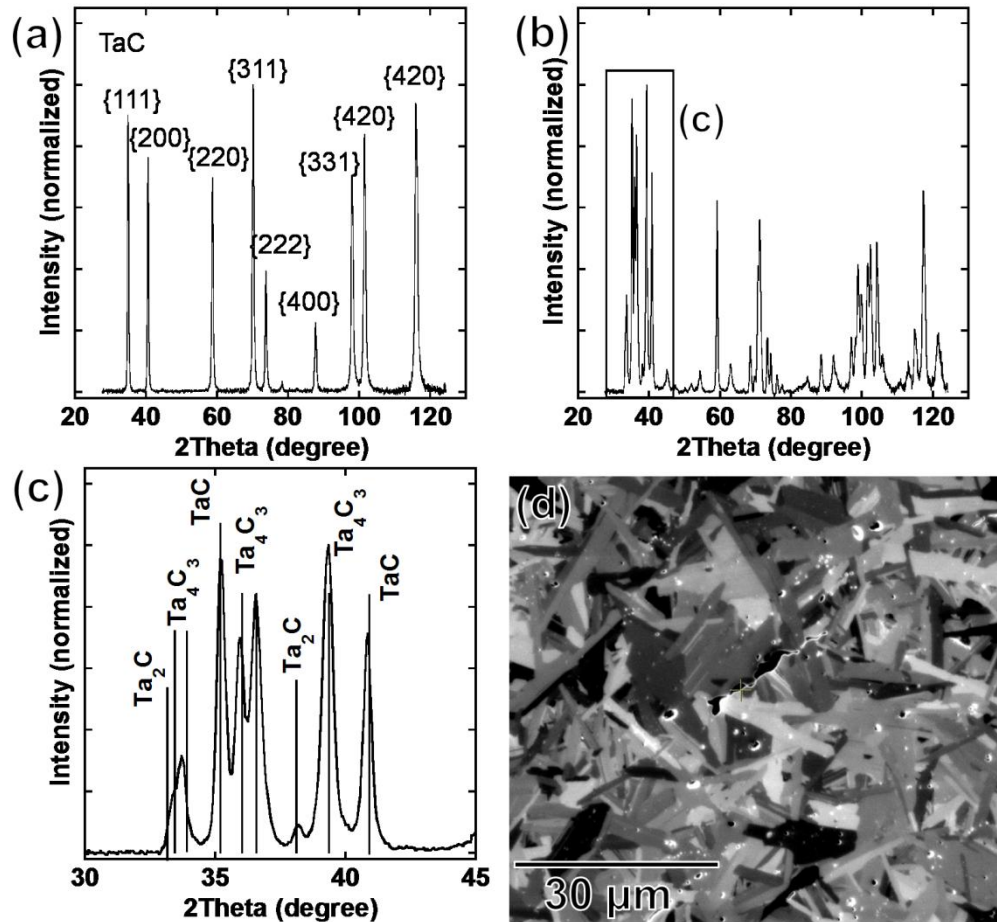


**Figure 4:** XRD and SEM micrographs of 61Ta:39C specimen (a) XRD plot of starting powder revealing only the TaC phase present. (b) XRD of the VPS processed 61Ta:39C specimen. (c) Enlarged region of XRD plot in (b) showing the multiple identified Ta-C phases. (d) SEM micrograph showing the acicular microstructure of the 61Ta:39C specimen.

The high magnification SEM and TEM imaging revealed that the acicular grains were comprised of a fine lath structure of the secondary phases frequently running along the major-axis of the grain, figure 5. This layered lath stacking is clearly evident in the magnified STEM-

HAADF image of figure 5(a). Figure 5(a) shows grains containing differing amounts of phase content, with the Ta-rich  $Ta_4C_3$  phase having a brighter contrast than that of the TaC phase. This variation in grain contrast suggest that the microstructure is not completely homogenous, with different grains containing a varied ratio of tantalum and carbon, as seen in work by Rowcliffe [29]. The phases were identified by the SAED patterns in figure 5(b) and (c). Previous work has shown these laths are also  $Ta_2C$  [4] and is present in the microstructure evident by the XRD results of figure 4. Comparing the SAED to a simulated electron diffraction of a multiphase grain oriented in the  $\langle 110 \rangle$  in figure 5(c) revealed the phases TaC and  $Ta_4C_3$  have the following orientation relationship as previously determined by [4,29]:  $\{111\}_{TaC} // \{0001\}_{Ta_4C_3}$  and  $\langle 110 \rangle_{TaC} // \langle 101\ 0 \rangle_{Ta_4C_3}$ . A STEM-HAADF image in figure 5(e) clearly reveals irregularly spaced bright bands of  $Ta_4C_3$  forming parallel to each other on a specific  $\{111\}_{TaC}$  plane. The irregular spaced planes are likely a result of the carbon diffusivity in the matrix that leads to the precipitation of  $Ta_4C_3$  (and  $Ta_2C$ ) on specific planes. The high resolution STEM-HAADF micrograph in figure 5(f) shows near atomic scale imaging of the tantalum atoms of the highlighted region in figure 5(d).

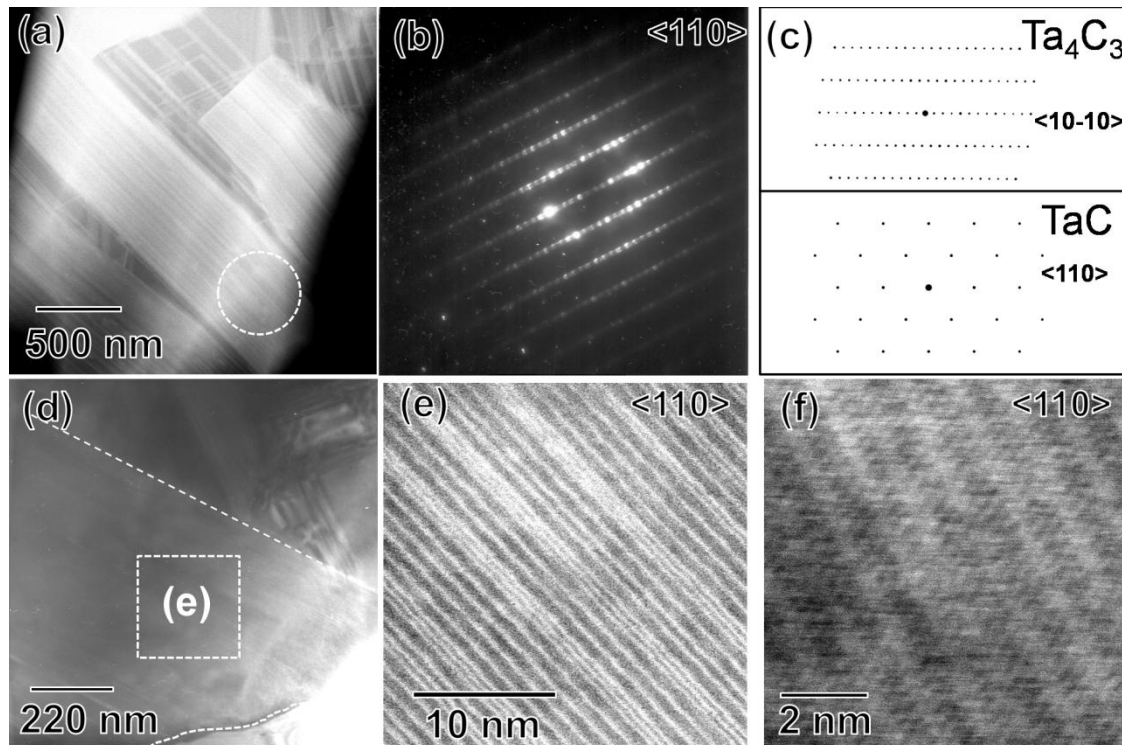


**Figure 5:** TEM data of 61Ta:39C specimen **(a)** STEM-HAADF of a multiphase grain showing a banded structure within the grains. **(b)** Selected area diffraction of a grain highlighted in **(a)** identified as both the TaC and Ta<sub>4</sub>C<sub>3</sub> phases. **(c)** Simulated electron diffraction patterns of the Ta<sub>4</sub>C<sub>3</sub> and TaC phases showing the orientation relationship between the two phases. **(d)** Bright field TEM image of a grain containing a banded lath structure. **(e)** STEM-HAADF image of the banded structures in **(d)** showing planes of tantalum-rich concentrations. **(f)** Highly magnified STEM-HAADF image revealing near atomic scale structure of the banded phase structure.

### iii. Oxide inclusion microstructure

As shown previously in the EDS spectral maps, oxygen was present in the initial powders as an impurity. Using SEM and TEM, it was found that there were regions within the microstructure that contained globular formations of an oxide inclusion. These oxides likely formed from the initial powder impurities and/or background levels of oxygen in the subsequent processing of the carbide. The lack of oxide based XRD peaks indicates these phases are of insufficient volume fraction. They were noticeably sporadic in the microstructure. SEM imaging, figures 6(a) and 7(a), show an elongated oxide structure, as determined from the EDS spectral

map of a similar region, shown in figure 6. Figure 6(c) shows a concentration of oxygen within the globular structure. Approximate composition of this oxide inclusion was determined to be 38Ta:62O using EDS.

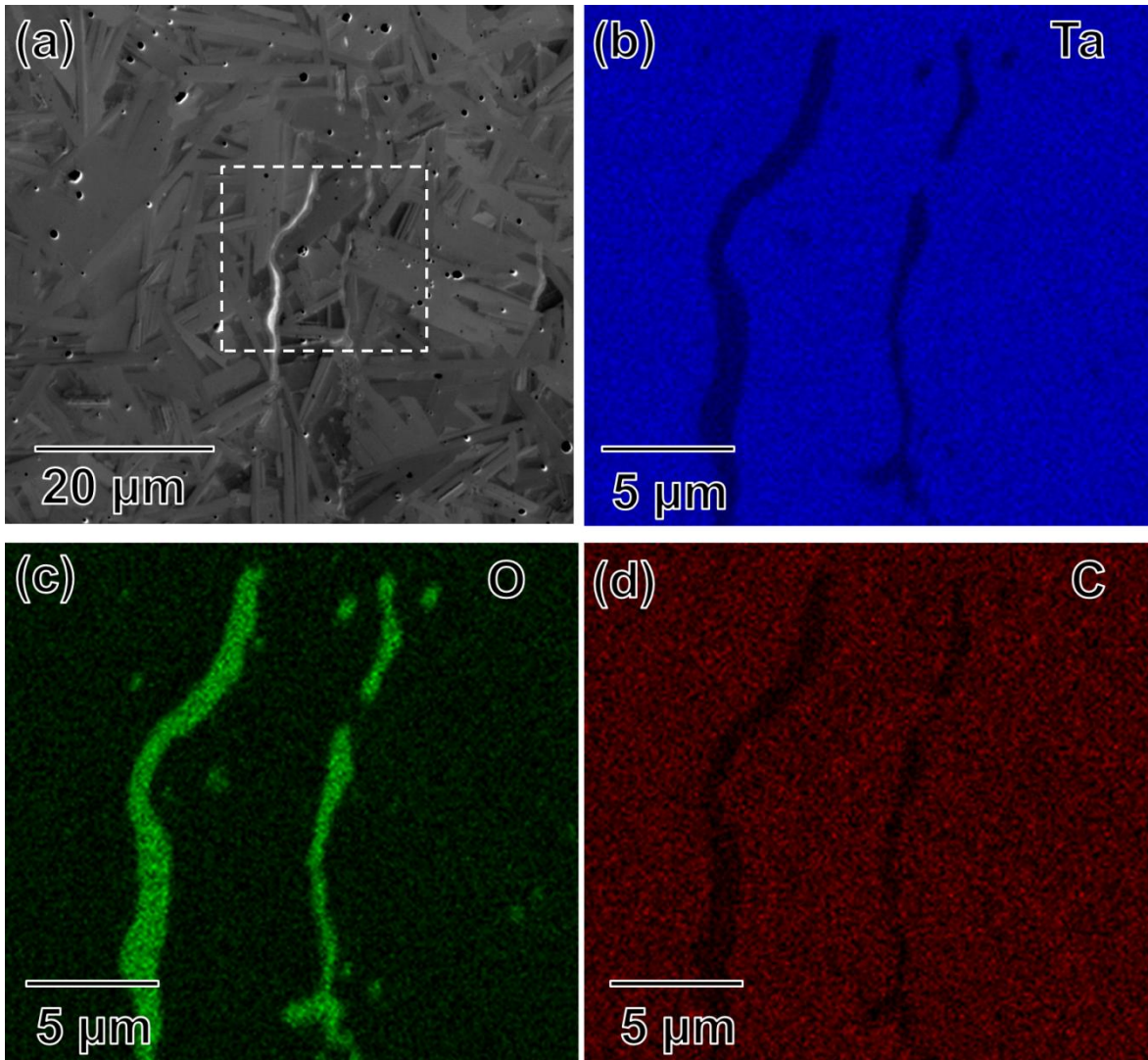


**Figure 6:** SEM image and EDS spectral maps of the 61Ta:39C sample with an oxide inclusion. (a) SEM image showing region where the EDS spectral maps were taken. EDS spectral map of (b) tantalum, (c) oxygen, and (d) carbon.

To further investigate the oxide phase, a TEM foil was prepared using traditional preparation techniques of cutting a 3 mm diameter disc from the specimen, grinding to < 100 μm in

thickness, dimpled to  $< 15 \mu\text{m}$  and Ar ion milled to electron transparency. STEM-HAADF micrographs revealed that an oxide phase was captured in the prepared foil, as highlighted in figure 7(b). The STEM-HAADF image shows a globular oxide structure surrounded by the acicular  $\text{Ta}_x\text{C}_{1-x}$  grains (the 'x' subscripts are used to account that multiple phases that exist in these grains as seen in figure 5). A STEM-EDS line profile within this oxide region was performed and is plotted in figure 7(c). The oxide was found to be crystalline, as shown by the lattice fringe images in figure 7(d-e). A Fast Fourier Transform (FFT) of the lattice fringe image, shown in the inset in figure 7(d), matches the SAED pattern taken down the  $\langle 001 \rangle$  zone, figure 5(f). The phase was determined to be tantalum (II) oxide, TaO, and is consistent with the EDS profile. This is a surprising result considering TaO is a metastable oxide as compared to the more common  $\text{Ta}_2\text{O}_5$  [15]. Though TaO has similar lattice symmetry and constants with TaC [21], the oxide/ $\text{Ta}_x\text{C}_{1-x}$  interface forms in incoherent boundary, figure 6(e), and evident by the curved morphology. This curvature would suggest a driving force to minimize surface area-to-volume indicative of a high interfacial energy boundary between the phases.

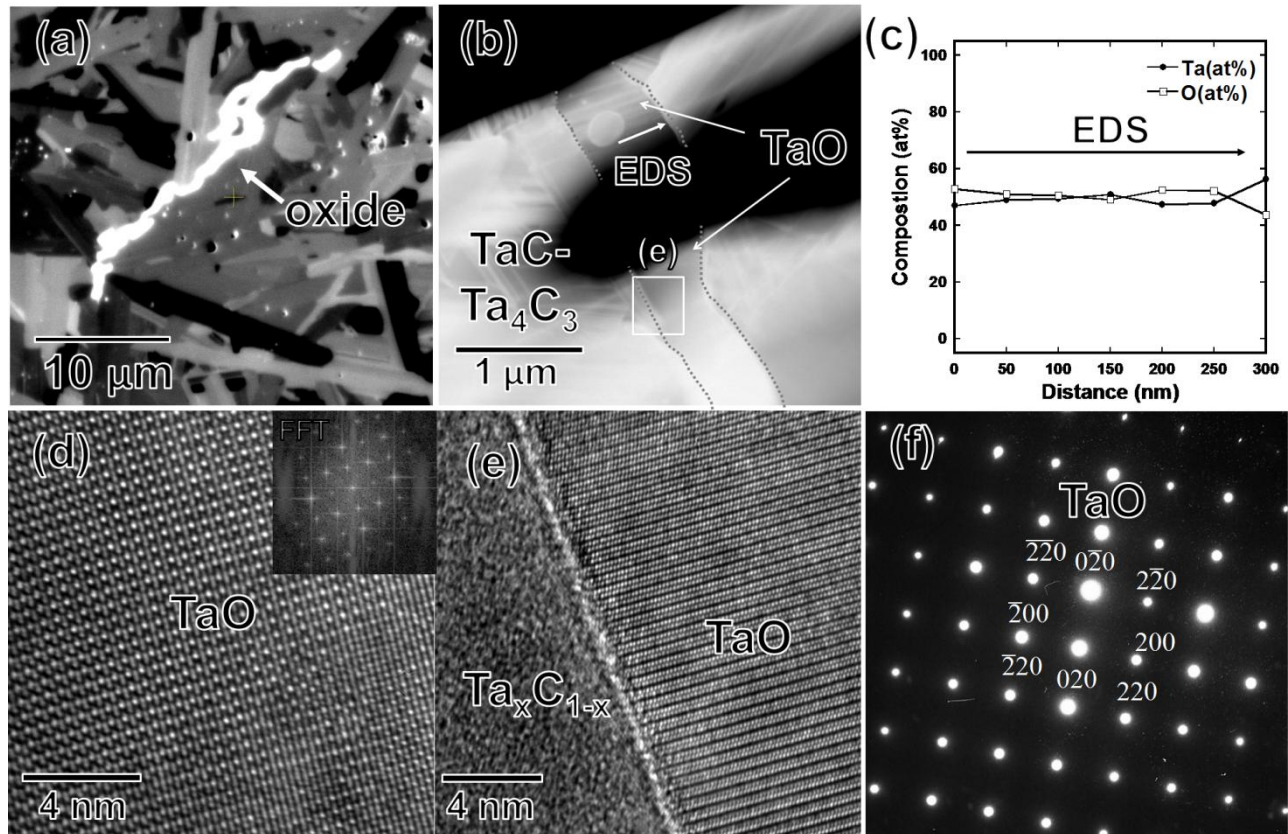


**Figure 7:** SEM and TEM micrographs of oxide inclusion within the 61Ta:39C microstructure (a) SEM image of an oxide inclusion within the 61Ta:39C microstructure showing the elongated nature of the oxide. (b) STEM-HAADF image of an oxide inclusion showing spatial locations of the EDS line profile and SAED. (c) STEM-EDS line profile of oxide inclusion. The arrow indicates direction of analysis. (d) Lattice fringe image of an oxide region in (b) with inset of a FFT. (e) Interface of the  $Ta_xC_{1-x}$  grain and TaO. (f) SAED of region in (d) identified as the TaO phase.

A similar TEM study of a different oxide inclusion was performed on the same specimen. Bright field imaging in figure 8(a) shows the region of interest with multiple elongated oxide grains. The selected area aperture was positioned over a specific oxide grain, figure 8(b). The SAED, figure 8(c), identified the grain to be  $\beta$ - $Ta_2O_5$  as viewed from the  $\langle 112 \rangle$  zone. A high magnification lattice fringe image of the same grain reveals a high order of crystallinity and the FFT of this image yields a similar pattern as the SAED, shown in figure 8(d). A STEM-HAADF

image in figure 8(e) shows the multigrain oxide inclusion within the  $Ta_xC_{1-x}$  microstructure. These multiple grains can give a banded appearance because of ion channeling with respect to their mis-orientations with each other, as is seen in a SEM micrograph, figure 9(a). A STEM-EDS line profile across this interface is plotted in figure 8(f) and confirms the chemistry of  $Ta_2O_5$ .

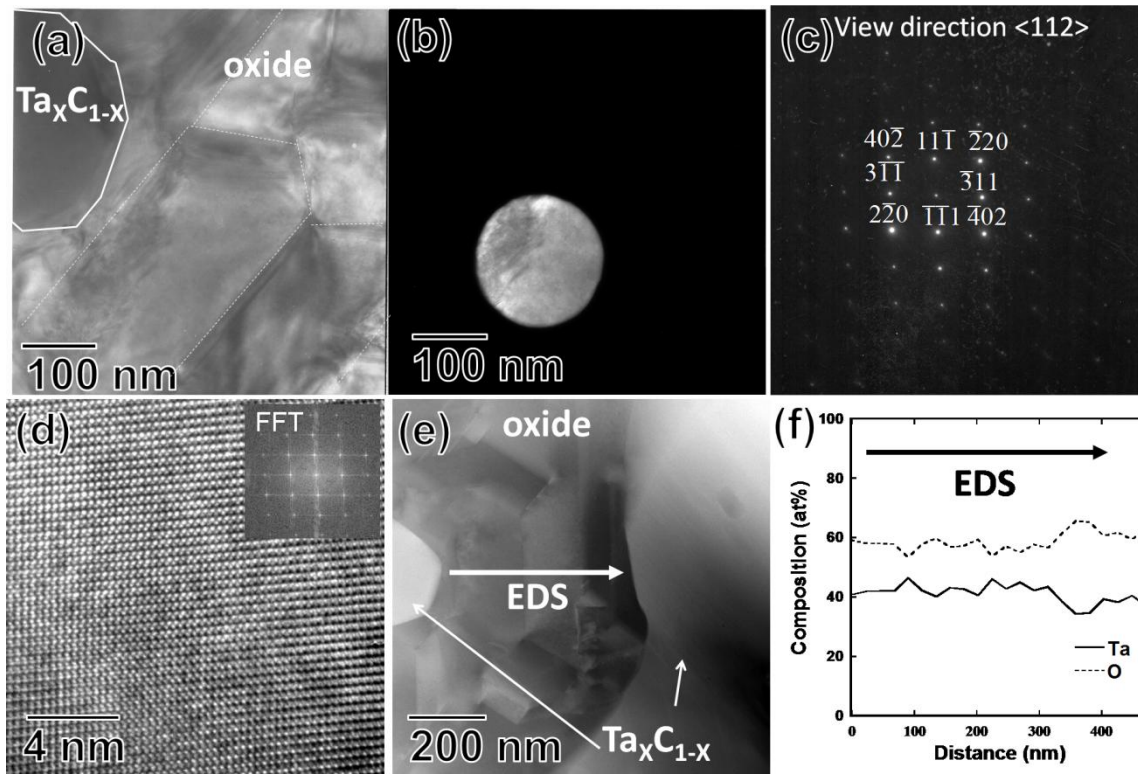


**Figure 8:** (a) Bright field TEM image of an oxide inclusion within the 61Ta:39C microstructure. (b) Selected area aperture of identified grain in (a). (c) SAED of (b) identified as the  $\beta$ - $Ta_2O_5$ . (d) Lattice fringe TEM image of the grain in (b) showing crystallinity and an inset of the FFT showing a similar diffraction pattern of  $\beta$ - $Ta_2O_5$  as seen in (c). (e) STEM-HAADF of region in (a) showing multiple oxide grains within the inclusion. (f) STEM-EDS line profile of oxide inclusion highlighted in (e) showing a consistent amount of oxygen present in the inclusion. The arrow indicates direction of analysis.

Traditional SEM and TEM imaging techniques only yield a 2D perspective on the microstructure, but it is obvious that the microstructure extends into three dimensions. To

characterize the shape of the oxide inclusions, a 3D serial sectioned reconstruction was performed. A computer generated reconstruction of the oxide inclusion, light grey features, is shown along with the porosity, indicated by the dark grey-smaller features, in figure 7(b). These features are enclosed by the final serial slice ion contrast images of the microstructure. The oxides are rounded and globular which in some cases were interconnected as one large feature. These interconnected oxide regions appear to have wetted and formed along the grain boundaries, figures 6 and 9 suggesting that they formed upon cooling since the oxide phases, have a lower melting point (~1800 C) than that of the  $Ta_xC_{1-x}$  phases [25]. This would suggest that oxygen is expelled from the matrix, if possible, and forms the stable pentaoxide phase, figure 8. If oxygen is contained in the matrix, at lower levels, than the possibility of forming the monoxide phase can occur, as seen in figure 7. The grain boundaries allow for rapid diffusion of oxygen to form the stable oxide phase. Surrounding these larger oxide inclusion clusters were smaller, spherical inclusions that were disconnected from the larger interconnected inclusions. figures 9(c) and (d) give alternate perspectives of an extracted oxide inclusion.

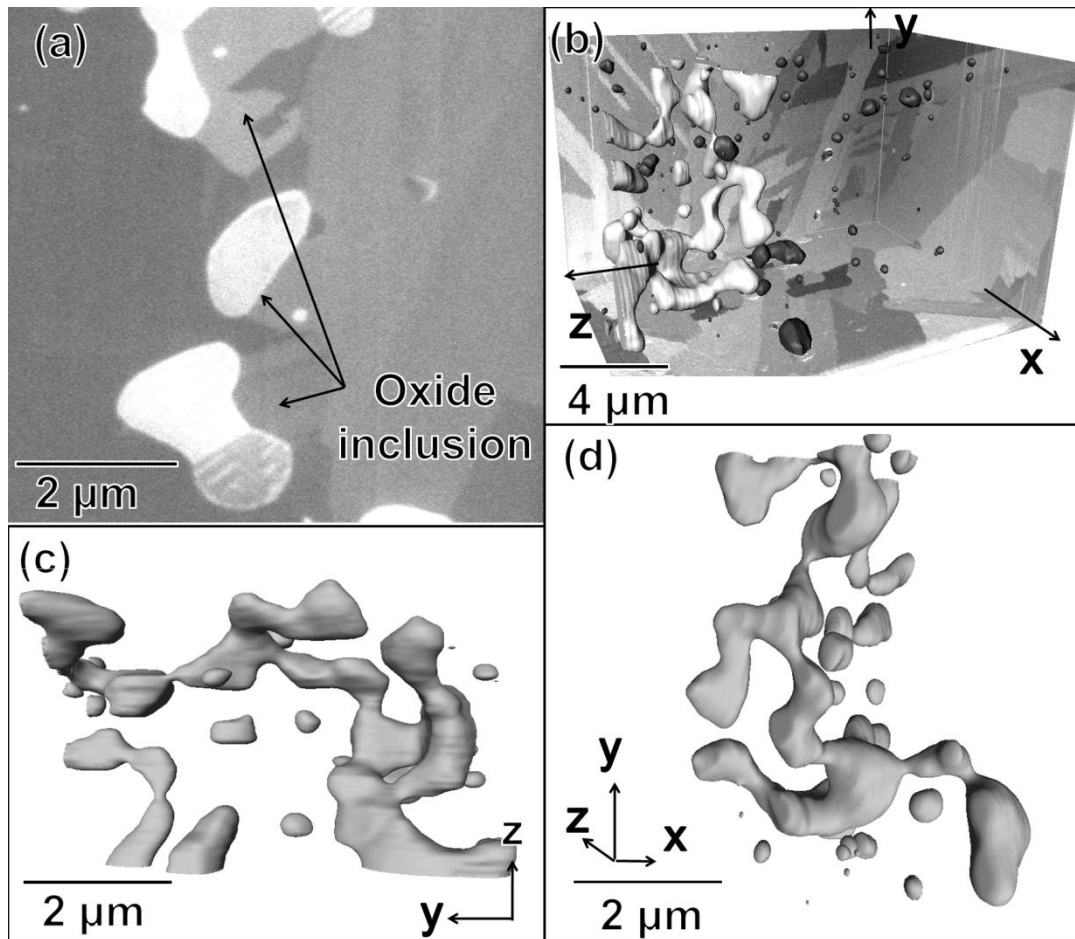


**Figure 9:** (a) A slice taken from the serial sectioned microstructure showing an inclusion. (b) 3D perspective of the reconstructed inclusions (light grey) and porosity (dark grey). (c-d) Different perspectives of the 3D reconstruction of the inclusion revealing an interconnected globular structure.

iv. *Porosity*

The porosity is an important physical characteristic in a microstructure in regulating the mechanical properties. Jun and Shaffer [6] found that the bulk modulus decreased in tantalum carbides with increasing porosity. In this specimen, the porosity was found to be randomly distributed throughout the microstructure, both at the grain boundaries and within the grains. The presence of pores, particularly within the matrix suggests that it is difficult to fully consolidate the

material. This is likely a result of this materials extremely high melting temperature ( $\sim 4000\text{ }^{\circ}\text{C}$ ) [30] and the inability to provide adequate temperature and/or pressure during processing of the carbides. The distribution of pore volumes is plotted in figure 10(a) with the majority of pores having a volume less than  $0.04\text{ }\mu\text{m}^3$  with a mean at  $0.046 \pm 0.134\text{ }\mu\text{m}^3$ . For the 3D serial sectioned volume,  $300\text{ }\mu\text{m}^3$ , the pores only accounted for  $5\text{ }\mu\text{m}^3$  or  $\sim 2\%$  of the volume. Figure 10(b-d) shows various viewing perspectives of the porosity.

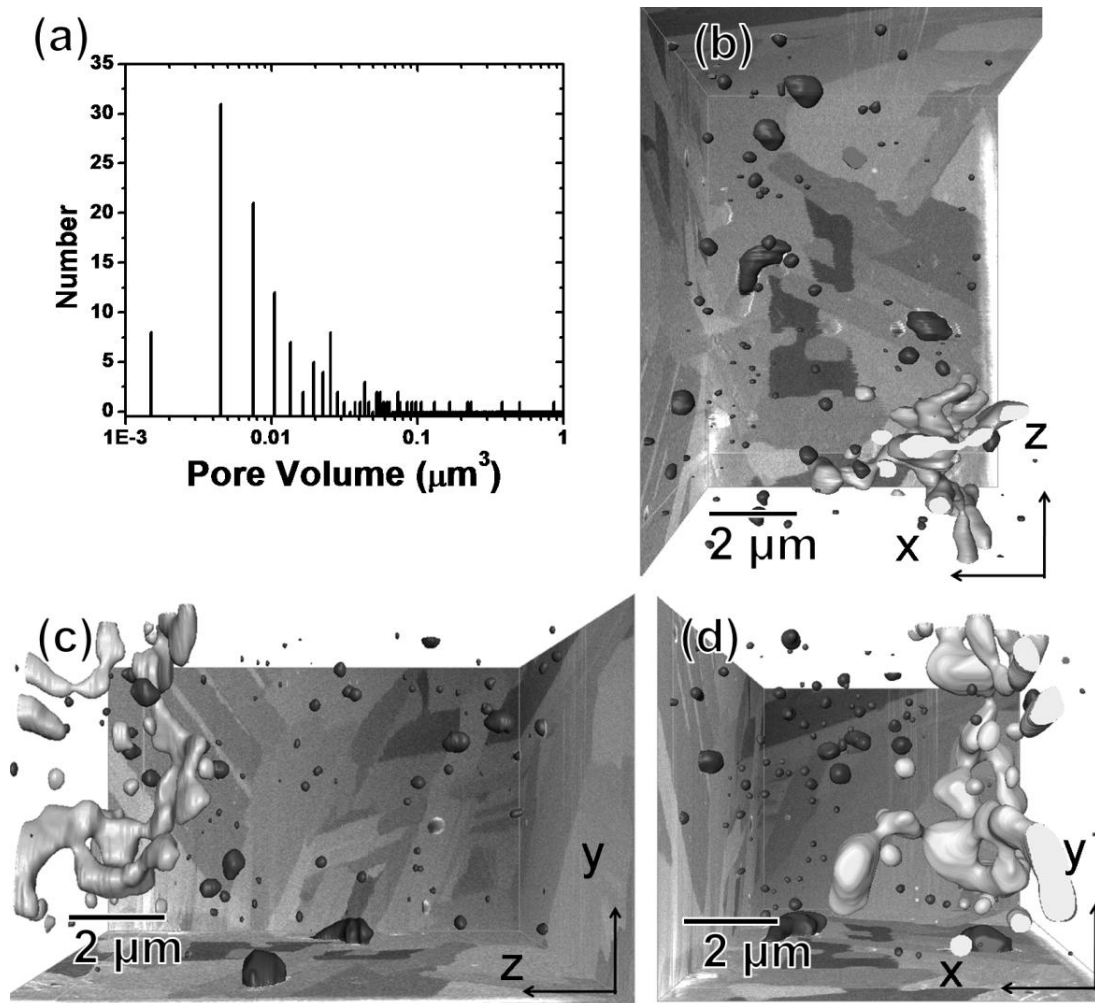


**Figure 10:** (a) Histogram of pore volume within the serial sectioned volume. (b-d) Multiple viewing perspectives of the reconstructed porosity within the microstructure.

#### 4. Conclusion

A 61Ta:39C specimen was fabricated by VPS processing with subsequent sintering and HIP operations to consolidate the material. The initial powders were carbon-rich TaC to help off-set carbon loss from the VPS process. The initial powder revealed a low concentration of oxygen impurities that is suspected to contribute to the formation of oxide inclusions in the tantalum carbide. These inclusions were of insufficient volume to XRD diffract their phase in the diffractogram. SEM and TEM micrographs and EDS spectral maps revealed that these inclusions were on the grain boundaries and within the matrix phase. The morphology of the oxide inclusions along the grain boundaries were interconnected, which was clearly evident from the 3D reconstructions. The oxide phases were identified by SEAD to be tantalum (II) oxide, TaO, and tantalum pentoxide,  $\beta$ -Ta<sub>2</sub>O<sub>5</sub>. EDS line profiles also provided complimentary compositional verification of these phases. Finally, the 3D reconstruction provided quantification of the porosity size distribution and location in the microstructure. For the finite volume analyzed, the greater part of the pores was observed in the grains as compared to the boundaries. The distribution of the pores showed that the majority of pores had a volume less than 0.04  $\mu\text{m}^3$ .

#### 5. Acknowledgement

This research has been supported by the Army Research Office under grant W911NF-08-1-0300, Dr. David Stepp program manager.

#### 6. References

- [1] K. Balani, G. Gonzalez, A. Agarwal, R. Hickman, and J. S. O'Dell, "Synthesis, Microstructural Characterization, and Mechanical Property Evaluation of Vacuum Plasma Sprayed Tantalum Carbide," *J. Am. Ceram. Soc.*, **89**(4)(2006) 1419-1425
- [2] K. Upadhyay, J. M. Yang, and W. P. Hoffman, "Materials for Ultrahigh Temperature

- Structural Applications," *Am. Ceram. Soc. Bull.*, **76**(12)(1997) 51-56
- [3] C. R. Wang, J. M. Yang, and W. Hoffman, "Thermal stability of refractory carbide/boride composites," *Mater. Chem. Phys.*, **74**(3)(2002) 272-281
- [4] R. A. Morris, D. Butts, and G. Thompson, "TaXC1-X Phases and Microstructures Processed by Vacuum Plasma Spraying ," *J.Am. Ceram. Soc.*, **In press**(2010)
- [5] R. Morris, D. Butts, S. DiPietro, A. Craven, L. Matson, and G. Thompson, "Comparison between HIP and VPS tantalum carbides microstructure morphologies," in *SAMPE 2009 Technical Conference Proceedings*, Baltimore, MD, May 18-21, 2009, pp. 1-10.
- [6] C.K Jun and P.T.B Shaffer, "Elastic moduli of niobium carbide and tantalum carbide at high temperature ," *Journal of less common materials*, **23**(4)(1971) 367-373
- [7] E.L. Courtright, J.T. Prater, G.R. Holcomb, G.R. St. Pierre, and R.A. Rapp, "Oxidation of hafnium carbide and hafnium carbide with additions of tantalum and praseodymium ," *Oxid. Met.* , **36**(5-6)(1991) 423-437
- [8] P. Helisto, A.S. Helle, and J. Pietikainen, "Interface phenomena between oxide layers and cemented carbide tools," *Wear*, **139**(2)(1990) 225-234
- [9] H. Bispinck, O. Ganschow, L. Wiedmann, and A. Benninghoven, "Combined SIMS, AES, and XPS investigations of tantalum oxide layers," *Applied Physics A: Materials Science & Processing*, **18**(2)(1979) 113-117
- [10] R. S. Roth, J. L. Waring, and H. S. Parker, "Effect of oxide additions on the polymorphism of tantalum pentoxide. IV. The system Ta<sub>2</sub>O<sub>5</sub>---Ta<sub>2</sub>WO<sub>8</sub>," *Journal of Solid State Chemistry*, **2**(3)(1970) 445-461
- [11] E.I. Golovko, L.F. Ochkas, M.S. Koval'chenko, and A.F. Nikityuk, "Oxidation of tantalum carbide alloys," *Powder Metallurgy and Metal Ceramics*, **15**(10)(1976) 777-780
- [12] M. Desmaison-Brut, N. Alexandre, and J. Desmaison, "Comparison of the Oxidation Behavior of Two Dense Hot Isostatically Pressed Tantalum carbide (TaC and Ta<sub>2</sub>C) Materials," *Journal of the European Ceramic Society*, **17**(1997) 1326-1334
- [13] S.A. Kuznetsov, V.V. Grinevich, A.V. Arakneeva, and V.T. Kalinnikov, "Electrochemical Synthesis of Tantalum Monoxide Nanoneedles in Molten Salts," *Doklady Chemistry*, **428**(2)(2009) 199-202
- [14] Kirk-Othmer, *Kirk-Othmer Concise Encyclopedia of Chemical Technology*, 5th ed.: John

Wiley & Sons, Inc., 2007.

- [15] N. Schonberg, "An X-Ray Investigation of the Tantalum-Oxygen System," *Acta Chem. Scand*, **8**(1954) 240
- [16] T. Kim and M. S. Wooldrich, "Catalytically Assisted Self-Propagating High-Temperature Synthesis of Tantalum Carbide Powders," *J. Am. Ceram. Soc.*, **84**(5)(2001) 976-982
- [17] B. Schulz, B. Wang, D. Butts, and G. Thompson, "Influence of Hafnium on the Microstructures in Tantalum Carbides," *Scripta Met.*, **in press**(2010)
- [18] R. M. German and S. J. Park, *Mathematical relations in particulate materials processing: ceramics, powder metals, cermets, carbides, hard materials and minerals.*: John Wiley & Sons. Inc., 2008.
- [19] H. O. Pierson, *Handbook of Refractory Carbides and Nitrides*. Westwood, New Jersey: Noyes Publications, 1996.
- [20] M. D. Uchic, M. A. Groeber, D. M. Dimiduk, and J. P. Simmons, "3D Microstructural Characterization of Nickel Superalloys via Serial-Sectioning Using a Dual Beam FIB-SEM," *Scripta Materialia*, **55**(206) 23-28
- [21] R. W. G. Wyckoff, *Crystal Structures I*, 2nd ed. New York: Interscience Publishers, 1963.
- [22] F. Lissner and T. Schleid, "Redetermination of the Crystal Structure of di-Tantalum monocarbide, Ta<sub>2</sub>C," *Z. Kristallogr. NCS*, **216**(6)(2001) 329
- [23] A. I. Gusev, A. S. Kurlov, and V. N. Lipatnikov, "Atomic and Vacancy ordering in carbide z-Ta<sub>4</sub>C<sub>3-x</sub> and Phase equilibria in the Ta-C system," *J. Solid State Chem.*, **180**(2007) 3234-3246
- [24] J. M. Cowley, *Diffraction Physics*, 3rd ed. Amsterdam, The Netherlands: Elsevier Science B. V., 1995.
- [25] I. P. Zibrov, V. P. Filonko, M. Sundberg, and P. E. Werner, "Structures and phase transitions of (b)Ta<sub>2</sub>O<sub>5</sub> and (z)Ta<sub>2</sub>O<sub>5</sub>: two high-pressure forms of Ta<sub>2</sub>O<sub>5</sub>," *Acta Crystallogr., Sect. B: Struct. Sci.*, **59**(2000) 659-665
- [26] J. Goldstein, D. Newbury, D. Joy, P. Echlin, E. Lifshin, L. Sawyer, and J. Michael, *Scanning Electron Microscopy and X-Ray Microanalysis*, 3rd ed. New York, USA: Springer, 2003.

- [27] D. C. Joy, *Monte Carlo Modeling for Electron Microscopy and Microanalysis*. New York: Oxford University Press, 1995.
- [28] D. B. Williams and C. B. Carter, *Transmission electron microscopy: a textbook for materials science*. New York, N.Y.: Springer Science, 1996.
- [29] D. J. Rowcliffe, "Structure of Non-Stoichiometric TaC," *Mater. Sci. Eng.*, **18**(1975) 231-238
- [30] E. K. Storms, "The Tantalum-Tantalum Carbide System," in *The Refractory Carbides*.: Academic Press, 1967.

## CHAPTER 5

### THERMO-MECHANICAL TESTING OF TANTALUM CARBIDES USING A LORENTZ-FORCE, NON-CONTACT TECHNIQUE<sup>4</sup>

#### Abstract

A thermo-mechanical testing apparatus has been constructed where an electrical current provides resistive heating and, in the presence of a magnetic field, provides a Lorentz force for the application of a load on a test bar specimen. The electromagnetic Helmholtz coil can be used to independently control the magnetic flux, or load, while adjusting the specimen current for resistive heating of the specimen. The coils and specimen were encased in a stainless steel chamber that controlled the testing environment. The apparatus successfully deformed test bars of  $\gamma$ -TaC at 2600 °C and 3100 °C for 30 minutes. The temperature and deflection measurements were simulated using a finite element model. During the thermo-mechanical testing, the equiaxed grains grew isotropic with the intrinsic porosity, observed in pre-tested grain boundaries, providing microstructural markers of the grains initial size, shape and location in the microstructure.

---

<sup>4</sup> A manuscript has been prepared for the work in this chapter for the publication in the Journal of Instruments and Experimental Techniques as : R.A. Morris and G.B. Thompson, “Thermo-Mechanical Testing of Tantalum Carbides using a Lorentz-Force, Non-Contact Technique.”

## 1. Introduction

For ultrahigh temperature ceramics (UHTC), quantifying the thermo-mechanical properties can be challenging because of the inability to access temperature regimes where intrinsic deformation modes are initiated [1,2,3,4]. Since bulk lattice diffusion, which can have a dramatic effect on mechanical responses, initiates at approximately one-half or higher the melting temperature,  $T_m$ , the ability to probe temperatures  $> 2000$  °C for UHTC is crucial. These testing limitations are usually because of inadequate heating capability, compliance in the testing rig at these temperatures, and/or chemical reactions between the testing specimens and testing fixtures or the environment [5].

$\gamma$ -TaC has a melting temperature near 4000 °C and is the highest melting temperature known [6]. Additionally,  $\gamma$ -TaC exhibits a brittle-to-ductile behavior at temperatures  $> 1500$  °C [4]. Most traditional ‘at-temperature’ testing rigs, such as four point bending units encased in graphite filament furnaces, provide maximum testing temperatures that approach 1800 °C – 2000 °C. In particular to  $\gamma$ -TaC, exceeding the 2000 °C temperature threshold would allow investigation into its creep performance, the activation of potentially new dislocation activity, such as thermally activated cross-slip, and dislocation climb. Arguably, there are no systematic means to provide quantitative loading for UHTC at temperatures greater than 2000 °C. To fully exploit tantalum carbides for thermo-structural loading applications in extreme temperatures, the ability to quantitatively probe higher temperatures is required.

Karlsdottir and Halloran reported the use of electrical current to provide rapid heating of ceramic materials [7]. Tantalum carbides exhibit reasonable electrical conduction [8] providing the ability to resistively heat the material without excessive voltages needed to pass the current. Also, the ability to regulate the current intrinsically controls the temperature of the specimen

making it independent of the need for any external heating source. Thus, the specimen's own conductivity provides the independent means to heat itself. This is advantageous as now temperatures that were beyond the temperature limitations of graphite or tungsten filament furnaces can be accessed.

Building upon the design of Karlsdottir and Halloran [7], Gangireddy *et al.* [9] constructed an ingenious 'electro-magnetic mechanical apparatus.' In this unit, they took advantage of the fact that a current carrying electrical conductor in the presence of a magnetic field experiences a Lorentz force [10] given as:

$$\mathbf{F} = L\mathbf{I} \times \mathbf{B} \quad (1)$$

where the resultant force,  $\mathbf{F}$ , is proportional to the cross product of the length of the conductor,  $L$ , the current,  $\mathbf{I}$ , and the magnetic field vector,  $\mathbf{B}$ . Depending on the current's magnitude and/or the specimen size, the specimen itself can experience significant plastic deformation under the Lorentz force. Gangireddy *et al.* [9] successfully demonstrated the thermo-mechanical deformation of a  $\text{ZrB}_2\text{-SiC}$  composite using this apparatus. Though successful, the testing rig constructed by Gangireddy *et al.* [9] had several limitations. This included the oxidation of the specimen during testing and the inability to independently control load and temperature since the magnetic flux was fixed by the permanent magnets, making both the temperature and force dependent on the current. Oxidation and similar types of phase transformations during a test should be avoided. These phase transformations alter the intrinsic mechanical response in the material making the data collected convoluted.

In this paper, we provide modifications to the original Gangireddy *et al.* [9] apparatus design to test materials that are prone to oxidation, as well as independently control the

temperature and load during the test. The material to be tested,  $\gamma$ -TaC, arguably represents the ultimate material because of its extreme melting temperature and it readily oxidizes and (de)carburizes depending on the environment [11].

## 2. Modifications to the Lorentz-force, non-contact apparatus

As described in the introduction, a modified testing apparatus or rig was constructed based on Gangireddy *et al*'s. [9] Electro-Magnetic Mechanical Apparatus design, shown in figure 1. Our testing rig is built around two main components: (1) a current source to provide resistive heating of the specimen, similar to Gangireddy *et al*'s [9] and (2) a Helmholtz electromagnet coil design that provides adjustable magnetic flux by regulating the current in the coils. The advantage of the Helmholtz coils is the ability to change the applied force during the test by simply changing the current. The field strength can also be tailored by adjusting the air gap between the two magnetic poles. This was easily accomplished using an adjustable mounting screw to our electromagnetic coils.

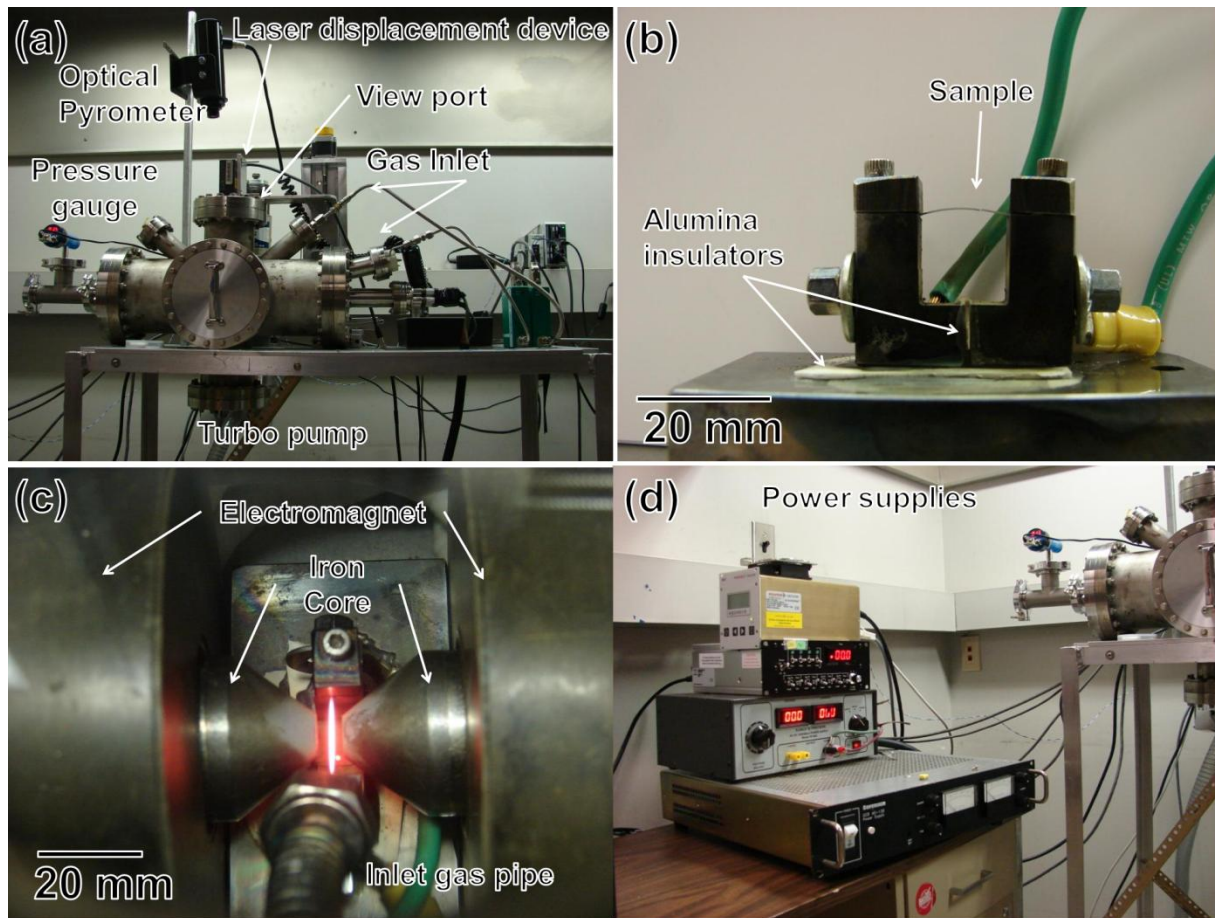


**Figure 1:** (a) Image of the thermo-mechanical testing rig with the components labeled (b) Clamp-type mount for holding the test bar between the electromagnets. The specimen shown is post thermo-mechanical loading; the initial specimen was flat. (c) Test bar during heating experiment with the electromagnet and conical iron cores and gas inlet above the specimen. (d) Electronics and related machinery.

To increase the field strength between the coils, either the number of ‘turns’ has to be increased [12] or an insert iron core can be placed at the center of the coils on either side. This former option would increase the size of the electromagnetic coils, which could be a disadvantage with limited instrumentation space. We found that the iron core was more suitable for our applications. The ferromagnetic property of the iron core causes the internal magnetic domains of the iron to line up with the smaller driving magnetic field produced by the current in the electromagnet. The effect is the multiplication of the magnetic field by factors of tens to even

thousands [13]. For our experimental conditions, the maximum magnetic flux density for our coils and iron core was measured at 0.75 T using a hand-held Gauss meter at an air gap of 4 mm.

Comparable to Gangireddy *et al*'s [9] unit, a DC current power supply was used to provide resistant heating of the specimen. The current and voltage supplied to the specimen was measured using a combined voltmeter and ammeter. Typical specimen geometries consisted of a rectangular bar that was 2 cm in length with a square cross-sectional width of 250  $\mu\text{m}$ . These specimens were electro-discharge machined into the appropriate sizes. Though a larger amount of material at each end of the bar can be advantageous in terms of reducing the gauge length size to be the narrowest in the middle of the bar as well as ensuring that the smaller cross-sectional area in the gauge length is resistively hotter than the ends, we did not observe any issues, as described in detail below, using a straight bar approach.

The conductive fixture to hold the specimen bar, shown in figure 1(b), was made out of stainless steel sheets that were clamped into position by a screw mount. The stainless steel block was advantageous because it was nonmagnetic and can withstand high temperatures. The massive block also acted as an excellent heat sink for the tantalum carbide specimen wire which confined the heat to the bar specimen. Electrical insulating alumina plates were placed between the two block clamps and the specimen mounting plate which allowed easy placement and retraction of the sample from the coils. Figure 1(c) shows a tantalum carbide specimen at an elevated temperature during a test.

In an attempt to alleviate the potential oxidation of a specimen during heating as well as control the environment the specimen was tested in, the coils and mounting unit were placed inside a stainless steel chamber that could be evacuated using a turbo pump backed by a

mechanical roughing pump, figure 1(a). The chamber is able to reach pressures  $< 1 \times 10^{-4}$  Pa. A Raytek Marathon ® series optical pyrometer could monitor the temperature *in situ* through a glass port window that provided a top-down view of the specimen. Unlike the Gangireddy *et al*'s [9] unit, which determined the relative displacement of the specimen post-testing, the modified version includes a Keyence LK-G series® laser displacement sensor, at a wavelength 680 nm, which can monitor, *in situ*, the relative movement of the bar's bend. An optical filter was necessary to be placed onto the sensor to clearly distinguish the laser reflection from the white light emitted from the specimen during heating. Gas inlet lines were attached to the chamber which can flow various working gasses into and over the test bar. Though a general background pressure could be applied, it was found that a snorkel inlet, figure 1(c), of the gas to flow directly over the specimen was more effective in improving the specimen-working gas reactions, as will be discussed in detail below.

The temperature of the specimen was determined using the output of the optical pyrometer and verified using Joules first law of resistive heating. The power, P, dissipated is given as:

$$P = \frac{V^2}{R} = V \cdot I \quad (2)$$

where V is voltage, R is resistivity ( $\sim 2 \times 10^6 \Omega\text{m}$  for TaC [8,14]), and I is current. Assuming a low pressure environment where radiant heat dominates, as is the case for enclosing our specimen in the modified vacuum chamber, the power dissipation is given by the Stefan–Boltzmann law [15] as:

$$P = \epsilon \cdot \sigma \cdot A \cdot T^4 \quad (3)$$

where  $\epsilon$  is the emissivity ( $\sim 0.4$  for TaC [16]),  $\sigma$  is the Stefan-Boltzmann constant,  $A$  is the surface area and  $T$  is temperature, in Kelvin. Combining equation (2) and (3), the temperature can readily be determined from the measurable currents and voltages as:

$$T = \sqrt[4]{\frac{V \cdot I}{\epsilon \cdot \sigma \cdot A}} \quad (4)$$

For specimen geometries studied and applied currents greater than 10 A, the tantalum carbide specimens melted demonstrating the range in temperatures capable to be tested in this unit for this material system.

Displacement measurements of the deformed test bars can be performed *in situ* using the laser displacement sensor or measuring the plastic deformation in the post-tested bar. Under the applied load from the Lorenz force, the test bar behaves as a beam of length  $L$  with fixed ends as illustrated in figure 2(a). The relation of the maximum flexure stress,  $\sigma_{max}$ , to the current, magnetic flux, and specimen dimensions is given [9] as:

$$\sigma_{z,max} = 0.25 \frac{L^2}{Yt^2} I_x B_y \quad (5)$$

where  $Y$  and  $t$  are the cross-sectional dimensions of the test bar, and  $B$  is the magnetic flux.

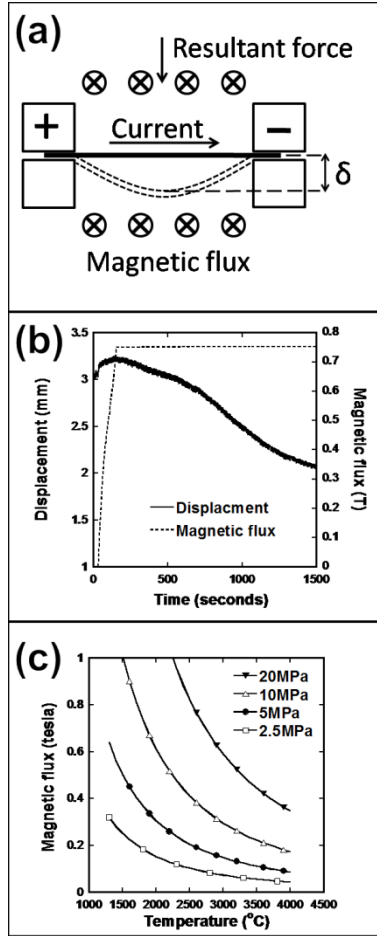


**Figure 2:** (a) Illustration of the Lorentz force applied to a current carrying conductor in the presence of a magnetic field. (b) Plot of real-time displacement and magnetic flux for a TaC sample held at 2000 °C. (c) Iso-loading contour plot showing temperature-magnetic flux relationships to provide a constant stress.

As mentioned previously, the laser interferometer can allow the deformation response to be viewed in real time. Figure 2(b) shows an experimental *in situ* displacement plot of a TaC test bar at 2000 °C at a constant magnetic field (load) for a period of time, i.e. a creep experiment. Excluding the first tens of seconds, where the specimen was heating up to temperature and the slope change is a result of thermal expansion, the variation in slopes from ~ 100 seconds and longer mimic the classical shapes for different modes of steady-state creep, as commonly reported in a variety of material systems [17].

While the temperature is directly related to the current in the specimen, given above, the applied force can be adjusted by varying the magnetic flux using the variable power supply that controls the electromagnet. This enables the same load to be applied to the specimen at different temperatures. A series of iso-loading curves are shown in figure 2(c).

### 3. Results and Discussion

#### *3.1 Microstructural and phase content control during thermo-mechanical testing*

Tantalum carbide can readily oxidize to  $Ta_2O_5$  at temperatures above  $500^\circ C$  forming a laminated, non-protective oxide scale [11]. Initial experiments were performed, at atmosphere, to determine the extent and microstructure transitions that would accompany tantalum oxidation under various applied currents for temperatures  $1000^\circ C$  for times of 1 to 30 seconds. As shown in figure 3(a), the  $Ta_xC_{1-x}$  outer surface converted to  $Ta_2O_5$  and grew orthogonally to the bar surface. The experimental details of fabrication and X-ray Diffraction for phase identification of the tantalum carbides can be found elsewhere [18]. Upon extended time, the entire bar converted to the pentaoxide phase. Clearly, this phase and microstructure transition is not ideal for thermo-mechanical testing of this material.

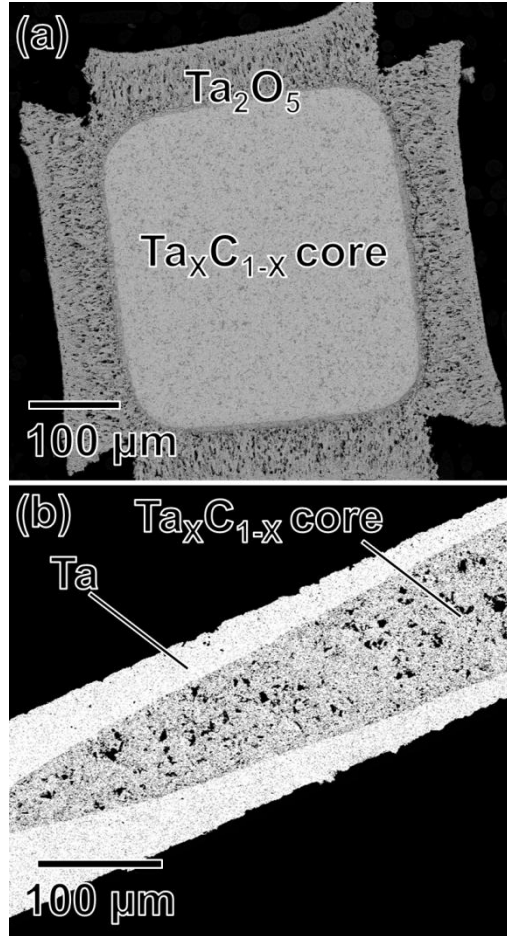


**Figure 3:** (a) Oxide scale after heating  $Ta_xC_{1-x}$  in atmosphere. (b) Surface tantalum layer that was transformed from the  $Ta_xC_{1-x}$  bar by de-carburization at elevated temperature in Ar environment.

Subsequently, the specimen was tested in the enclosed chamber design. The chamber was evacuated  $< 1 \times 10^{-4}$  Pa and backfilled to  $\sim 0.1$  Pa with ultrahigh purity Ar. While this eliminated the oxidation of the tantalum carbides, the decarburization of specimen occurred evident by the Ta surface layer, figure 3(b). Figure 3(b) shows a transformed Ta outer layer with a core of untransformed  $Ta_xC_{1-x}$  after heating the specimen to  $2600^\circ C$  for 30 minutes. The variation in the Ta conversion is a result of a temperature gradient within the specimen bar as the ends of the bar are closer to the heat sink mounts, which has been modeled below. The thicker Ta region, in figure 3(b), was near the middle section of the bar and would be the hottest region

during testing. This clearly indicates a temperature dependence on the rate of de-carburization in the surrounding environment. Though the enclosed vacuum environment removed the oxidation issue, even in the presence of an inert background gas, an undesired phase transformation in the carbide material occurred.

Similar to experiments where methane is flowed over a tantalum wire to carbonize it [8], a comparable experiment has been performed to reduce the decarburization in the tantalum carbide. A stream of methane was flowed to yield a chamber pressure of 0.3 to 4.4 Pa, after the chamber was evacuated. The cross-sectional surface thickness of transformed material was then measured using scanning electron microscopy (SEM) micrographs and plotted as a function of chamber pressure in figure 4(a). At 0.66 Pa, the tantalum carbide showed no to little change in the surface phase content. Figures 4 (b-f) shows the resultant microstructures after heating for 30 minutes at 2600°C using different working pressures of methane. Since the initial  $Ta_xC_{1-x}$  starting material, where  $X=0.5-0.66$ , was a mixture of TaC and  $Ta_2C$ , the conversion of the outer surface to single phase TaC, indicated by the electron backscattering diffraction phase map in figure 4(e), was indicative of a too rich-carbon environment. An exaggerated amount of methane in the system, as is the case for the 4.4 Pa pressure, caused well over 50% of the material to transform to single phase TaC, figure 4(f).

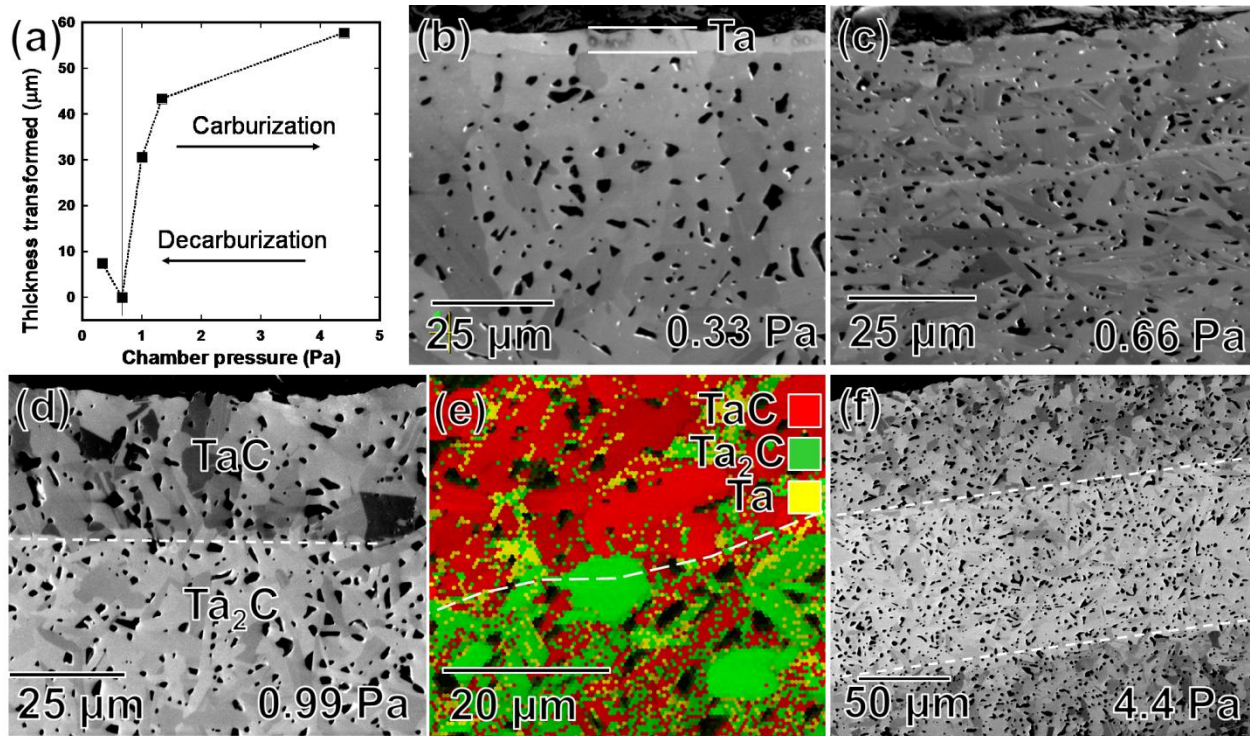


**Figure 4:** (a) Plot of the carburization and decarburization of  $\text{Ta}_x\text{C}_{1-x}$  at 2600 °C after 30 minutes at various methane chamber pressures. (b) Decarburization of  $\text{Ta}_x\text{C}_{1-x}$  to tantalum at a working pressure of 0.33 Pa of  $\text{CH}_4$ . (c) Micrograph showing no visible transformation at 0.66 Pa of  $\text{CH}_4$ . (d) Carburization of  $\text{Ta}_x\text{C}_{1-x}$  to TaC at a working pressure of 0.99 Pa of  $\text{CH}_4$ . (e) EBSD phase map of (d) showing the carburized TaC layer that formed. (f) Micrograph of transformed TaC layer in a highly carburizing environment of 4.4 Pa of  $\text{CH}_4$ .

### 3.2 Deformation responses in tantalum carbides using the Lorentz-force

With the microstructure stable under elevated temperature annealing, the thermo-mechanical response under the Lorentz force has been investigated for single phase  $\gamma$ -TaC. Two specimens at 2600°C (specimen #1) and 3100°C (specimen #2) were experimentally tested at a maximum magnetic field of 0.75 T for 30 minutes where the methane stabilized the phase in the test bar. Table 1 shows the corresponding data for each experiment.

**Table 1:** Table of the various experimental parameters for the as-cut specimens and the deformed specimens #1 and #2.

Sample #	Temperature (°C)	Deflection (mm)	Current (A)	Mag. Field (T)	Force/area (MPa)	Grain size (μm)
As-cut	-	-	-	-	-	15 +/- 5
1	2600 +/- 20	0.33	6.9	0.75	16	48 +/- 11
2	3100 +/- 20	0.84	9.0	0.75	21	111 +/- 28

A finite element model, using the COMSOL® platform, has been employed to determine the magnetic flux profile of the applied magnetic field, the temperature profile across the specimen bar, and the deformation response of the bar under the applied magnetic field (or Lorentz force) are tabulated in Table 1.

The magnetic flux of the electromagnet was measured using a Gauss meter at a gap 4 mm and 8.5 mm. The magnetic flux density is given as

$$A_z = J_z^e \mu_0 \mu_r \quad (6)$$

where  $A_z$  is the magnetic potential,  $J_z^e$  is the external current density in the magnet,  $\mu_0$  permeability in a vacuum, and  $\mu_r$  relative permeability. The resulting contour profile is shown in figure 5(a) and the field line profile is plotted in figure 5(b). These plots clearly reveal that the specimen will experience a gradient force across the bar that will follow the profile of the field lines whose peak field is dependent upon the gap between the coils.

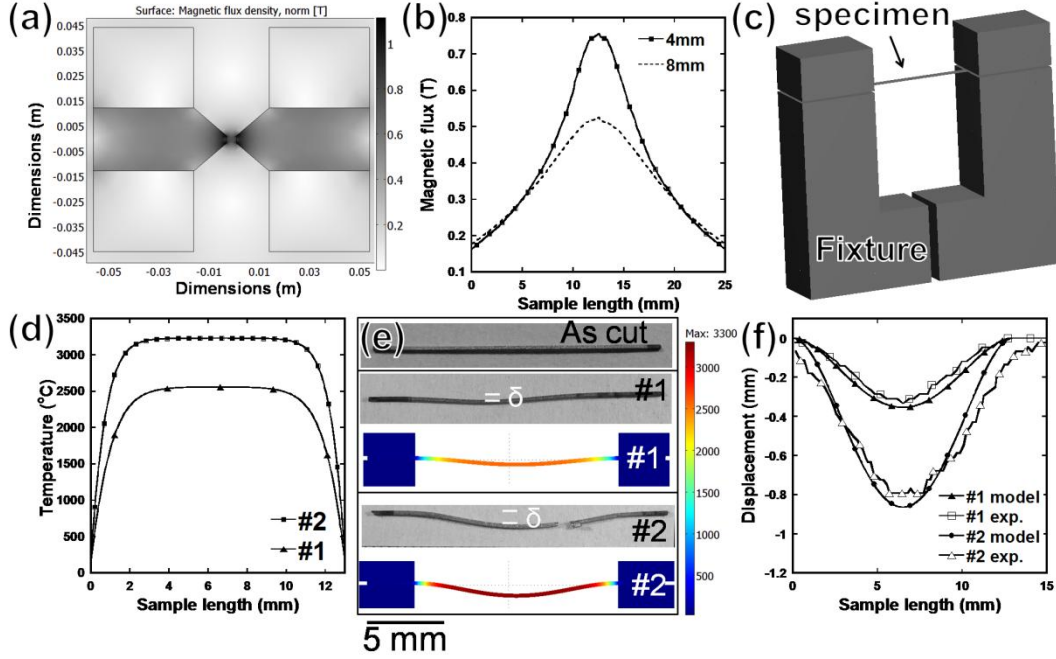


**Figure 5:** (a) Surface plot of the simulated magnetic flux density of the electromagnet with an iron core. (b) Plot of the simulated magnetic flux across the test bar length for two different iron core air gaps of 4 mm and 8 mm. (c) 3D model of the clamp fixture and specimen used for the modeling of the thermo-mechanical testing rig. (d) Plot of the simulated specimen temperature. (e) Images of the as-cut sample and deformed specimens #1 and #2 with the simulated deformed specimen overlaid with the temperature profile. (f) Plot of the experimental and simulated displacements across the length of the deformed specimens.

The testing mount used in the simulation is shown in figure 5(c) to model the resistive heating and the specimen displacement because of the Lorentz force. The temperature profile across the bar has been calculated, based on the experimental parameters applied to be shown below, using equation (4) and the 2-dimensional heat flow equations:

$$\nabla \cdot (-k\nabla T) = Q \quad (7)$$

$$-\nabla \cdot \left( \frac{\nabla V - J^e}{\rho_o(1+\alpha(T-T_o))} \right) = Q_j \quad (8)$$

where  $k$  is the thermal conductivity,  $Q$  is the heat source,  $V$  is applied voltage,  $J^e$  is the external current density,  $\rho_o$  is the electrical resistivity,  $\alpha$  is the temperature coefficient,  $T_o$  is the

reference temperature, and  $Q_j$  is the current source. The temperature coefficient for electrical resistivity of TaC was taken from the work by Cooper *et al.* [8] and Grebenkina *et al.* [14] The simulation takes into account the conductive heat transfer through the stainless steel fixtures and radiant heat from the specimen into the surrounding environment. The profile, figure 5(d), indicates that the temperature across the bar is uniform over approximately 80% of the length. As expected, a decrease in temperature occurs approximately 2 mm from the contact points of the specimen to the heat sink fixture. This was seen in the previous temperature dependant carbonization experiments above, figure 3(b).

Finally, the deflection of the specimen, as a function of Lorentz force, equation (1), magnetic flux line profile, figure 5(b), and bending behavior, equation (5), was calculated for the applied currents that generated the temperatures shown in figure 5(d). The TaC's Young's modulus was taken from Jun and Shaffer [19] and the thermal expansion from Chiao and Lin [20]. The experimental and simulated deflection of the TaC bar is shown in figure 5(e). The simulated deformation bend is overlaid with the temperature profile. As expected, specimen #2, which experienced a higher current therefore a higher temperature and higher force, exhibited a greater amount of deflection. The simulated and experimental deflection as a function of length is plotted in figure 5(f). The simulated deformation is in good agreement with the experimental determined deflection. The experimental deflection amounts were measured by taking an optical image of the post-tested bar in cross-section and placing the image in Nikon's ELEMENTS software where the pixels were converted into unit lengths and the displacement normal to a linear line drawn from the two unbent ends of the bar (initial condition).

### *3.3 Microstructure evolution under thermo-mechanical loading*

The hot isostatic pressed (HIP) single phase  $\gamma$ -TaC microstructures exhibited an equiaxed grain size of  $15 \pm 5 \mu\text{m}$ , figure 6(a) and (b). The experimental details of its fabrication can be found elsewhere [18]. The higher magnification SEM micrograph of figure 6(b) reveals porosity between the grains which is typical for powder metallurgy HIP processing [21]. After the thermo-mechanical loading at 2600 °C and 3100 °C for 30 minutes, the microstructure of the two specimens were re-examined and representative micrographs are shown in figure 6(c) and (d). The grain size increased to  $48 \pm 11 \mu\text{m}$  and  $111 \pm 28 \mu\text{m}$  for 2600 °C and 3100 °C, respectively. Interestingly, the initial porosity locations appeared to remain fixed in the microstructure while the grains coarsened as evident by the pores now encased within the grains themselves. Clearly, the higher temperature anneals resulted in significant grain growth during the thermo-mechanical loading. The lack of clear deformation bands within the microstructure is suspected to be a result of dynamic recovery within the microstructure that accompanied the elevated temperature deformation as similarly seen in hot worked materials [22] and is the subject of future work.

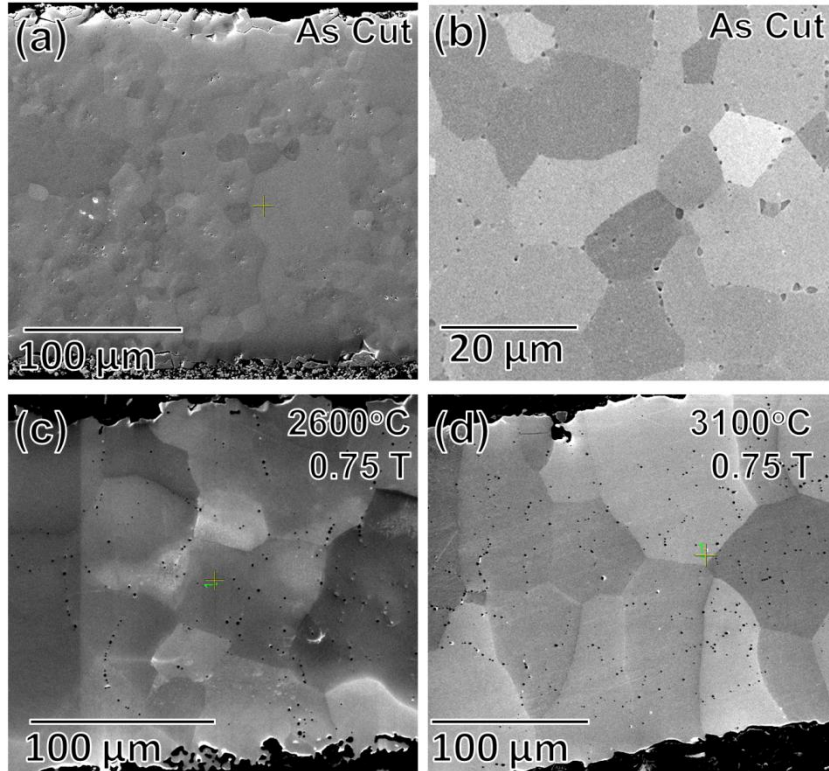


**Figure 6:** (a-b) SEM micrographs of the as-cut microstructure showing equiaxed grains with the porosity located at the grain boundaries. (c) Post heating of specimen #1 microstructure. (d) Post heating of specimen of #2 microstructure

#### 4. Summary

A thermo-mechanical testing apparatus, based upon the design of Gangireddy *et al.* [9], has been modified to allow independent control of the load and temperature through the use of an electromagnetic Helmholtz coil design. Additionally, the system was housed in a stainless steel chamber to control the environment during testing and has both *in situ* pyrometer and laser interferometer attachments for real time evaluation of temperature and deflection. The temperature and deflection measurements were also simulated using a finite element code. The modified thermo-mechanical testing apparatus was used to test the deflection of tantalum carbide. The oxidation and (de)carburization of the sample was prevented by evacuating the chamber and flowing in a methane stream over the specimen while at temperature. During loading for 30 minutes at 2600°C and 3100°C, the single phase TaC equiaxed grains experienced significant coarsening. The retained porosity, initially at the grain boundaries, did not appear to migrate or reduce in size providing intrinsic markers of the initial grain size, shape and location in the microstructure.

#### 5. Acknowledgements:

The authors thank Nicholas De Leon, Joel Sadoris and Anna Williams for assistance during this project. This work was primarily supported under the MDA contract HQ0006-08-C-7663 with supplementary support from the Army Research Office under grant W911NF-08-1-0300.

#### 6. References

- [1] M. C. Teague, G. E. Hilmas, and W. G. Fahrenholtz, "Mechanical properties of reactively processed W/Ta<sub>2</sub>C-based composites," *J. Euro. Ceram. Soc.*, **30**(11)(2010) 2197-2201

- [2] L. Limeng, Y. Feng, and Z. Yu, "Microstructure and Mechanical Properties of Spark Plasma Sintered TaC<sub>0.7</sub> Ceramics," *J. Am. Ceram. Soc.*, **In press**(2010)
- [3] R. E. Pawel and J. J. Campbell, "The influence of alloying elements on oxygen diffusion and flexure in tantalum base alloys," *Acta Metall.*, **29**(5)(1981) 809-817
- [4] C. Kim, G. Gottstein, and D. S. Grummon, "Plastic Flow and Dislocation Structures in Tantalum Carbide: Deformation at Low and Intermediate Homologous Temperatures," *Acta Metall. Mater.*, **42**(7)(1994) 2291-2301
- [5] X. Zhang, G. E. Hilmas, and W. G. Farenholtz, "Densification, Mechanical Properties, and Oxidation Resistance of TaC–TaB<sub>2</sub> Ceramics," *J. Am. Ceram. Soc.*, **91**(12)(2008) 4129-4132
- [6] E. K. Storms, "The Tantalum-Tantalum Carbide System," in *The Refractory Carbides.*: Academic Press, 1967.
- [7] S. N. Karlsdottir and J. W. Halloran, "Rapid characterization of ultra-high temperature ceramics," *J. Am. Ceram. Soc.*, **90**(2007) 3233-3238
- [8] J. R. Cooper and R. L. Hansler, "Variation of electrical resistivity of cubic tantalum carbide with composition," *J. Chem. Phys.*, **39**(248)(1963)
- [9] S. Gangireddy, J. W. Halloran, and W. N. Zachary, "Non-contact mechanical property measurements at ultrahigh temperatures," *J. Eur. Ceram. Soc.*, **30**(2010) 2183-2189
- [10] J. D. Jackson, *Classical electrodynamics*, 3rd ed. Ney York, N.Y.: Wiley, 1999.
- [11] J. Stringer, "Oxidation in Tantalum in Oxygen-Nitrogen and Oxygen-Inert Gas Mixtures," *Oxid. Met.*, **11**(5)(1977) 255
- [12] D. Halliday, R. Resnick, and J. Walker, *Fundamentals of Physics*, 6th ed.: Wiley, 2000.
- [13] A. Fitzgerald, C. Kingsley, and A. Kusko, *Electric Machinery*, 3rd ed. USA: McGraw-Hill, 1971.
- [14] V. G. Grebenkina and E. N. Denbnovetskaya, "Temperature coefficient of electrical resistivity of some complex carbides," *Powder Metall. Met. Ceram.*, **7**(3)(1968) 187-188
- [15] H. A. Lorentz, *The thoery of electrons and its applications to the phenomena of light and radiant heat*, 2nd ed. New York, USA: G. E. Stechert company, 1916.

- [16] B. Eckstein and R. Forman, "Preparation and Some Properties of Tantalum Carbide," *J. App. Phy.*, **33**(1)(1962) 82-88
- [17] M. A. Meyers and K. K. Chawla, *Mechanical Behavior of Materials.*: Cambridge University Press, 1999.
- [18] R. A. Morris, B. Wang, and G. B. Thompson, "Microstructural Formations and Phase Transformation Pathways in HIP Tantalum Carbides," *to be submitted*
- [19] C.K. Jun and P.T.B. Shaffer, "Elastic moduli of niobium carbide and tantalum carbide at high temperature," *J. Less-Common Met.*, **23**(4)(1971) 367-373
- [20] M. Chiao and L. Lin, "Self-Buckling of micromachined Beams Under Resistive Heating," *J. Microelectromech. Syst.*, **9**(1)(2000) 146-151
- [21] R. M. German, *Powder Metallurgy and Particulate Processing*. Princeton, New Jersey: Metal Powder Industries Federation, 2005.
- [22] E. P. Degarmo, J. T. Black, and R. A. Kohser, *Materials and Processes in Manufacturing*, 9th ed.: Wiley, 2003.

## CHAPTER 6

### CONCLUSIONS AND FUTURE DIRECTIONS

#### 6.1 General Summary

A study of the microstructural effects on processing and carbon content was completed and addressed in Chapters 2-5. In Chapter 2, a series of  $Ta_XC_{1-X}$  specimens, where  $X = 51, 56, 58, 62, 65,$  and  $68$  at. %, were HIP processed from TaC and Ta powder mixtures to span the phase ranges of TaC, TaC + Ta<sub>2</sub>C (Ta<sub>4</sub>C<sub>3</sub>), and Ta<sub>2</sub>C. For the single phase compositions, the microstructure was equiaxed with the TaC grains being smaller than Ta<sub>2</sub>C. The grain size differences were explained in terms of the initial powder sizes. For composition between ~ 40 at.% C to ~ 44 at.% C (two-phase region between TaC and Ta<sub>4</sub>C<sub>3</sub>), the microstructure consisted of equiaxed TaC grains encasing fine laths of Ta<sub>4</sub>C<sub>3</sub> precipitated on multiple TaC {111} planes within each grain. This resulted in hatch-work pattern morphology. For compositions between ~ 34 at.% C to ~ 40 at.% C (ideally Ta<sub>4</sub>C<sub>3</sub> and Ta<sub>2</sub>C), the two phase mixture consisted of acicular grains with TaC, Ta<sub>4</sub>C<sub>3</sub> and Ta<sub>2</sub>C phases having their closed packed planes and closed packed directions all aligned and parallel to the major axis of the grain. This grain morphology is formed because of the low interfacial energy between the phases, preferential growth rate parallel to the closed packed planes and the sequence of precipitation. Using a TaC/Ta diffusion couple, it was observed that carbon is depleted from the TaC phase and reacts with the Ta to form Ta<sub>2</sub>C. Since *hcp* Ta<sub>2</sub>C has only one closed packed plane orientation, {0001}, per grain, the subsequent precipitation of TaC within these grains results in all the phases being parallel laths which drives the change in grain shape. These results clearly indicate that small variations in carbon content can have a dramatic effect on microstructure morphology and phase content. The sequence of precipitation of the initial matrix phase, either TaC or Ta<sub>2</sub>C, controls the overall

grain morphology because of the preferred orientation relationship of these phases with each other.

Chapter 3 was a study on the effects of VPS processing of tantalum carbide microstructures. A series of 53Ta:47C, 55Ta:45C, and 63Ta:37C specimens have been VPS, sintered and HIP'ed processed. In the 53Ta:47C VPS as-sprayed condition, a distribution of grain sizes and phases existed. Upon the subsequent sintering, the grain size became uniform and equiaxed. The post-VPS processing also homogenized the phase content to be single phase TaC. Upon fabricating specimens with less carbon content, the precipitation and stabilization of Ta<sub>4</sub>C<sub>3</sub> and Ta<sub>2</sub>C was secured. For the 55Ta:45C<sub>45</sub> specimen, an equiaxed grain structure with secondary phases of Ta<sub>4</sub>C<sub>3</sub> precipitated on multiple variants of {111}. These phases spanned and did not span the entire interior of the grain and formed a cross-hatch structure within the grains. The 63Ta:37C specimen exhibited an acicular grain morphology. The precipitation of Ta<sub>4</sub>C<sub>3</sub> and Ta<sub>2</sub>C was found to be parallel to the major-axis of the acicular grain with each grain consisting of a multiple stacking of these secondary phases. These phases also spanned the entire length of the major axis direction of the acicular grain. Based upon the low lattice misfit for the orientation relationship between these phases and TaC, these low interfacial energy planes dominate. Consequently this yields an anisotropic growth direction that changes the grain morphology from equiaxed to acicular with increasing volume fraction of the secondary phase content with TaC.

Chapter 4 was an extension of the VPS study if tantalum carbide, but focused on the formation of oxide inclusions and porosity within the microstructure. A 61Ta:39C specimen was fabricated by VPS processing using initial powder that was revealed to have a low concentration of oxygen which was suspected to contribute to the formation of oxide inclusions in the tantalum carbide. These oxide inclusions were of insufficient volume to XRD diffract there phase in the

diffractograms. SEM and TEM micrographs and EDS spectral maps revealed that these inclusions were on the grain boundaries and within the matrix phase. The morphology of the oxide inclusions along the grain boundaries were interconnected, which was clearly evident from the 3D reconstructions. The oxide phases were identified by SAED to be tantalum (II) oxide, TaO, and tantalum pentoxide,  $\beta$ -Ta<sub>2</sub>O<sub>5</sub>. EDS line profiles also provided complimentary compositional verification of these phases. Finally, the 3D reconstruction provided quantification of the porosity size distribution and location in the microstructure. For the finite volume analyzed, the greater part of the pores was observed in the grains as compared to the boundaries.

Finally in chapter 5, a thermo-mechanical testing apparatus, based upon the design of Gangireddy *et al.* [32], has been modified to allow independent control of the load and temperature through the use of an electromagnetic Helmholtz coil design. Additionally, the system was housed in a stainless steel chamber to control the environment during testing and has both *in situ* pyrometer and laser interferometer attachments for real time evaluation of temperature and deflection. The temperature and deflection measurements were also simulated using a finite element code. The modified thermo-mechanical testing apparatus was used to test the deflection of tantalum carbide. The oxidation and (de)carburization of the sample was prevented by evacuating the chamber and flowing in a methane stream over the specimen while at temperature. During loading for 30 minutes at 2600°C and 3100°C, the single phase TaC equiaxed grains experienced significant coarsening. The retained porosity, initially at the grain boundaries, did not appear to migrate or reduce in size providing intrinsic markers of the initial grain size, shape and location in the microstructure.

## 6.2 Linking Microstructure to Processing

This dissertation has investigated the relationship of processing on the resultant tantalum carbide microstructure. In general, the two different processes, HIP and VPS, followed different initial formation mechanisms; a solid state reaction between powders for HIP and a solidification of liquefied powders for VPS. Though the initial processing of VPS and HIP are different, the latter processing steps of VPS, i.e. sintering and HIP, makes the final microstructures similar. Though the initial powder in HIP and/or sprayed droplet sizes in VPS contained at least an order of magnitude difference in initial sizes, the final grain sizes of these microstructures appeared to trend with largest initial sized feature, whether that be the powder or the sprayed droplets. Clearly, to reduce the final grain size, one should reduce the initial sprayed droplet size or reaction powder size.

The porosity spatial location also appeared to be dependent on the processing route. It was found that the HIP process nominally developed porosity along the grain boundaries, while the VPS method had porosity throughout the microstructure. For the HIP process, the formation of porosity along the boundaries would occur because of incomplete volume filling as the powders sinter [33]. The high melting temperature of these materials would suggest limited diffusivity as compared to lower melting temperature elements. For the VPS process, the porosity was observed throughout the microstructure. Since the initial droplets are formed from the liquid, rapid cooling would result in porosity between the grains. The subsequent sintering and HIP though consolidates the droplets, surrounding the porosity, resulting in a distribution of porosity throughout the microstructure.

### 6.3 A Perspective on the Nucleation of Secondary Phases

A transformation model developed from chapters 2 and 3 of this dissertation, which is based on work by Rowcliffe [14], shows a possible transformation mechanism that involves a diffusion-shear mechanism to transform the  $Ta_2C$  or  $Ta_4C_3$  phases from the TaC phase. Future work would involve more detailed characterization and energy based calculations that determine these transformation mechanisms. In the proceeding paragraphs, the proposed mechanisms are described in details from which future simulation work could develop based on these simple descriptions. Rowcliffe [14] reported that the  $Ta_2C$  and  $Ta_4C_3$  phase precipitates out of the TaC matrix through a stacking fault mechanism. Each of these phases has a parallel close packed plane and close packed direction orientation relationship with TaC.  $\gamma$ -TaC is a B1 rock-salt structure which has face-centered-cubic (fcc) symmetry. It is commonly known that a Shockley partial dislocation of  $1/6\langle 211 \rangle$  passed on every other  $\{111\}$  fcc plane converts the structure to hcp. Since the B1 structure has two interpenetrating fcc lattices of Ta and C, the Shockley needs to be twice as long to give the correct symmetry displacement. This would result in a large energy penalty since dislocation energy scales with the burgers vector squared,  $b^2$  [14]. Consequently, Rowcliffe [14] suggested that a  $1/6\langle 211 \rangle$  Shockley is passed in opposite directions on parallel planes to generate the necessary displacement with the least energy penalty. Though this shift can give the correct fcc to hcp symmetry, Rowcliffe [14] did not discuss the compositional change necessary between TaC and  $Ta_2C$  or  $Ta_4C_3$ . To maintain the correct symmetry and composition, carbon atoms must be depleted on specific closed packed planes.

From the TEM analysis, the nucleation of the sub-carbide phases ( $Ta_2C$  and  $Ta_4C_3$ ) from the TaC phase was found to occur on the  $\{111\}$  planes of TaC. TEM micrographs in figure 1

(previously shown in figure 9 of chapter 2) revealed that there was a precipitation of these phases, in regular occurrence, formed plate like structures which initiated within the TaC grain. A possible mechanism is the formation of hcp from fcc materials by a Frank Loop method. In this mechanism, vacancies condense onto  $\{111\}$  planes and create a local intrinsic stacking fault of hcp material. In a similar manner, the condensation of vacancies on a  $\{111\}$  TaC plane would help assist in the diffusion of carbon away while creating this intrinsic stacking fault that can lead to the appropriate symmetry. The preferential migration of vacancies to one plane would result in a deficiency of vacancies on the planes above and below which could explain why lath bands form and not thicken for these secondary phase laths. The formation of these phases was clearly evident in the grains as seen in figure 1(b). Future work would look into the energetics of such a mechanism and simulate the data from the experimental TEM observations collected.

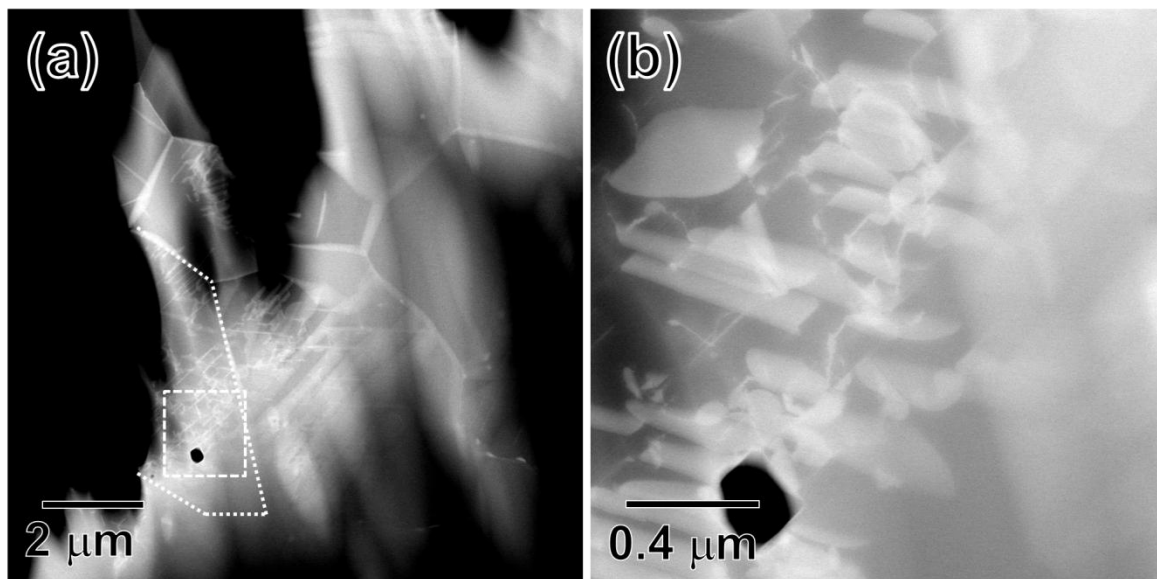


**Figure 1:** STEM-HAADF of TaC grain with the initial formations of sub-carbide phases. **(a)** Highlighted grain with inter lath structure within the grain. **(b)** Magnified area in (a) showing sub-carbide phases forming on different  $\{111\}$  TaC planes within the grain. (from Chapter 2)

The transformation mechanism described above is illustrated in figure 2. Figure 2 shows a schematic of the TaC structure, looking down a  $\langle 110 \rangle$  direction. The removal of  $\{111\}$  planes of carbon the highlighted in figure 2(a), yields the correct chemistry for Ta<sub>2</sub>C. To get the correct stacking order, two opposing  $1/6\langle 112 \rangle$  shears of adjacent Ta-C-Ta  $\{111\}$  plane groupings are needed, shown in figure 2(b). Lattice relaxation of the final result, figure 2(c), gives the structure of Ta<sub>2</sub>C. A similar diffusion/shear mechanism would also give the correct stacking for the Ta<sub>4</sub>C<sub>3</sub> phase, as shown in figure 3. Carbon loss along every 4<sup>th</sup>  $\{111\}$  plane of the TaC structure, figure 3(a), will give the correct chemistry for Ta<sub>4</sub>C<sub>3</sub>. Subsequently, two opposing shears of the adjacent Ta-C-Ta-C-Ta-C-Ta  $\{111\}$  plane groupings will give the correct structure of the Ta<sub>4</sub>C<sub>3</sub> phase, as shown in figure 3(a). This yields the correct composition and stacking sequence for the Ta<sub>4</sub>C<sub>3</sub> phase, shown in figure 3(b). It should be noted that a lattice relaxation is needed to give the correct atomic spacing after the shearing.

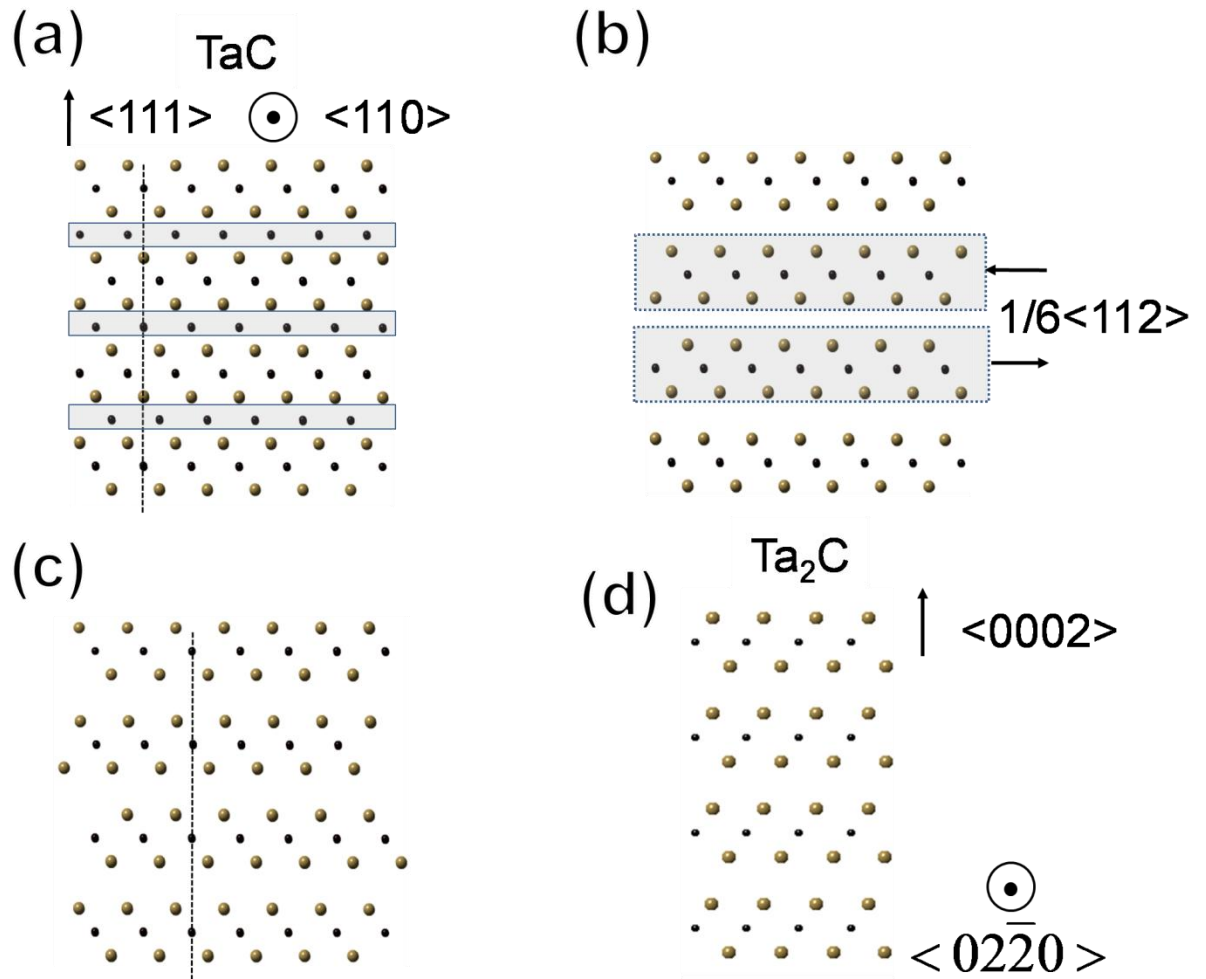


**Figure 2:** Transformation of the TaC structure to the Ta<sub>2</sub>C structure by a diffusion/shear mechanism. (a) TaC structure with planes of carbon highlighted to be removed allowing for the correct composition for Ta<sub>2</sub>C. (b) Shearing of adjacent Ta-C-Ta {111} plane groupings in opposing  $1/6\langle 112 \rangle$  directions. (c) Final structure similar to that of Ta<sub>2</sub>C. (d) Structure of the Ta<sub>2</sub>C phase.

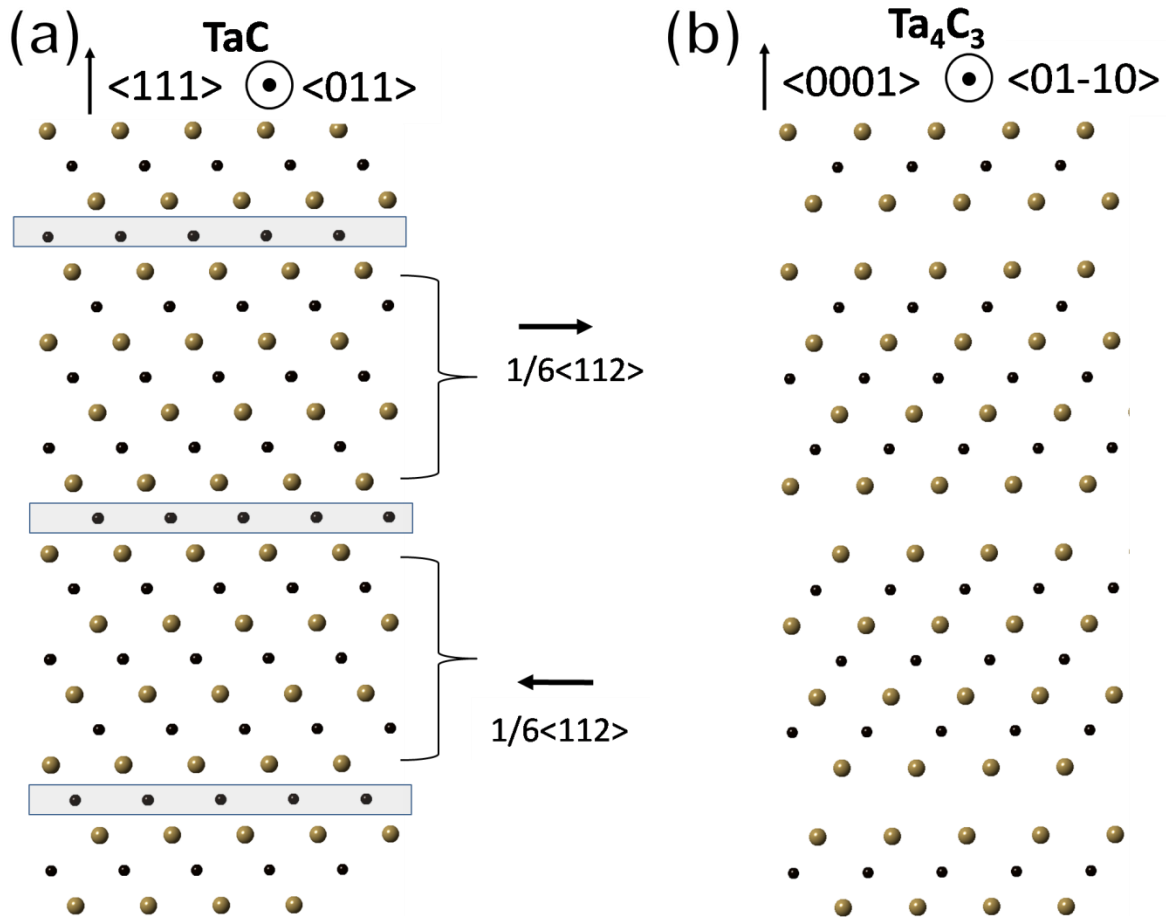


**Figure 3:** Transformation of the TaC structure to the Ta<sub>4</sub>C<sub>3</sub> structure by a diffusion/shear mechanism. (a) TaC structure with planes of carbon highlighted to be removed allowing for the correct composition for Ta<sub>4</sub>C<sub>3</sub> along with shearing of adjacent Ta-C-Ta-C-Ta-C-Ta {111} plane groupings in opposing  $1/6\langle 112 \rangle$  directions. (b) Structure of the Ta<sub>4</sub>C<sub>3</sub> phase.

#### 6.4 Thermo-mechanical Test Rig Improvements

Improvements to the thermo-mechanical testing rig are suggested for future work. To increase the force applied to the specimens, one would increase the sample thickness to allow for higher currents to pass through the sample while preventing melting of the sample because of the resistive heating. This would increase the maximum applied stress while maintaining similar temperatures. Obviously, this will require a more robust power supply capable of supplying the necessary current required to heat the sample and increase the Lorenz load. Alternatively, a

higher field strength electromagnet could be used but this could be limited by the size of the vacuum chamber.

Improvements to the test bar fixture are suggested such that the separate effects of thermal expansion which bows the bar because it is clamped could be removed through a piezoelectric stage which linearly extends to prevent bowing. Thus, after the sample is heated and allowed to linearly expand by the stage, the experiment then can proceed to bow or bend the bar under the Lorentz force of the magnetic field. With the development of this testing rig, the research program can now quantitatively explore the thermo-mechanical responses that accompany the different tantalum carbide microstructures as a function of load.

## REFERENCES

- [1] Gilbert Santoro, "Variation of Some Properties of Tantalum Carbide with Carbon content," *Transactions of the Metallurgical Society of AIME*, **227**(1963) 1361-1368
- [2] A. L. Bowman, "The Variation of Lattice Parameter with Carbon Content of Tantalum Carbide," *J. Phys. Chem. A*, **65**(9)(1961) 1596-1598
- [3] V I Smirnova and B F Ormont, "Limits of Homogeneity and the Relation of the Thermodynamic and Other Properties of the Carbide Phases of Ta to Their Composition and Structure," *Zh. Fiz. Khim.*, **30**(1956) 1327
- [4] V I Smirnova and B F Ormont, "Relation of the Heat and Free Energy of Formation of Tantalum Carbides to the Phase and Chemical Composition.," *Dokl. Akad. Nauk. SSSR*, **100**(1955) 127
- [5] R Lesser and G Brauer, "Carbide Phases in Tantalum carbide," *Z. Metallk.*, **49**(1958) 622
- [6] G V Samsonov and V B Rukins, "Microhardness and Electrical Resistance of Tantalum Carbides in Their Homogenous Region," *Dopovidi Akad. Nauk Ukr. RSR*, **3**(1957) 247
- [7] E K Storms, "The Tantalum-Tantalum Carbide System," in *The Refractory Carbides.*: Academic Press, 1967.
- [8] G. Santoro and H. B. Probst, "An Explanation of Microstructures in the Tantalum-Carbon System," in *Adv. X-Ray Anal.*, **7**, 1963, pp. 126-135.
- [9] K. Yvon and E. Parthe, "On the Crystal Chemistry of the Close Packed Transition Metal Carbides. I. The Crystal Structure of the z-V, Nb, and Ta Carbides," *Acta Crystallogra.*, **26**(1970) 149-153
- [10] D. J. Rowcliffe and G. E. Hollox, "Plastic Flow and Fracture of Tantalum Carbide and Hafnium Carbide at Low Temperatures," *J. Mater. Sci.*, **6**(1971) 1261-1269
- [11] O. M. Barabash and Y. N. Koval, *A Handbook on the Structure and Properties of Metals and Alloys*. Kiev: Naukova Dumka, 1986.
- [12] D A Porter and K E Easterling, *Phase Transformations in Metals and Alloys*, 2nd ed. New York: Chapman & Hall Press, 1993.
- [13] W. F. Brizes and J. M. Tobin, "Isolation of the Zeta Phase in the System Tantalum Carbide," *Journal of the American Ceramic Society*, **50**(2)(1967) 115-116
- [14] D. J. Rowcliffe, "Structure of Non-Stoichiometric TaC," *Mater. Sci. Eng.*, **18**(1975) 231-238

- [15] A. I. Gusev, A. S. Kurlov, and V. N. Lipatnikov, "Atomic and Vacancy ordering in carbide z-Ta<sub>4</sub>C<sub>3-x</sub> and Phase equilibria in the Ta-C system," *J. Solid State Chem.*, **180**(2007) 3234-3246
- [16] E. Rudy and D P Harmon, Air force Materials Laboratory Research and Technology Division, Air Force Command, Wright-patterson A.F.B., Ohio, AFML-TR-65-2, Part I, Volume V, 1965.
- [17] A. I. Gusev, A. A. Rempel, and V. N. Lipatnikov, "Incommensurate Ordered Phase in Non-Stoichiometric Tantalum Carbide," *Journal of Physics: Condensed Matter*, **8**(1996) 8277-8293
- [18] S-J. L Kang, *Sintering: Densification, grain growth and microstructure*. Boston: Elsevier Press, 2005.
- [19] S. DiPietro, J. Sekella, R. Roberts, M. Fuller, J. Shigley, L. Matson, M. Opeka, and J. Spain, "HIP processing and microstruture of TaC-based refractory compounds," in *31st annual conference on composites materials and structres*, Daytona Beach, FL, 2-25 January 2007.
- [20] K. Balani, G. Gonzalez, A. Agarwal, R. Hickman, and J. S. O'Dell, "Synthesis, Microstructural Characterization, and Mechanical Property Evaluation of Vacuum Plasma Sprayed Tantalum Carbide," *J. Am. Ceram. Soc.*, **89**(4)(2006) 1419-1425
- [21] Troy Kim and Margaret S. Wooldrich, "Catalytically Assisted Self-Propagating High-Temperature Synthesis of Tantalum Carbide Powders," *J. Am. Ceram. Soc.*, **84**(5)(2001) 976-982
- [22] P. Helisto, A.S. Helle, and J. Pietikainen, "Interface phenomena between oxide layers and cemented carbide tools," *Wear*, **139**(2)(1990) 225-234
- [23] Martina Di Ferdinando, Alessio Fossati, Alessandro Lavacchi, Ugo Bardi, Francesca Borgioli, Claudia Borri, Carlo Giolli, and Andrea Scrivani, "Isothermal oxidation resistance comparison between air plasma sprayed, vacuum plasma sprayed and high velocity oxygen fuel sprayed CoNiCrAlY bond coats," *Surface and Coatings Technology*, **204**(15)(2010) 2499-2503
- [24] "Introduction to Thermal Spray Processing," in *Handbook of Thermal Spray Technology*. USA: ASM International, 2004.
- [25] H. Bispinck, O. Ganschow, L. Wiedmann, and A. Benninghoven, "Combined SIMS, AES, and XPS investigations of tantalum oxide layers," *Applied Physics A: Materials Science & Processing*, **18**(2)(1979) 113-117
- [26] E.L. Courtright, J.T. Prater, G.R. Holcomb, G.R. St. Pierre, and R.A. Rapp, "Oxidation of hafnium carbide and hafnium carbide with additions of tantalum and praseodymium ," *Oxid. Met.* , **36**(5-6)(1991) 423-437

- [27] C. Kim, G. Gottstein, and D. S. Grummon, "Plastic Flow and Dislocation Structures in Tantalum Carbide: Deformation at Low and Intermediate Homologous Temperatures," *Acta Metall. Mater.*, **42**(7)(1994) 2291-2301
- [28] Melissa C. Teague, Gregory E. Hilmas, and William G. Fahrenholtz, "Mechanical properties of reactively processed W/Ta<sub>2</sub>C-based composites," *J. of the Euro. Ceram. Soc.*, **30**(11)(2010) 2197-2201
- [29] Liu Limeng, Ye Feng, and Zhou Yu, "Microstructure and Mechanical Properties of Spark Plasma Sintered TaC<sub>0.7</sub> Ceramics," *J. Am. Ceram. Soc.*, **In press**(2010)
- [30] R. E. Pawel and J. J. Campbell, "The influence of alloying elements on oxygen diffusion and flexure in tantalum base alloys," *Acta Metall.*, **29**(5)(1981) 809-817
- [31] Xiaohong Zhang, Gregory E. Hilmas, and William G. Farenholtz, "Densification, Mechanical Properties, and Oxidation Resistance of TaC–TaB<sub>2</sub> Ceramics," *J. Am. Ceram. Soc.*, **91**(12)(2008) 4129-4132
- [32] S. Gangireddy, J. W. Halloran, and W. N. Zachary, "Non-contact mechanical property measurements at ultrahigh temperatures," *J. Eur. Ceram. Soc.*, **30**(2010) 2183-2189
- [33] R. M. German, *Powder Metallurgy aand Particulate Processing*. Princeton, New Jersey: Metal Powder Industries Federation, 2005.
- [34] R. W. G. Wyckoff, *Crystal Structures I*, 2nd ed. New York: Interscience Publishers, 1963.
- [35] J. R. Cooper and R. L. Hansler, "Variation of electrical resistivity of cubic tantalum carbide with composition," *J. Chem. Phys.*, **39**(248)(1963)
- [36] V. G. Grebenkina and E. N. Denbnovetskaya, "Temperature coefficient of electrical resistivity of some complex carbides," *Powder Metall. Met. Ceram.*, **7**(3)(1968) 187-188
- [37] B. Eckstein and R. Forman, "Preparation and Some Properties of Tantalum Carbide," *J. App. Phy.*, **33**(1)(1962) 82-88
- [38] F. Lissner and T. Schleid, "Redetermination of the Crystal Structure of di-Tantalum mono-Carbide, Ta<sub>2</sub>C," *Z. Kristallogr. NCS*, **216**(6)(2001) 329
- [39] I. P. Zibrov, V. P. Filoneko, M. Sundberg, and P. E. Werner, "Structures and phase transitions of (b)Ta<sub>2</sub>O<sub>5</sub> and (z)Ta<sub>2</sub>O<sub>5</sub>: two high-pressure forms of Ta<sub>2</sub>O<sub>5</sub>," *Acta Crystallogr., Sect. B: Struct. Sci.*, **59**(2000) 659-665

## APPENDICES

APPENDIX A  
PROPERTY VALUES

The following is a collection of the parameters of the Ta-C and Ta-O phases used within this dissertation

TaC:

T<sub>m</sub>: 3985 °C [1]

Space group: 'F m 3 m' (225) [2]

Lattice parameter: (a) 4.4540 Å [2]

Unit cell volume: 88.359 Å<sup>3</sup> [2]

Electrical resistivity: ~ 2x10<sup>6</sup> Ωm [3,4]

Emissivity: 0.4 [5]

Ta<sub>2</sub>C:

T<sub>m</sub>: 3330 °C [1]

Space group: 'P -3 m 1' [6]

Lattice parameter: (a) 3.1059 Å (c) 4.9464 Å [6]

Unit cell volume: 41.323 Å<sup>3</sup> [6]

Ta<sub>4</sub>C<sub>3</sub>:

Space group: R-3m (166) [7]

Lattice parameter: (a) 3.1216 Å (c) 30.058 Å [7]

Cell Volume: 205.08 Å<sup>3</sup> [7]

TaO:

Space group: 'F m 3 m' (225)[2]

Lattice parameter: (a) 4.422 Å [2]

Unit cell volume: 86.468 Å<sup>3</sup> [2]

Ta<sub>2</sub>O<sub>5</sub>:

Structure: Monoclinic [8]

Space group: 'C 2/c' (15) [8]

Cell angle (alpha) 90.0 (beta) 104.264 (gamma) 90.0 [8]

Lattice parameter: (a) 12.7853 Å (b) 4.85370 Å (c) 5.5276 Å [8]

Cell volume: 332.45 Å<sup>3</sup> [8]

T<sub>m</sub>: 1872 °C [8]

#### References

- [1] O. M. Barabash and Y. N. Koval, *A Handbook on the Structure and Properties of Metals and Alloys*. Kiev: Naukova Dumka, 1986.
- [2] R. W. G. Wyckoff, *Crystal Structures I*, 2nd ed. New York: Interscience Publishers, 1963.
- [3] J. R. Cooper and R. L. Hansler, "Variation of electrical resistivity of cubic tantalum carbide with composition," *J. Chem. Phys.*, **39**(248)(1963)
- [4] V. G. Grebenkina and E. N. Denbnovetskaya, "Temperature coefficient of electrical resistivity of some complex carbides," *Powder Metall. Met. Ceram.*, **7**(3)(1968) 187-188
- [5] B. Eckstein and R. Forman, "Preparation and Some Properties of Tantalum Carbide," *J. App. Phy.*, **33**(1)(1962) 82-88
- [6] F. Lissner and T. Schleid, "Redetermination of the Crystal Structure of di-Tantalum mono-Carbide, Ta<sub>2</sub>C," *Z. Kristallogr. NCS*, **216**(6)(2001) 329
- [7] A. I. Gusev, A. A. Rempel, and V. N. Lipatnikov, "Incommensurate Ordered Phase in Non-Stoichiometric Tantalum Carbide," *Journal of Physics: Condensed Matter*, **8**(1996) 8277-8293
- [8] I. P. Zibrov, V. P. Filoneko, M. Sundberg, and P. E. Werner, "Structures and phase

transitions of (b)Ta<sub>2</sub>O<sub>5</sub> and (z)Ta<sub>2</sub>O<sub>5</sub>: two high-pressure forms of Ta<sub>2</sub>O<sub>5</sub>," *Acta Crystallogr., Sect. B: Struct. Sci.*, **59**(2000) 659-665

## APPENDIX B

### SIMULATED ZONE AXIS FOR COMMON TANTALUM CARBIDE PHASES

Simulations of electron diffraction patterns for the various tantalum carbide phases at different zone axis are shown below, organized by phase. The simulations were obtained using CrystalMaker® for windows by CrystalMaker Ltd.

TaC:

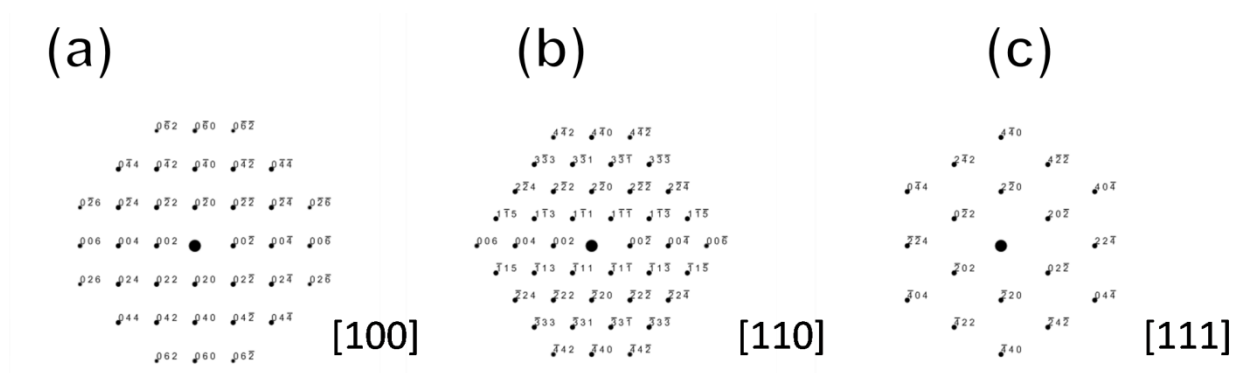


**Figure 1:** TEM electron diffraction simulation of the TaC structure for the viewing directions of (a) [100], (b) [110], and (c) [111].

Ta<sub>2</sub>C:



**Figure 2:** TEM electron diffraction simulation of the Ta<sub>2</sub>C structure for the viewing directions of (a) [1010], (b) [1230], and (c) [0001].

Ta<sub>4</sub>C<sub>3</sub>:

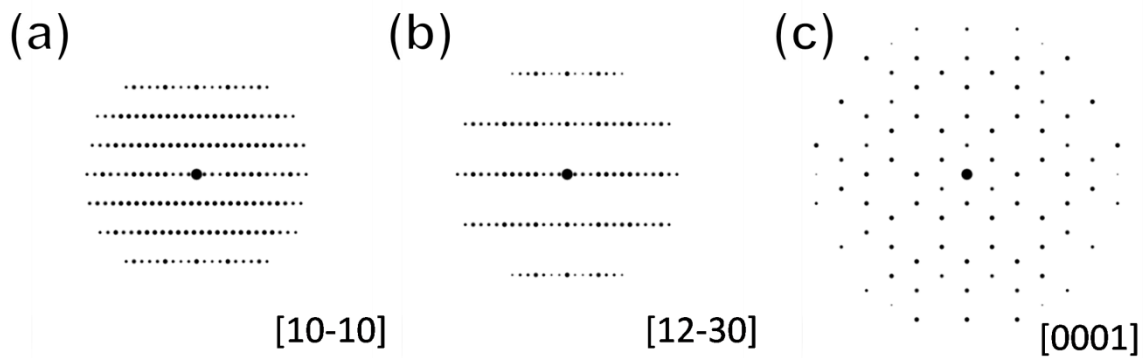


**Figure 3:** TEM electron diffraction simulation of the Ta<sub>4</sub>C<sub>3</sub> structure for the viewing directions of (a) [1010], (b) [1230], and (c) [0001].

## APPENDIX C

### SERIAL SECTIONING PROCEDURES

This procedure will create a 10X10X10um volume of serial sectioned data for use in later 3D analysis. The procedure of serial sectioning follows three main steps, sample preparation, sample alignment, and serial cutting/imaging, and will be divided as such.

The automated script routine consists of:

Image collection of the cutting surface - Image matching and alignment - milling of section - Rotation of sample - Image collection of imaging surface - image matching and alignment - Final image collection...Repeat (Figure1)

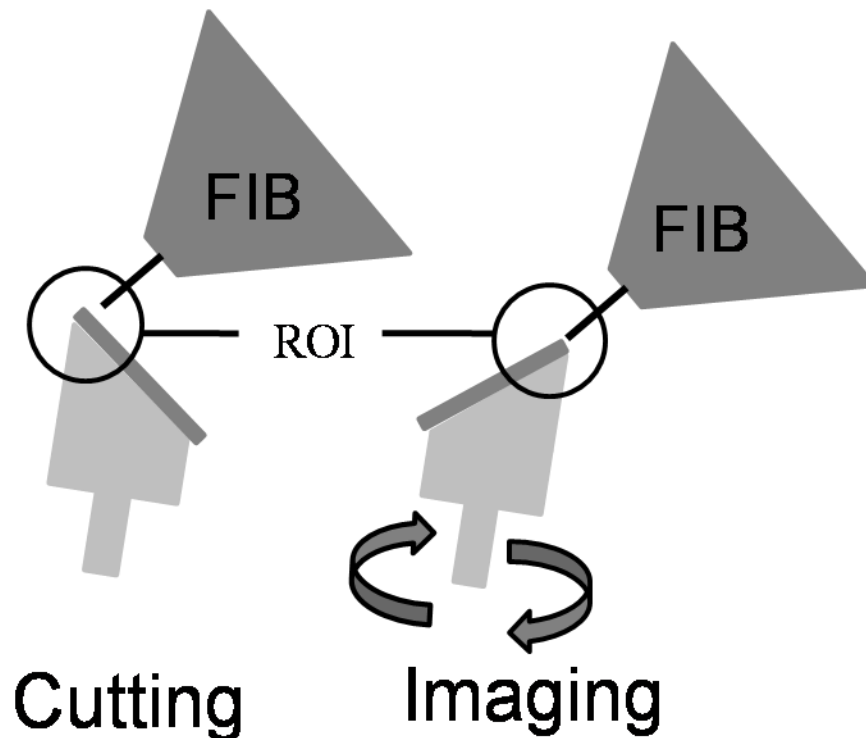


**Figure 1:** Sample positions in relation to the ion source during the different steps of the serial sectioning script

Sample preparation:

A sharp 90° polished edge is required.

-Section a thin foil from a bulk sample using a dicing saw/EDM/wire saw, or other cutting equipment.

(Optional) cut trenches on either side of ROI into sample using thin blade dicing saw.

-Glue sample to edge of metal mount using low temperature glue (i.e. Crystalbond ®)

-Polish both the top and side of sample to at least the equivalent of 3 um polish leading to a sharp edge. The smoother the surface, the easier the image matching will match the fiducial marks.

-Attach to a 45° SEM mount with the ROI . Carbon tape along with carbon paint will suffice for thin and small samples. Larger heavier samples will need to be mechanically fastened to holder.

Sample alignment:

-Load sample in to SEM/FIB Dual Beam microscope.

-Set WD to 15.2mm, find eucentric position of ROI, tilt sample to 7° so that FIB beam is parallel to the imaging surface of the ROI.

-Load runscript (Figure 2)

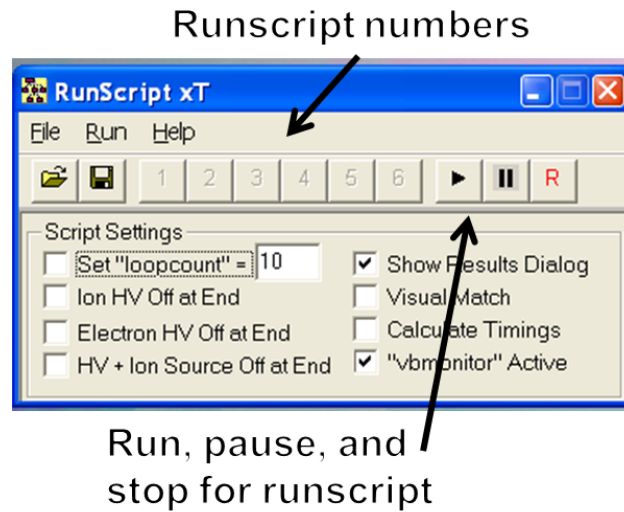


**Figure 2:** Runscript user interface

-Open the scripting workspace. File:Workspace:Open, find file: sliceandview.wsp

-Find ROI on sample, deposit a 1-3  $\mu\text{m}$  platinum cap on ROI using 1-0.3 nA

*Trench milling:*

-Using high current (3-5, nA or greater) mill a trench 10 $\mu\text{m}$  deep and at least 5 $\mu\text{m}$  wide on either side of the ROI. (Figure 3)

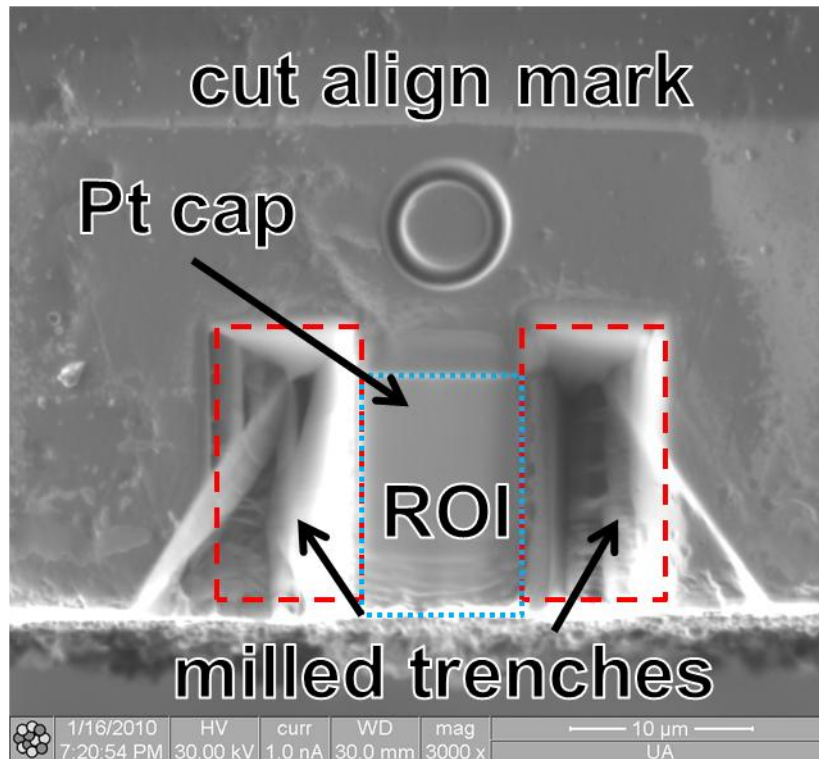


**Figure 3:** Milled sections of cutting image

-Polygon or rectangle cutting shapes are useful for this step. Make sure that there is no redeposition during cutting

*Cut positioning:*

-Cut 10um diameter circle above ROI using 0.5 or 0.3nA.

- Image the cut circle at appropriate magnification (approx 2-3000X) and save the image as CutImageXXXX.bmp, where XXXX is the magnification.

-Open windows paint program and find CutImageXXXX.bmp. Using selection tool, selected the area around the cut circle.

-Edit: Cut then File:new, then Edit: Paste. You should have an image of only the cut circle. Save this file as Cutalign.bmp (Figure 4)

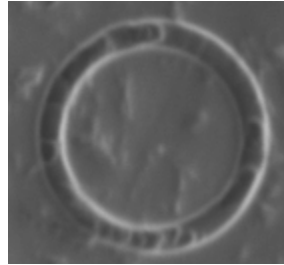


**Figure 4:** Cropped Cutalign.bmp image for image matching routine.

-Back on the FIB UI, make sure magnification is the same as what you used to take the picture.

-Select the appropriate cutting current to be used for the cutting (approx 1-5 nA, depending on metallurgical engineer mill rate, step size, and cutting width).

-Make sure focus, stigmation and all other parameters are optimized, as these setting will all be saved and reused for each cut.

-Using the runscrip, run #1 (GetCutPositions.txt).

- Image window will open and find the circle using the image matching routine using the Cutalign.bmp file to match the image it just captured.

-Your settings and positions for the cutting step should be complete.

-If an error occurs, make sure the picture you took and saved is the same as the image the image match window.

*Image positioning:*

-Rotate the sample 90 degrees so that you can see the face of the ROI (Figure 5).

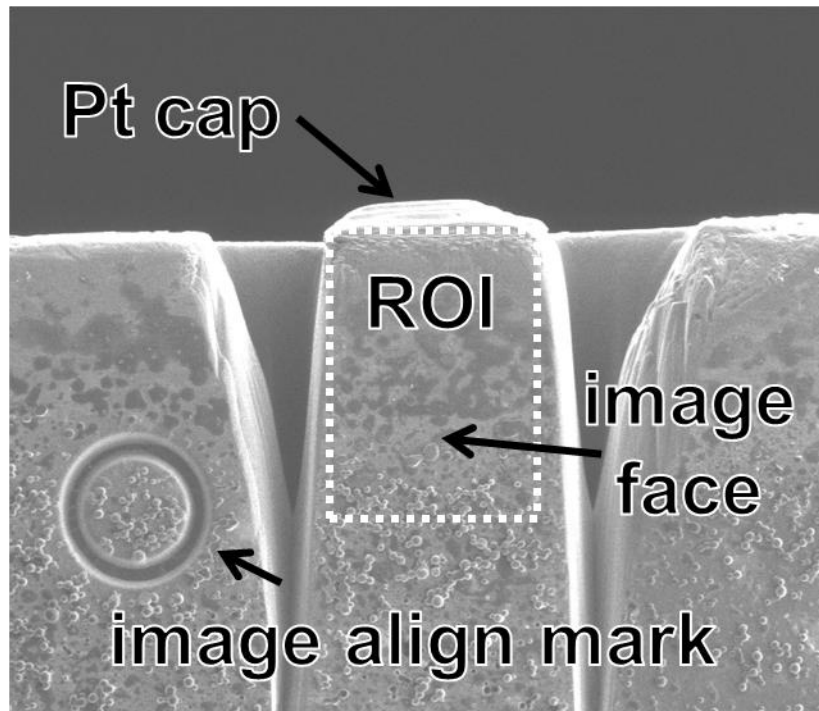


**Figure 5:** Imaging area of ROI showing the milled trenches and image alignment mark.

-Cut 10um diameter circle to the side of the ROI using 0.5 or 0.3nA.

-Image the cut circle at appropriate magnification (approx 2-3000X) and save the image as ImagingImageXXXX.bmp, where XXXX is the magnification.

-Open windows paint program and find ImagingImageXXXX.bmp. Using selection tool, select the area around the cut circle.

-Edit: Cut then File:New, then Edit: Paste. You should have an image of only the cut circle. Save this file as Imagealign.bmp

-Back on the FIB UI, make sure magnification is the same as what you used to take the picture.

-Select the appropriate imaging current to be used for the image collection (approx 0.3-0.1 nA, depending on mill rate, step size, and cutting width).

-Make sure focus, stigmation and all other parameters are optimized, as these setting will all be saved and reused for each cut.

-Using the runscript, run #2 GetImagePositions.txt.

- Image window will open and find the circle using the image matching routine using the Imagealign.bmp file to match the image it just captured.

Your settings and positions for the cutting step should be complete.

If an error occurs, make sure the picture you took and saved is the same as the image the image match window.

#### *Runscript file editing:*

You will need to edit three text files that control the runscript using a text editor, such as windows notepad, autolog.99, AutoSV.psc, and Setup.ini.

-Starting with autolog.99, which serves as the counter for the steps run, open the file in a text editor and replace the number and any text that follows with 0. (Figure 6) The file should read:

counter=0

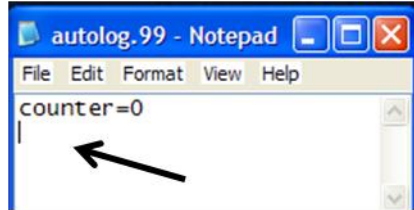


**Figure 6:** Initial autolog.99 file. Counter should be set at zero with a carriage return following.

-Open the AutoSV.psc file in the editor; look for the line "#goto end" approximately half way down the page. Remove only the # sign, so the line reads "goto end". (Figure 7)

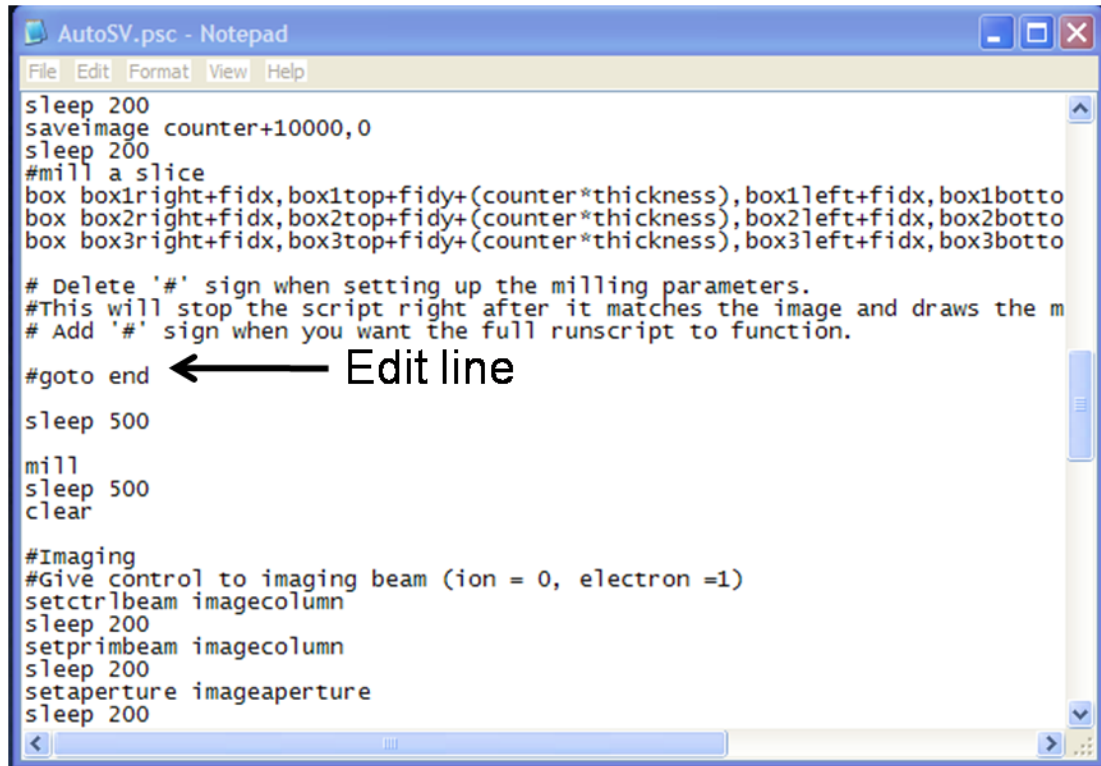


**Figure 7:** Location of the "#" sign to be replaced and added in the AutoSV.psc file.

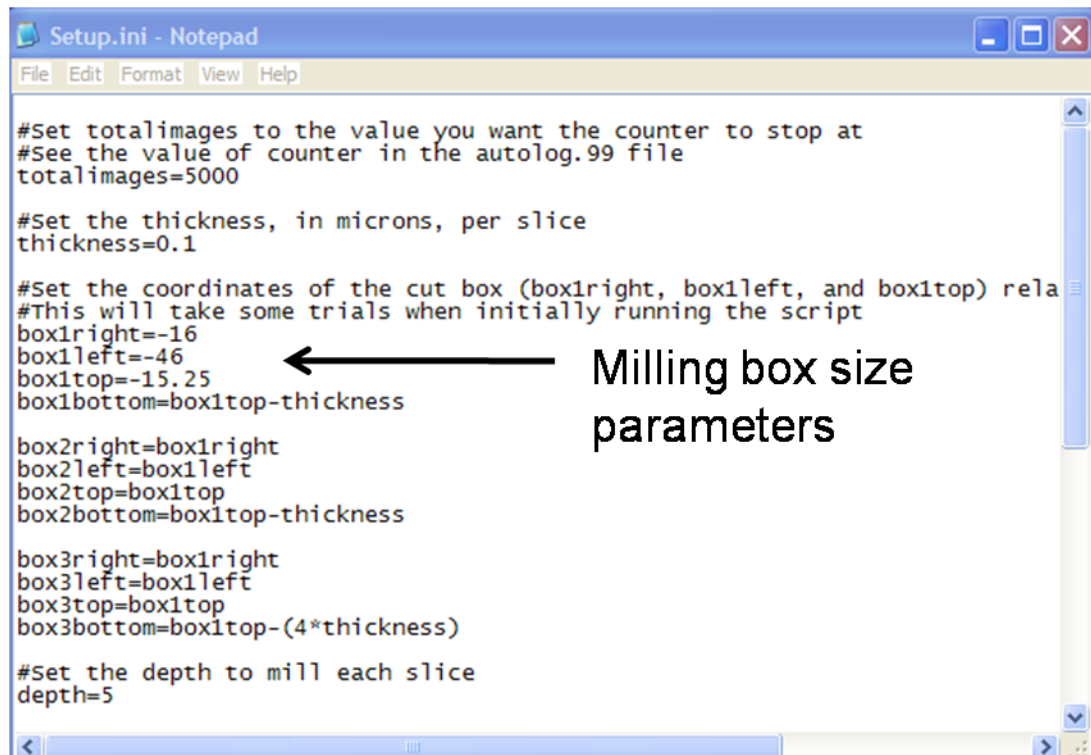
This will cause the script to match the image, draw the milling boxes and then go to the end of the script.

-Save the file and in the runscript, select and run script #3, AutoSV.psc

The program will change to the parameters that it uses to cut, take a single image, perform the image match, draw the milling boxes, and end the script.

The next steps involve a repetition of changing the parameters in the setup.ini file that control the position of the milling boxes and running the script until the milling boxes are upon the edge of the ROI.

-Open the setup.ini file using a text editor. (Figure 8)



```
Setup.ini - Notepad
File Edit Format View Help

#Set totalimages to the value you want the counter to stop at
#See the value of counter in the autolog.99 file
totalimages=5000

#Set the thickness, in microns, per slice
thickness=0.1

#Set the coordinates of the cut box (box1right, box1left, and box1top) rela
#This will take some trials when initially running the script
box1right=-16
box1left=-46
box1top=-15.25
box1bottom=box1top-thickness

box2right=box1right
box2left=box1left
box2top=box1top
box2bottom=box1top-thickness

box3right=box1right
box3left=box1left
box3top=box1top
box3bottom=box1top-(4*thickness)

#Set the depth to mill each slice
depth=5
```

**Figure 8:** Location of the parameter to be edited in the setup.ini file.

Change/adjust/leave the following settings:

Cut thickness- controls the thickness of each cut

box1right-controls the rightmost corner of the milling box, in um, where 0 is the center of the screen.

box1left- controls the leftmost corner of the milling box, in um, where 0 is the center of the screen.

box1top- controls the uppermost corner of the milling box, in um, where 0 is the center of the screen.

Depth- control the milling time which determines the depth of cut.

Since it is cutting an edge, which mills faster, this number can be 1-0.5 times the actual depth.

*i.e.* an actual 10um deep cut only requires a depth of 5

-Save the setupini.txt file and rerun the #3 runscript.

-After it make the adjustments in the box positioning, re-edit the setup.ini file until the milling box is in the desired location (Figure 9). Make sure the milling boxes extend past the ROI to ensure a complete cut.

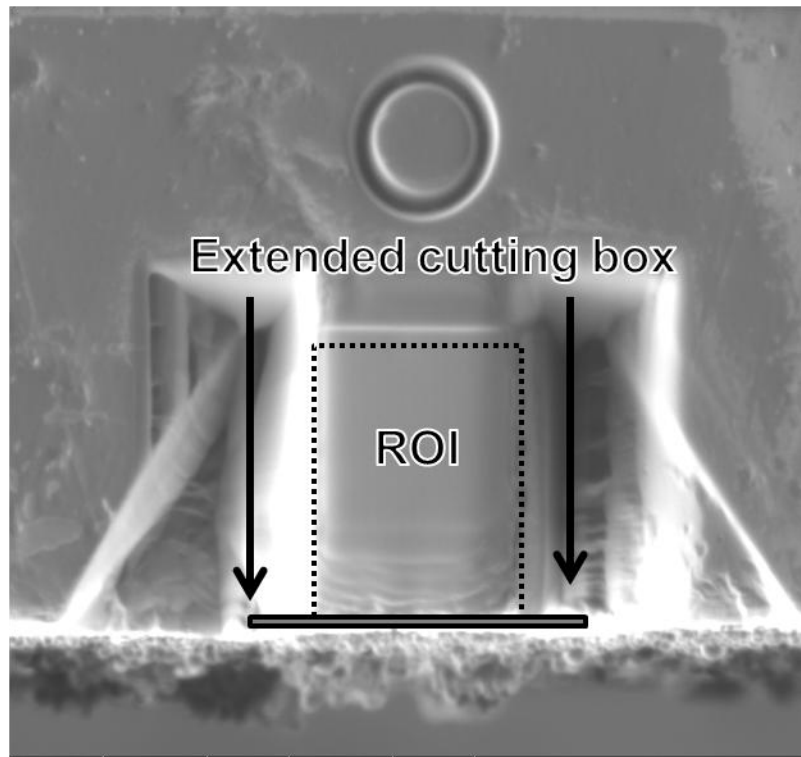


**Figure 9:** Location of milling box showing the extended size.

-Re-open the AutoSV.psc files and go back to the line previously added, replacing the “#” sign, so that the line reads "#goto end"

The runscript should be ready to run!

Adjustments will need to be made to the actual collected image for proper magnification, dwell time, contrast and brightness. This again can be adjusted by altering the setup.ini file

image2magnification=15000 (actual image magnification)

image2dwell=10000 (dwell time of the beam, in ms)

image2contrast=30240/1000 (arbitrary value used by the FIB, can be determined by running the #4 runscript, and read in the output text file autolog.77)

image2brightness=300/1000 (arbitrary value used by the FIB, can be determined by running the #4 runscript, and read in the output text file autolog.77)

Once the correct imaging values for the collected serial slice image is obtained. The #3 runscript can be run for automated serial sectioning.

*Serial sectioning:*

-Press the play button on the runscript user interface. Monitor the progress. Images will be saved in the same folder of the runscript files. Different filenames will correspond to the different types of files:

1K series- image matching for cutting face

2K Series- Image matching for the imaging face

3K and 4K series- Low and high magnification of ROI

After runscript has completed, images can then be compiled into 3D reconstruction software.

*List of files and their function required for automated scripting:*

SliceandView.wsp - sets up the runscript user interface

AutoSV.psc – controls the microscope and call the different functions for cutting/imaging

Setup.ini – hold the cutting parameters to be called by AutoSV.psc

Autolog.99 – Counter file

Autolog.88 – Holds the image parameters, positions and settings

Autolog.80 – Holds the cutting parameters, positions and settings

Autolog.77 – hold the values of contrast and brightness, as called by Getcb.txt

Get Cut Positions.txt – retrieves the cutting parameters, positions and settings

Get image positions.txt – retrieves the imaging parameters, positions and settings

Getcb.txt – retrieves the contrast and brightness values and displays them in the autolog.77 file